Measurement of Bottom Production in $p\bar{p}$ Collisions at $\sqrt{s}$=1.8 TeV Using Muon Impact Parameters

by

Tae Yung Song

A dissertation submitted in partial fulfillment
of the requirements for the degree of
Doctor of Philosophy
(Physics)
in The University of Michigan
1995

Doctoral Committee:

Associate Professor Dan Amidei, Chair
Professor Rolf A. Deininger
Professor Rudolf P. Thun
Professor John F. Ward
Professor York-Peng Ed Yao

Acknowledgments

First of all, I would like to thank all CDF members for making this thesis possible. Many people in CDF, too numerous to be mentioned individually, helped me complete this thesis, directly or indirectly.

I also thank the members of Michigan CDF group for supporting me in many ways during my years at University of Michigan as a CDF member.

I thank my advisor, Dan Amidei, for his guidance and patience during my career as a graduate student working on this experiment.

I owe special appreciation to Paul Derwent who provided me a lot of skills and knowledges needed to achieve my goal.

I would like to express my gratitude to many Korean friends at FNAL and Ann Arbor. Their warm friendship made my life more enjoyable.

Finally, I would like to thank my family for their affection and emotional support over all these years.

Table of Contents

List of Figures

Figure

List of Tables

Table

Chapter 1

Introduction

In this analysis we measure the cross sections for production of bottom quarks in $p\overline{p}$ collisions at $\sqrt{s}$=1.8 TeV. We measure inclusive integral rates above minimum bottom transverse momentum (Pt) = 15, 25 and 35 GeV/c, using the muon decay channel of bottom quarks. We measure the fraction of bottom muons in the inclusive muon samples using impact parameter information given by precision tracking and calculate bottom cross sections by combining the bottom muon fraction with other experimental efficiencies and acceptance.

1.1 Standard Model

According to the Standard Model of elementary particle physics [1], 6 quarks and 6 leptons are fundamental building blocks of matter and 4 fundamental forces act on them. The interactions between particles are determined by the invariance of the theory under gauge transformations [2]. The quarks and leptons are listed in Table 1.1 and Table 1.2 gives the list of fundamental forces and their respective carriers. The existence of 5 quarks has been well established and evidence for the sixth (top) quark

was reported by the CDF in 1994 [3]. For the leptons, only ν_τ has not been observed directly yet. The gluons were predicted to exist and were observed at PETRA in 1979 with the expected properties. W and Z bosons were discovered at CERN in 1983 and their masses agree with theoretical prediction [4].

Charge		1st generation	2nd generation	3rd generation
		Quarks		
$+2/3$		up (u)	charm (c)	top (t)
$-1/3$		down (d)	strange (s)	bottom (b)
		Leptons		
-1		electron (e)	muon (μ)	tau (τ)
0		electron neutrino (ν_e)	muon neutrino (ν_μ)	tau neutrino (ν_τ)

Table 1.1: Table of quarks and leptons.

Force carrier	Spin	Force	acts on
graviton	2	gravity	massive particles
photon (γ)	1	electromagnetic	electrically charged particles
$W^{\pm}$,Z	1	weak	quarks, leptons
gluon (g)	1	strong	quarks

Table 1.2: Table of fundamental forces and their carriers.

1.2 The Theory and Test of QCD

QCD (Quantum Chromodynamics) is the part of the Standard Model that describes strong interactions between quarks and gluons, according to a local non-abelian gauge theory with gauge group $SU(3)$. One of the fundamental properties of QCD is the shrinking of the coupling constant as the energy of interaction grows (asymptotic freedom) . In spite of this, the QCD calculation in high energy hadronic collisions cannot be done completely by perturbative methods since the fundamental particles are deeply bound inside the hadrons we use as beams. The solution is given by a factorization theorem [5], whereby cross sections can be expressed as the product of factors, each one involving phenomena appearing at different energy scales. At sufficiently high energy, that is when the energy scale exceeds a few $\mathrm{GeV/c^2}$, collisions between hadrons can be modeled as collisions of individual quarks and gluons, which are collectively called partons.

QCD has been tested in hadron-hadron collisions with the development of the theory. The earliest measurement of high Pt hadron production at the Intersecting Storage Rings (ISR) confirmed the parton model. Although the observation of jets and early tests of QCD at the S$p\bar{p}$S [6] were largely qualitative, they proved that experimental results can be predicted by the theory at leading order in perturbation theory. Currently we are entering a period where the emphasis is shifting to precision measurement.

1.3 Other Interests in b Quark Production

It is one of the tests of QCD to measure production cross sections of heavy quarks such as b quark from hadron-hadron collisions. In addition, there is great interest

in the b quark system as a laboratory for the measurement of quark mixing angles and CP violation. Besides testing QCD, the measurement of b quark production properties is important information for the design of future experiments on b quark physics at hadron colliders.

1.4 QCD Prediction of b Quark Cross Section

Based on the QCD parton model described in the above section, the inclusive cross section of the production of heavy quarks from the hadron-hadron collision is expressed in the following way [7]. Protons and antiprotons are indicated by a and b and partons in the protons and antiprotons are represented by i and j.

$$\sigma = \sum_{i,j} \int dx_1 dx_2 \hat{\sigma}_{i,j}(x_1 P_a, x_2 P_b, m, \mu) f_i^a(x_1, \mu) f_j^b(x_2, \mu) \tag{1.1}$$

- σ = heavy quark cross section
- x_1, x_2 = momentum fraction of parton in the incoming hadrons
- $\hat{\sigma}$ = subprocess cross section of parton-parton collision
- P_a, P_b = incoming proton and antiproton momentum
- m = mass of heavy quark
- μ = energy scale for strong coupling constant
- f_i^a, f_j^b = parton structure function

The subprocess cross section can be calculated based on QCD perturbation theory and the b quark production cross section has been calculated up to next-to-leading

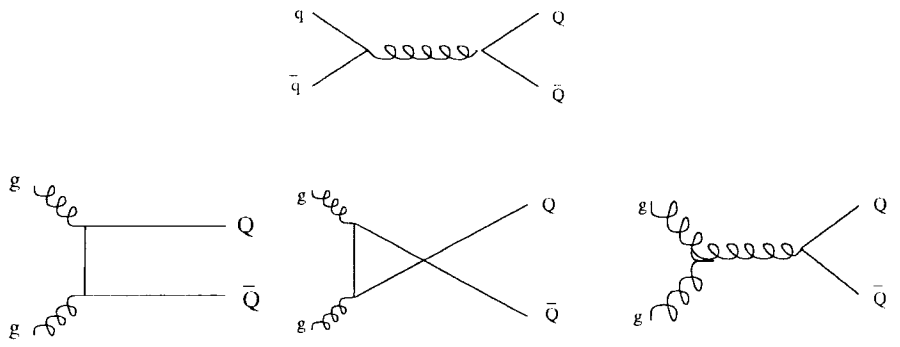

Figure 1.1: Feynman diagrams for the lowest order terms of heavy quark production.

order term. The lowest order term is $\alpha_s^2(\mu)$ and Figure 1.1 are the tree-level Feynman diagrams describing that interaction. Figure 1.2 shows tree-level Feynman diagrams of next-to-leading order terms. We note in passing that graphs with virtual corrections must also be included in order to get convergent results.

The cross section increases by a factor of two by including next-to-leading order terms. Figure 1.3 [8] shows how the cross section changes as function of energy scale when the next-to-leading order term (L+LN) is included.

Many factors are involved in the equation (1.1), and the quantitative prediction of QCD for the production cross section has an uncertainty due to the following reasons.

- Structure function :

  The proton structure function is not well known in the region of interest, mostly low x. Most measurements have been done by deep inelastic scattering of leptons from protons, which give information of the structure function at large x and

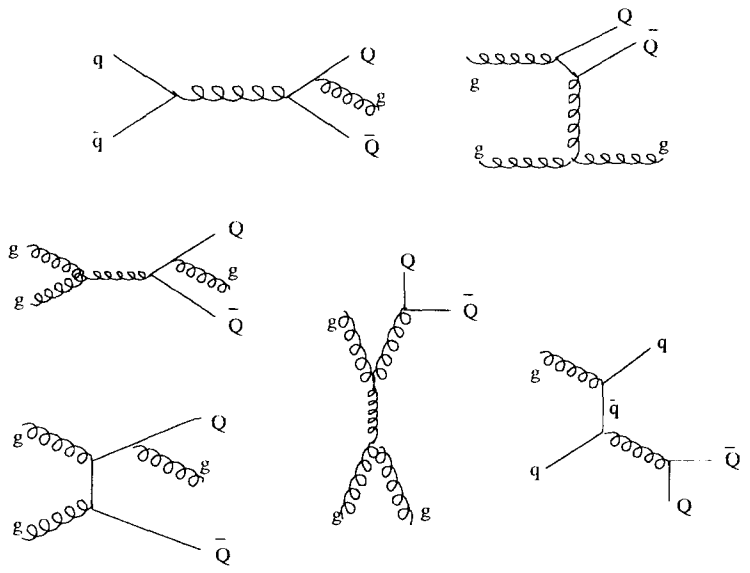

Figure 1.2: Feynman diagrams for next-to-leading order terms of heavy quark production.

small μ, which is not the case here.

- Mass of the quark :

  The mass of the bottom quark is estimated from the mass of the B mesons, which is about 5 GeV/c^2. The cross section changes by a factor of two when the b quark mass is shifted by 10%.

- Energy scale :

  The result of any QCD calculation depends on an input energy scale characteristic of the process involved, and is somewhat arbitrary. Figure 1.3 shows the energy scale dependence of the bottom quark cross section at the $p\bar{p}$ collider at the center of mass energy 1.8 TeV.

1.5 Prior Measurements of b Quark Cross Section

Previous to this work, the b quark production cross section in $p\bar{p}$ collisions has been measured at UA1 ($\sqrt{s}$ = 630 GeV), and D0 and CDF ($\sqrt{s}$ = 1.8 TeV) using many different b quark decay channels. Figure 1.4 [9] shows the QCD prediction of the bottom cross section from $p\bar{p}$ collisions at $\sqrt{s}$ = 630 GeV and UA1 measurements. Figure 1.5 and 1.6 [10] shows predictions at $\sqrt{s}$ = 1.8 TeV along with previous D0 and CDF measurements.

Prior measurements at UA1 and CDF use the exclusive decay of B mesons to J/ψ and the semileptonic decays to electrons and muons. The semileptonic decay channels have 20 times the statistics of the exclusive decays, but a disadvantage of fairly large backgrounds. The essential part of the measurement is therefore to know the fraction of the inclusive leptons coming from the b quark, and to know it with minimal uncertainty. Some UA1 and D0 measurements used a Pt_rel fitting method [11] to measure the bottom fraction. Pt_rel is the transverse momentum (Pt) of a track relative to the direction of the jet containing the track. Due to the large mass of the b quark, the Pt_rel of leptons coming from b quarks is relatively large compared to that of background leptons The bottom fraction is measured by fitting the Pt_rel distribution of inclusive leptons to a sum of contributions, including a high tail from b decays.

1.6 Measurement by Impact Parameter Fitting Method

Our analysis uses an inclusive muon sample to measure the bottom cross section using the muon decay channel of b quark. As explained in the above section, we need

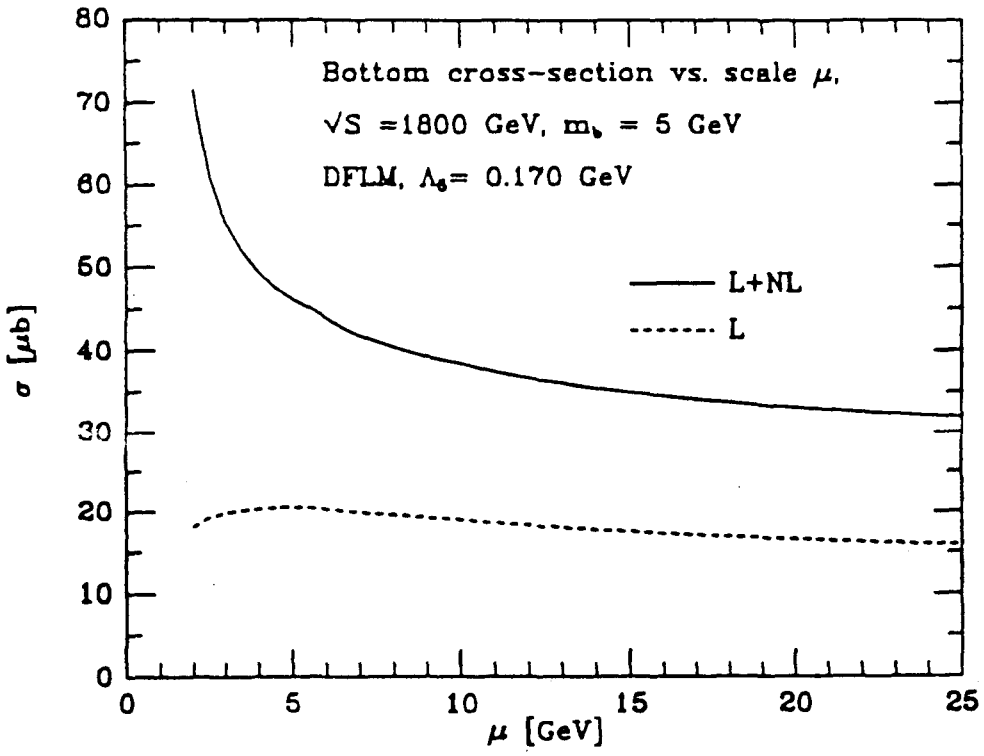

Figure 1.3: Scale dependence of b quark production cross section.

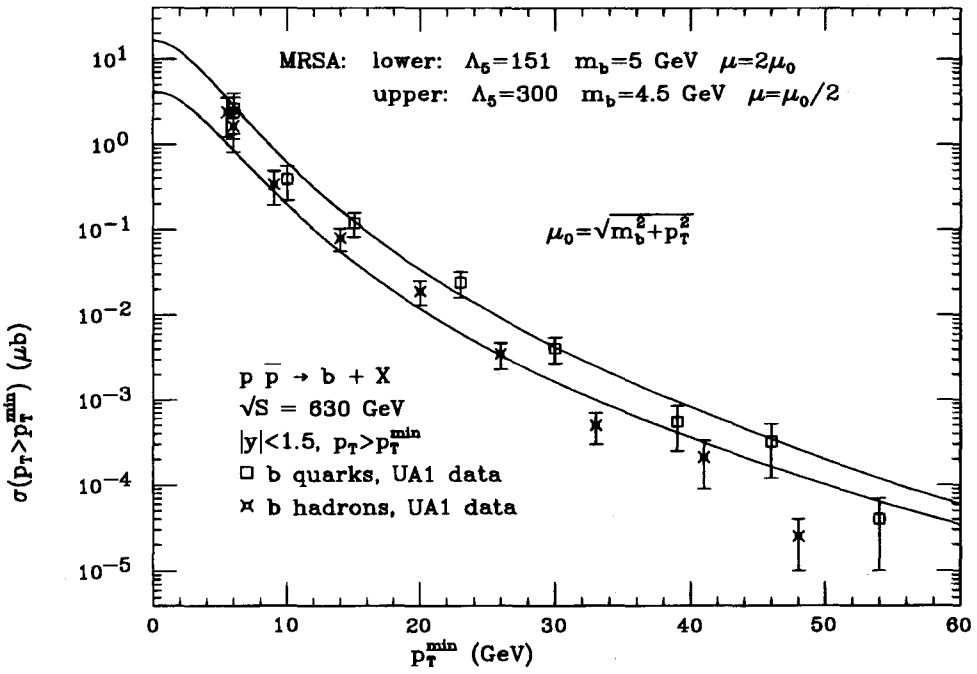

Figure 1.4: UA1 measurements of b quark production cross section.

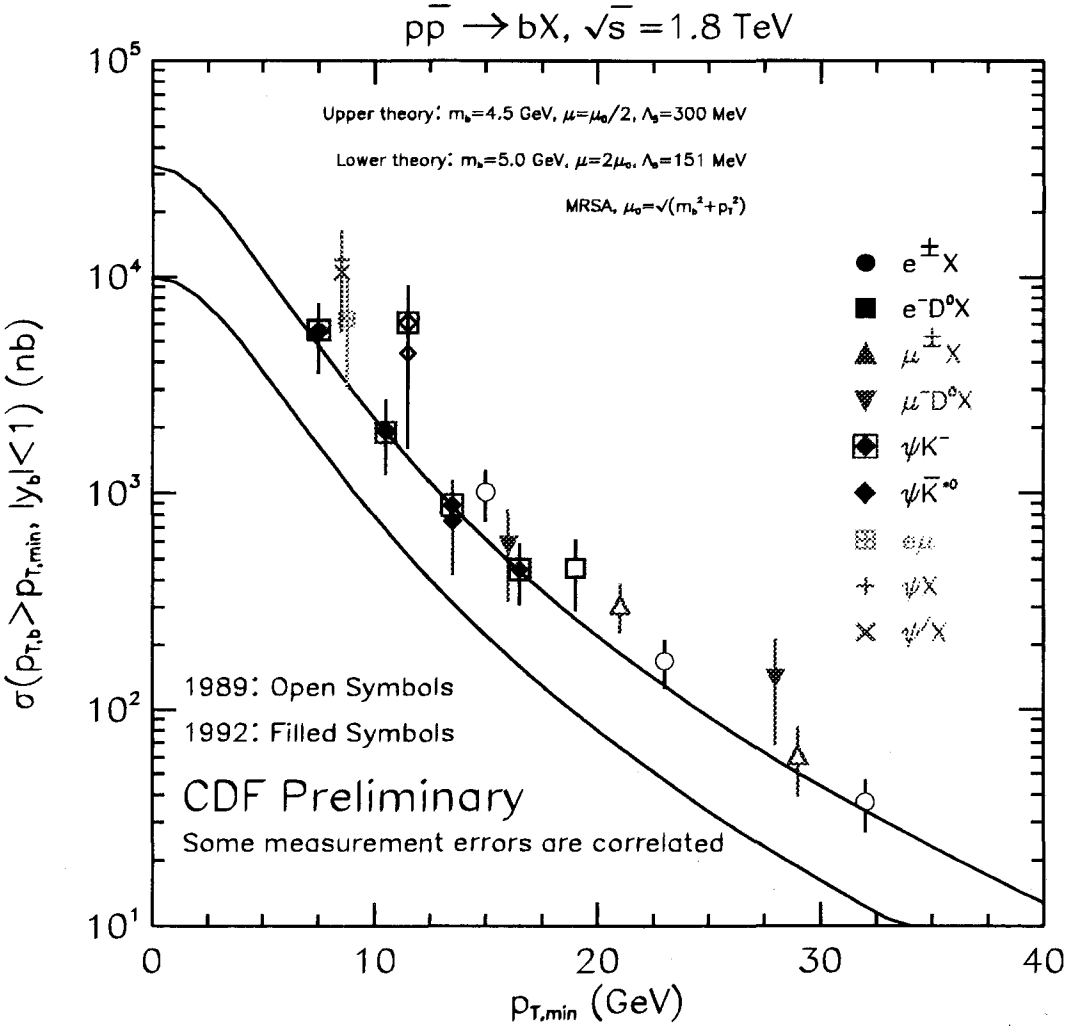

Figure 1.5: CDF measurements of b quark production cross section.

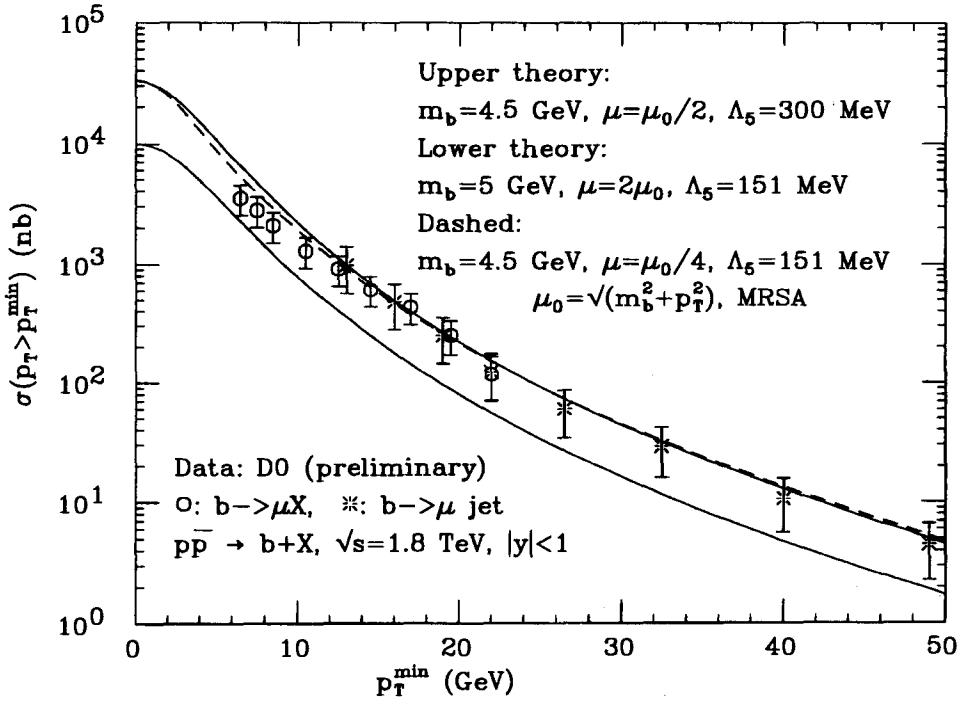

Figure 1.6: D0 measurements of b quark production cross section.

to measure the bottom muon fraction in the inclusive muon sample and we use an impact parameter fitting method for that purpose.

We define impact parameter as the distance of closest approach of the trajectory of a b decay product to the primary vertex, projected on the plane perpendicular to the beam line. Figure 1.7 is the topology of B production and its decay and Figure 1.8 shows the definition of impact parameter.

Long-lived hadrons decay with some average lifetime and their decay products emerge with a kink angle with respect to the original hadron direction. The B decay length distance is $\gamma\beta c\tau$, where τ is the proper decay time, γ and β describe the relativistic momentum of the B hadron and c is the speed of light. The impact parameter is given as

$$\text{decay length} \times \sin\delta = \gamma\beta c\tau \sin\delta \tag{1.2}$$

where δ is kink angle. We see that the mean impact parameter is proportional to the proper decay time, and the kink angle, which depends on the mass and momentum of the decaying particle. The lifetime and mass of the decaying particle are invariant characteristics of the specific decay, and this will allow us to measure the bottom fraction with the impact parameter distribution of its decay products. This method will be discussed in detail in Chapter 6.

Once we know the bottom muon fraction, we need to connect the bottom muon rate to the b quark production rate. Since the detected bottom muon rate is necessarily only a fraction of the total due to kinematical selections, geometrical coverage of the detector, offline quality control and so on, we need to know the magnitudes of

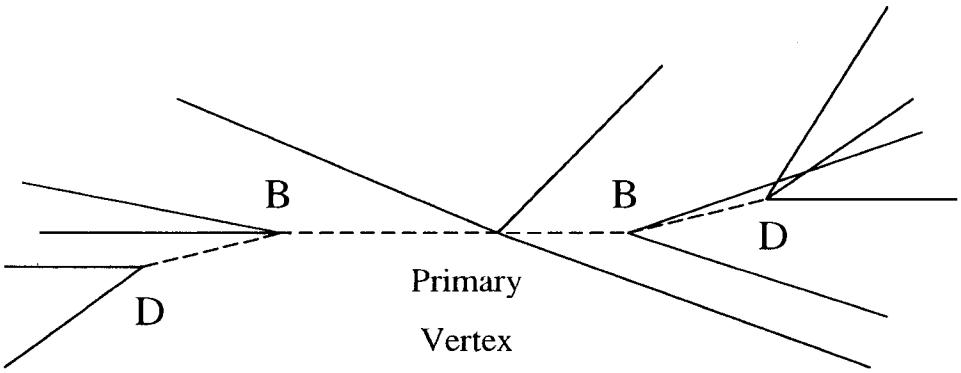

Figure 1.7: Topology of B production and its decay.

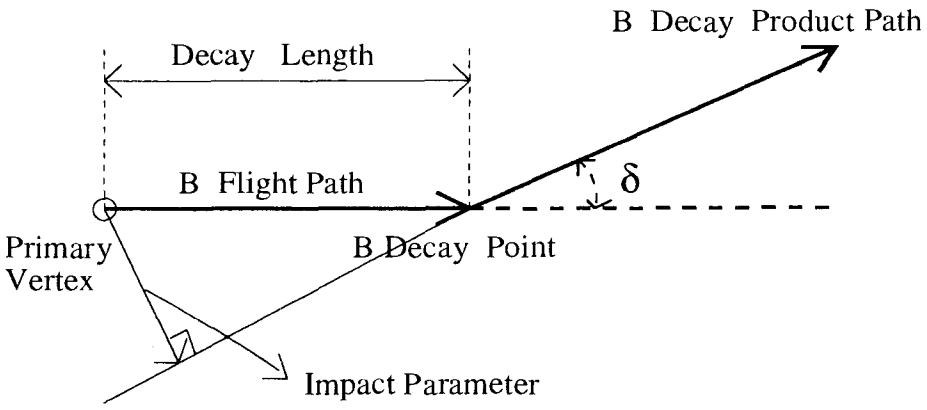

Figure 1.8: Definition of impact parameter.

the efficiency factors. This will be discussed in Chapter 4 and 5.

The details of the CDF experiment are described in Chapter 2 and the details of the data set is given in Chapter 3. Finally, results and conclusion will be presented in Chapter 7.

Chapter 2

The CDF Experiment

The Tevatron is a proton-antiproton collider operating at Fermilab National Accelerator Laboratory (FNAL) outside of Chicago, Illinois, U.S.A.. The Collider Detector at Fermilab (CDF) is one of two detectors designed to study physics from $p\bar{p}$ collisions. In this chapter we will discuss the general features of the experimental arrangement and some specific details pertinent to this analysis.

2.1 The Tevatron

Figure 2.1 shows the layout of the FNAL accelerator system. Protons are accelerated to 8 GeV in several stages [12] and then injected into the "Main Ring". The Main Ring boosts protons to 150 GeV, and they are then injected into the Tevatron, which is a superconducting synchrotron.

Antiprotons are made by colliding protons into tungsten-rhenium, and collecting antiprotons into the "accumulator" where they are stored and cooled. When adequate antiprotons are available, they are injected into the Main Ring and the Tevatron step

by step in the same way protons are injected, but rotating in the other direction.

The counter-rotating protons and antiprotons in the Tevatron are accelerated to 900 GeV and, at two points on the circumference, focused into each other to produce $p\bar{p}$ collisions with a center-of-mass-energy ($=\sqrt{s}$) of 1.8 TeV.

2.2 The CDF Detector

The CDF detector recorded its first data in 1988 and 1989, and has been subsequently upgraded. Figure 2.2 and 2.3 show an isometric view and one quadrant of a cutaway view of the detector with subsystem detectors labeled. The CDF coordinate system is defined in the top left corner of Figure 2.3 and consists of right handed spherical coordinates with the polar axis along the proton beam line. The recent CDF upgrade was finished in 1992 and took data in 1992 and 1993.

The CDF has tracking detectors to reconstruct trajectories (tracks) of charged particles. These tracking detectors are contained in a 1.4 Tesla superconducting central solenoid magnet and the track curvature measures particle momentum. Matching these tracks to signals in certain other detectors allows us to identify and measure muons. We will discuss tracking detectors and muon system in detail in the Sections 2.3 and 2.4.

The CDF also has hadronic and electromagnetic calorimeters to measure energy flow of the collision debris. These calorimeters are arranged in projective towers outside of solenoid and tracking volume, covering all of azimuth and pseudorapidity (η) from -4.2 to 4.2, where η is defined as

$$\eta = -\ln(\tan\frac{\theta}{2})$$

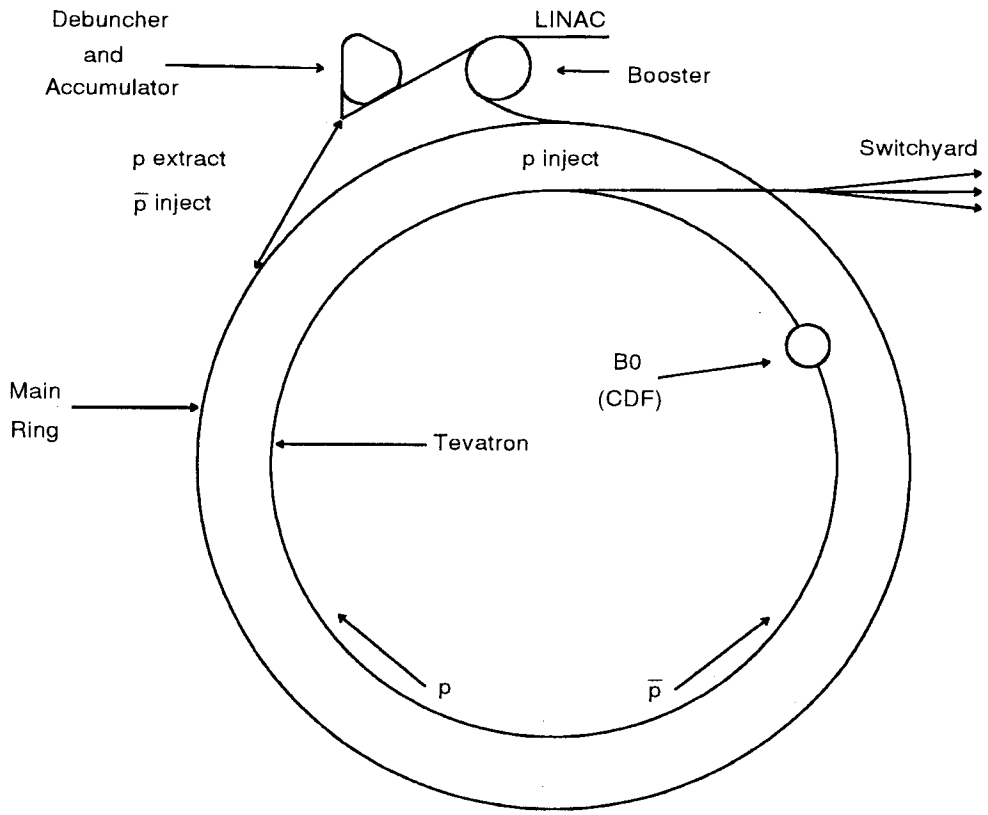

Figure 2.1: The layout of the Tevatron.

The following sections describe the portions of the CDF detector that are especially relevant to this analysis.

2.3 The Central Tracking System

The CDF central tracking system consists of 3 main sub-detectors, which are the Central Tracking Chamber (CTC), the Vertex Chamber (VTX) and the Silicon Vertex Detector (SVX). They are all inside the solenoid.

Closest to the interaction point is the SVX, a silicon microstrip detector surrounding the beam pipe and covering r=3 cm to 8 cm. The SVX is a 2-dimensional detector which makes a precision tracking measurement in the r-ϕ plane. The SVX is the main detector component of this analysis, and will be discussed separately in Section 2.5.

The VTX covers the radial region starting outside the SVX , from r=8 cm to 50 cm, surrounding the SVX. The main function of the VTX is to determine the event z vertex which, in the Tevatron, is distributed some distance along the beam line. It measures each track and a combined vertex fit is used to find event z with a resolution of about 1 mm. The VTX consists of 28 modules extending 2.6 m along z, covering $|\eta| < 3.5$.

Figure 2.4 is the event z vertex distribution of the typical events and it is well described by a Gaussian with mean of -1.2 cm and sigma of 25.1 cm. The event z distribution changes slightly run by run according to changing beam conditions. Table 5.1 in Chapter 5 shows the change of z distribution as these 1992 and 1993 data run progressed.

Outside of the VTX, in the region 55 cm $< r <$ 276 cm, is the large tracking device known as the Central Tracking Chamber or the CTC. The CTC is a "large

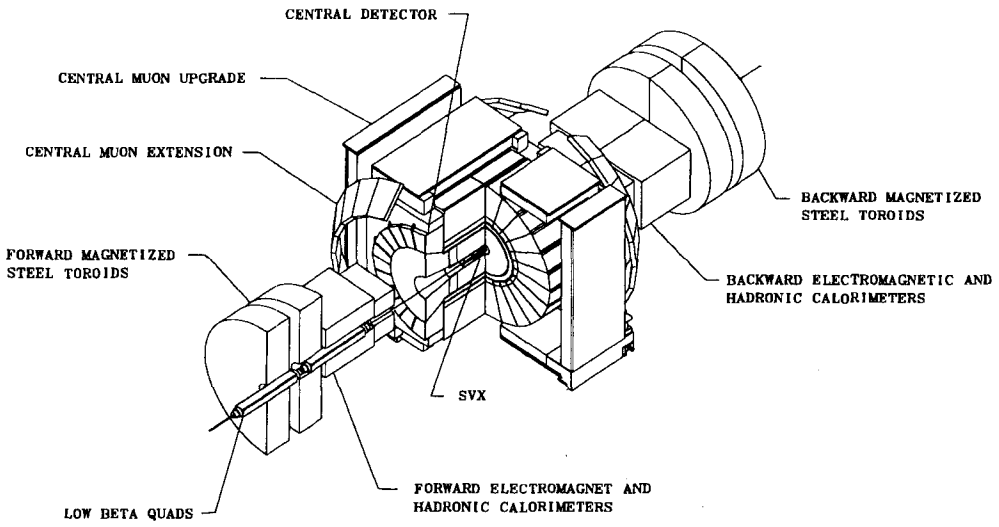

Figure 2.2: The CDF detector in isometric view. The distance between forward and backward magnetized toroids is 26.2 m.

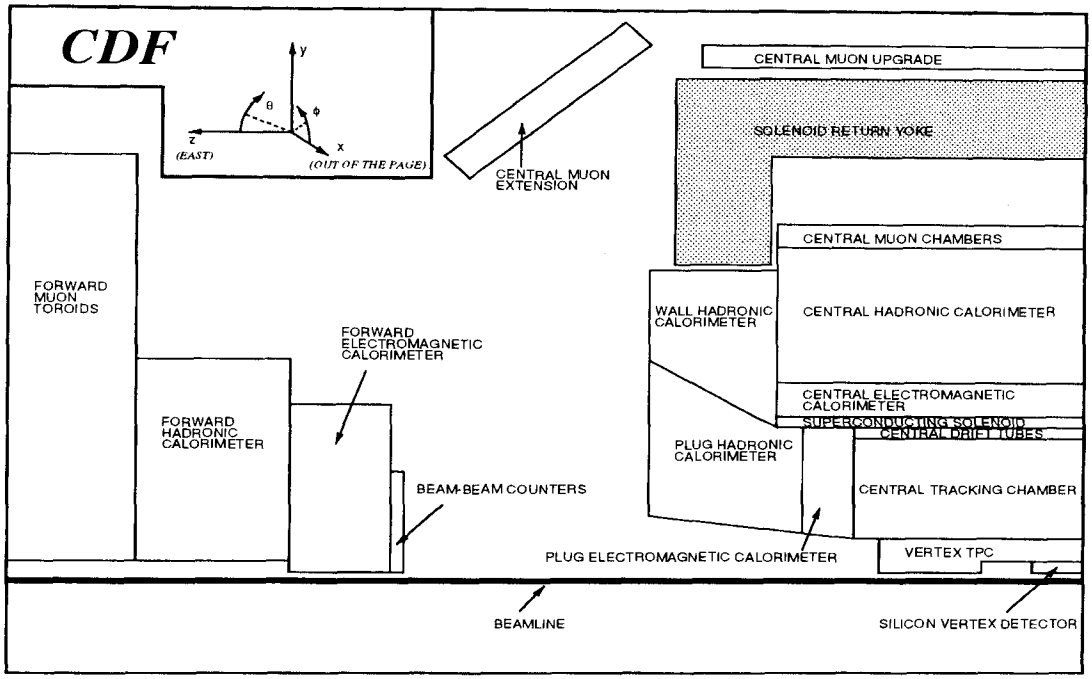

Figure 2.3: The CDF detector in cutaway view (quadrant).

cell" drift chamber with an active radius of 1.5 m. Figure 2.5 is an end view of the CTC endplate showing the arrangement of drift cells. The CTC is a 3-dimensional tracking detector and has 9 superlayers divided into 5 layers of axial wires and 4 layers of stereo wires [13]. Each axial superlayer has 12 wires and each stereo superlayer has 6 wires, giving a total of 84 measurements along the track. The CTC covers the angles $40° < \theta < 140°$ which completely covers the region of muon detectors described later. The axial layers provide r-ϕ information with a precision of 150 μm per measurement and a full determination of track curvature and axial direction. Each cell of the stereo layers has $\pm 3°$ stereo angle with respect to the beam line to enable determination of the polar angles of tracks. The CTC provides a transverse momentum (Pt) resolution

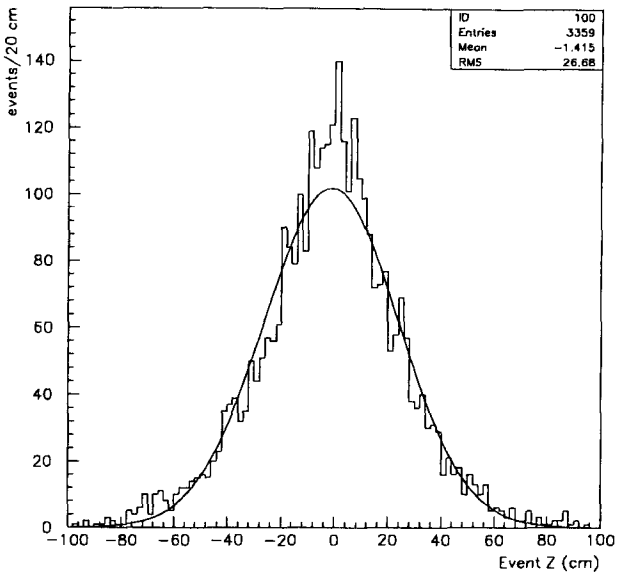

Figure 2.4: Event z vertex distribution of the typical events obtained by using the VTX.

of $\delta Pt/Pt = 0.002 \times Pt$, where Pt is in GeV/c.

2.4 Muon Chamber

The CDF muon system in the central region consists of the central muon system (CMU), the central muon extension (CMX) and the central muon upgrade (CMP). The CMX and the CMP are upgrades for the 1992-1993 run. The CMU and the CMP cover $0.00 < |\eta| < 0.65$ and the CMX covers $0.65 < |\eta| < 1.00$. Since we use only the CMU and the CMP in this analysis, the CMX will not be discussed further. The CMU is 3.7 m from the beam line, separated from the interaction region by approximately 5 hadronic absorption lengths of the CDF central calorimeter. The CMU is grouped in 15° wedges in ϕ and each wedge has 3 muon chambers [14]. A CMU muon chamber has 16 drift cells divided into 4 layers and 4 towers. Figure 2.6 [15] shows one wedge of the CMU with the relative positions of calorimeters . The CMU chambers use drift-

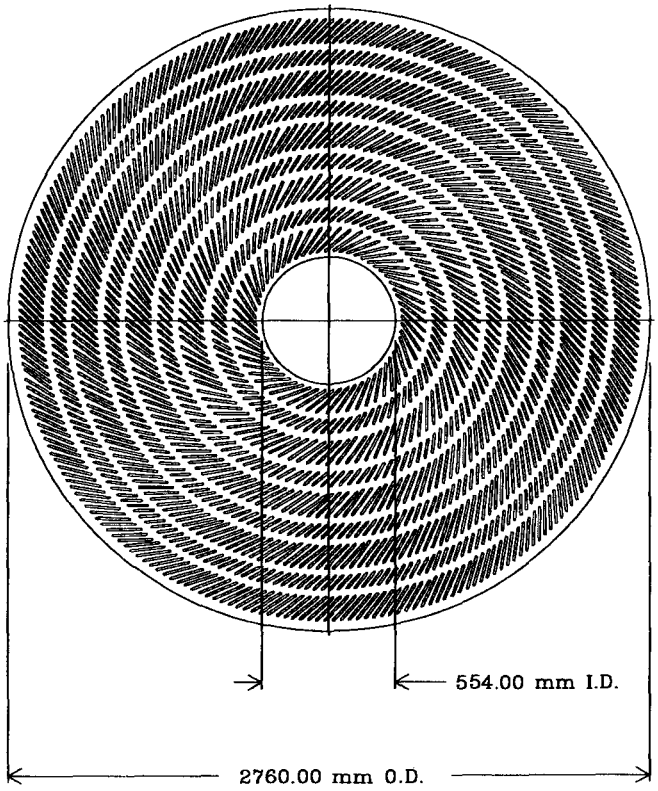

Figure 2.5: An end view of the CTC endplate.

time to determine r-ϕ information and charge-division to determine z information. The CMU provides an estimate of track Pt by the measurement of angle α between a particle track and the radial line passing through the sense wires. Figure 2.7 [16] shows a transverse projection of a track and we can derive the relationship between α and β, where β is the angle of deflection due to the magnetic field. The relation is

$$D\sin(\alpha)=L\sin(\frac{\beta}{2}) \tag{2.1}$$

where D=3470 mm is the distance from the interaction point to the bottom of the muon detector and L=1440 mm is the radius of the solenoidal magnetic field. The angle β can be related to track Pt, which is

$$\sin(\frac{\beta}{2})= \frac{eLB}{2Pt} \tag{2.2}$$

where B=1.5 T is the magnitude of the magnetic field. Equations (2.1) and (2.2) when combined give track Pt. The α is measured from the difference in drift times, δt, which is given by

$$\delta t=H\alpha/v$$

where H=55 mm is the separation of the sense wire layers, and v is the drift velocity of the ionization electrons. Figure 2.10 shows the relative sense wire positions. The momentum resolution of the CMU is $\delta Pt/Pt = 0.6$ ($Pt < 100$ GeV/c), which is crude, but adequate for triggering purposes.

The CMP muon chambers detect muons which penetrate an additional 60 cm of steel after the CMU. This steel provides an additional 3 absorption lengths, and

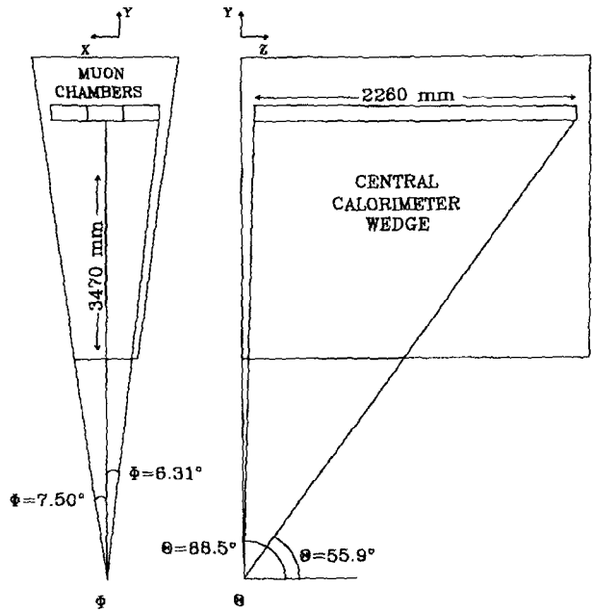

Figure 2.6: One wedge of the CMU.

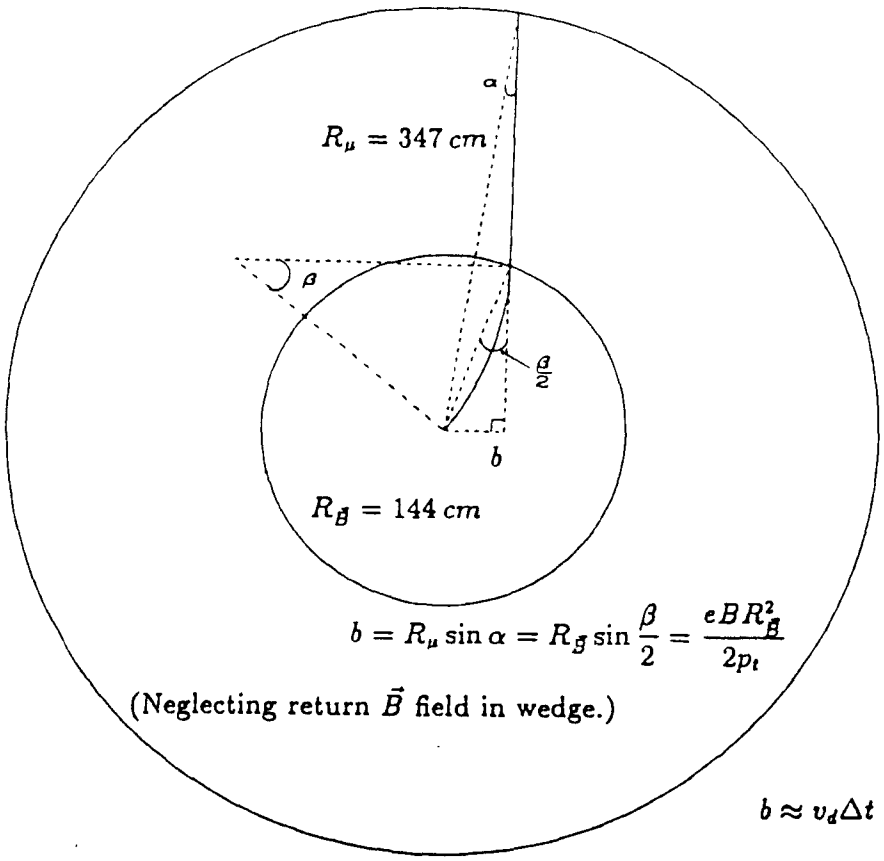

Figure 2.7: Transverse projection of a charged particle track. Within the inner circle of radius L=1440 mm is a 1.4 T magnetic field. The outer radius D=3470 mm represents the bottom sense wire plane of the central muon drift chambers.

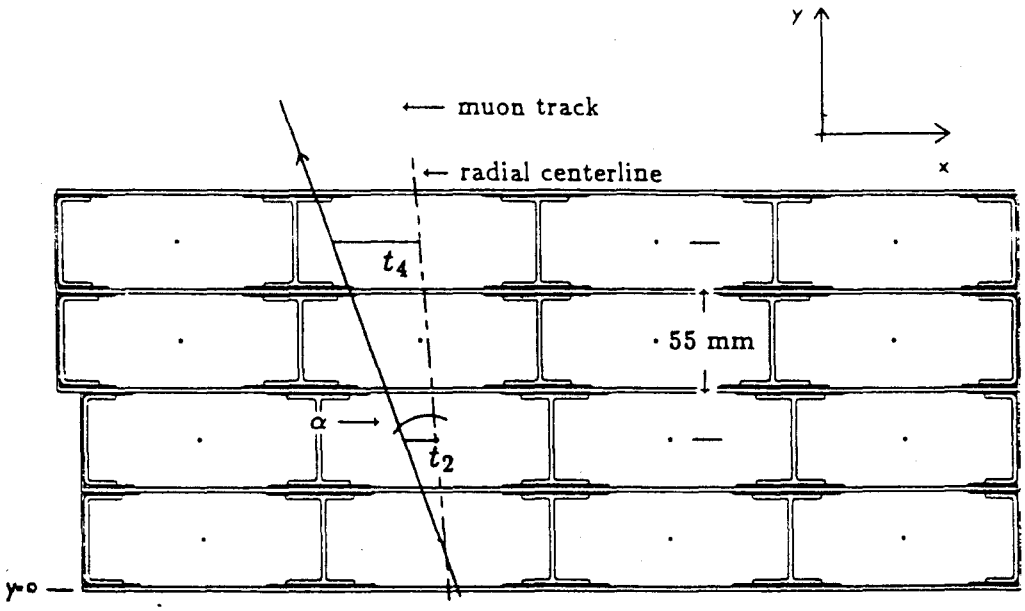

Figure 2.8: An end view of a CMU chamber.

signals in the CMP therefore represent a 95% reduction in punch-through backgrounds relative to the CMU. Muon backgrounds can therefore be reduced by an additional factor of 20 by requiring muons to be reconstructed both in the CMU and the CMP.

The CMP chambers are rectangular aluminum tubes 2.54 cm by 15.24 cm in cross section and 6.4 m long [17]. Those CMP chambers form a four sided box around the CDF detector. On the two sides of the detector, there are steel walls at a horizontal distance of about 5.4 m from the interaction point. On the top and bottom, the return yokes for the solenoid provide the steel and mounting frame at a vertical distance of about 4.7 m from the interaction point. The CMP provides only r-ϕ information and is not used to measure track Pt.

We consider a good muon to be a coincidence between a good reconstructed muon stub in the CMU or CMP and a track found in the CTC with certain restrictions on the "goodness" of the match. In the final analysis, the kinematics of the CTC track are then taken to represent the muon kinematics. The details of track matching between the CTC and muon stub will be discussed in Section 3.3 and 4.2.

2.5 The Silicon Vertex Detector

The SVX is a silicon microstrip detector designed to provide precision tracking information near the primary interaction point.

The whole SVX consists of two axial barrels, located symmetrically around the beam pipe on either side of the collision point. Figure 2.9 is an isometric view of one barrel of the SVX. Each barrel consists of 4 radial layers of silicon microstrips and each layer has 12 faces called "ladders". A ladder is a group of microstrip detectors electrically joined in series and Figure 2.10 shows one of the ladders of layer 2. The

ladder substrates are fabricated of Rohacell, a light weight foam, and reinforced with carbon fiber strips, and this assembly allows us to know the silicon detector position with an accuracy of 2.5 μm. Table 2.1 has basic parameters of the SVX and Table 2.2 shows the geometrical specification of the detector [18].

The silicon detectors used in this device are p-n junction semiconductor devices. A charged particle leaves an ionizing signal and if the junctions are reverse biassed, this charge is collected on the localized strips. For layers 0,1 and 2 strip, pitch is 60 μm and for layer 3 it is 55 μm.

The strips are DC coupled to a custom readout chip [19] which is directly bonded at the end of a ladder. The chips are mounted on readout hybrids and the four layers are bussed up to an interface hybrid called the port card. The signals go to the port card and can be read out by cables which pass through the SVX barrel and out of the VTX. The charge recorded on a given strip is used in an offline analysis to localize track trajectory with precision of order 10 μm.

Tracking Algorithm

A track is a trajectory of a charged particle and it is a helix inside the magnetic field. To represent a helical track, we need 5 track parameters, and the customary choice is $\cot\theta$, impact parameter, z, ϕ and curvature. A least squares fitting procedure is used to reconstruct tracks from the detector hit information.

The SVX tracking algorithm uses a "progressive method" [20] which starts from the CTC fit results, and improves the fit "progressively" by adding SVX hit informations and refitting of each of the 4 SVX layers. A track is extrapolated in from the CTC along a "road" which narrows with each near layer of the SVX. If an SVX hit

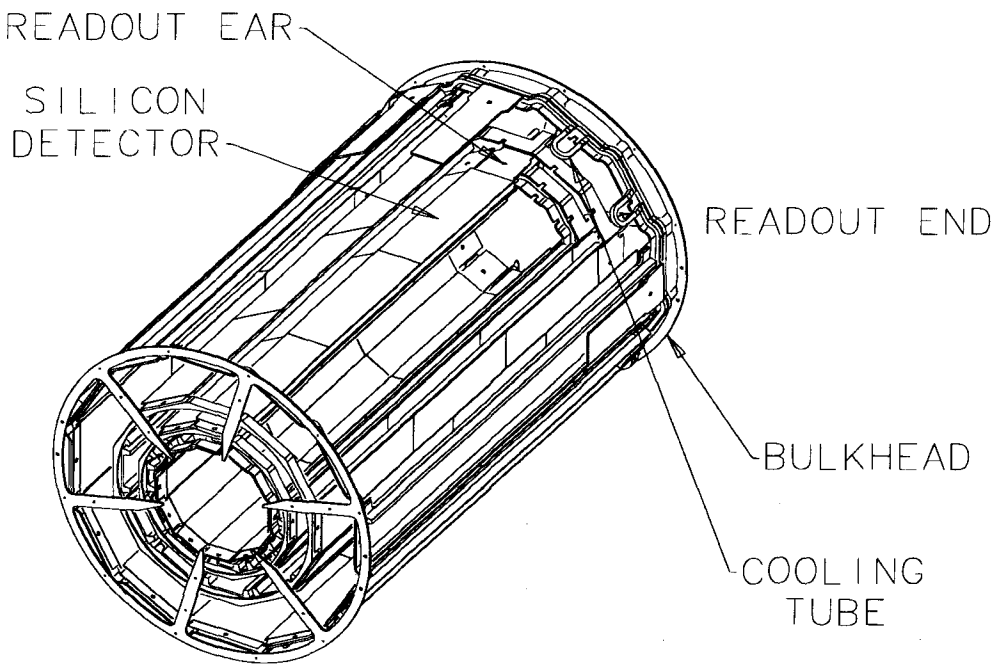

Figure 2.9: Isometric view of one barrel of the SVX.

is found within the road, the track parameters, the track covariance matrix and the track χ^2 are updated, including effects of multiple Coulomb scattering in the SVX material. The fit is controlled by a χ^2 defined as

$$\chi^2 = \chi^2_{CTC} + (\vec{p}_{SVX} - \vec{p}_{CTC})^T C^{-1} (\vec{p}_{SVX} - \vec{p}_{CTC}) + \sum_{layer} \frac{(x_{track} - x_{cluster})^2}{\sigma^2_{cluster}}$$

where $\vec{p}$ is the vector of track parameters, C is the track covariance matrix including multiple scattering, and x is the local coordinate on the SVX layer.

If there is more than one hit in the road, more than one candidate is reconstructed and the tree of candidates is fully expanded down to the innermost layer. The best track candidate is selected based on the final χ^2, starting with 4 hit candidates and proceeding to 3 hit and 2 hit candidates in turn, if necessary [21].

This procedure produces track parameters and a covariance matrix defined with respect to the detector origin. Since the location of the primary vertices vary event by event, we calculate a primary vertex for each event and recalculate track parameters and their covariance matrix with respect to that vertex.

The covariance matrix of the least squares track fit yields measured errors for the track parameters. The 3 main contributions to the uncertainty of track parameters are the intrinsic detector resolution, multiple scattering and the primary vertex finding resolution. The final values for the resolution are discussed in the next section.

Primary Vertex Finding Algorithm

The primary vertex is found in a two step process. The first step is calculation of x and y of the vertex averaged over a complete run. A D-ϕ correlation algorithm [22] formulates impact parameters of tracks as function of the slope of the beam and

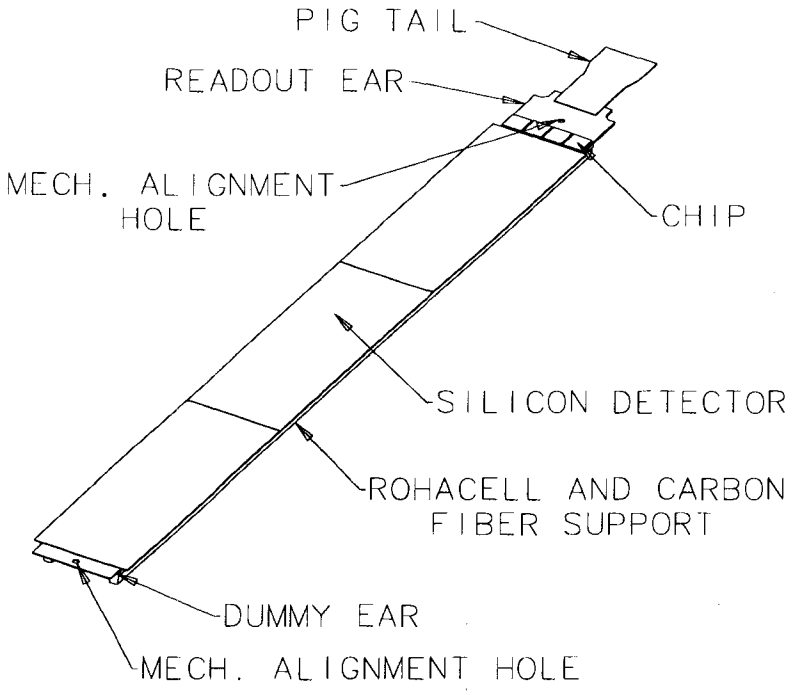

Figure 2.10: One ladder of layer 2 of the SVX.

beam position at z=0. Then the x and y of the beam position can be obtained by minimizing χ^2 of measured impact parameters of the SVX tracks.

With the average run by run beam position available, the event by event beam position is found by the routine VXPRIM [23]. For each event, the VXPRIM uses those run dependent x and y beam positions, along with the event z from the VTX, as the seed value of the primary vertex. VXPRIM calculates the event primary vertex by expanding tracks linearly at a point close to the seed vertex and repeating an iterative vertex fit. Figure 2.11 shows the resolutions of primary vertex measurements in both x-y and z. We conclude that these algorithms can measure the position of the primary vertex with an event-by-event precision of about 25 μm in x-y. The track parameters and covariance matrix are then recalculated with respect to the event primary vertex.

Performance

Figure 2.12 is an r-ϕ display of the SVX information for a typical event. The dodecahedra are the end-on views of the 4 SVX layers. Height of markers are proportional to integrated charge on the strips and track trajectories through 4 layers can be recognized by eye. The typical occupancy of the SVX is about 7% and signal-to-noise ratio is about 9 : 1 for minimum ionizing particles in case of normal incidence.

The hit efficiency is studied by counting tracks found by the CTC which extrapolate into the SVX four layer tracking volume [24]. The hit efficiency measured in this way depends on track quality and pattern recognition, and cannot really be isolated from track efficiency and resolution. Typical measured efficiencies are 93% for layer 0,1,2 and 91% for layer 3, where these numbers include effects of dysfunctional strips

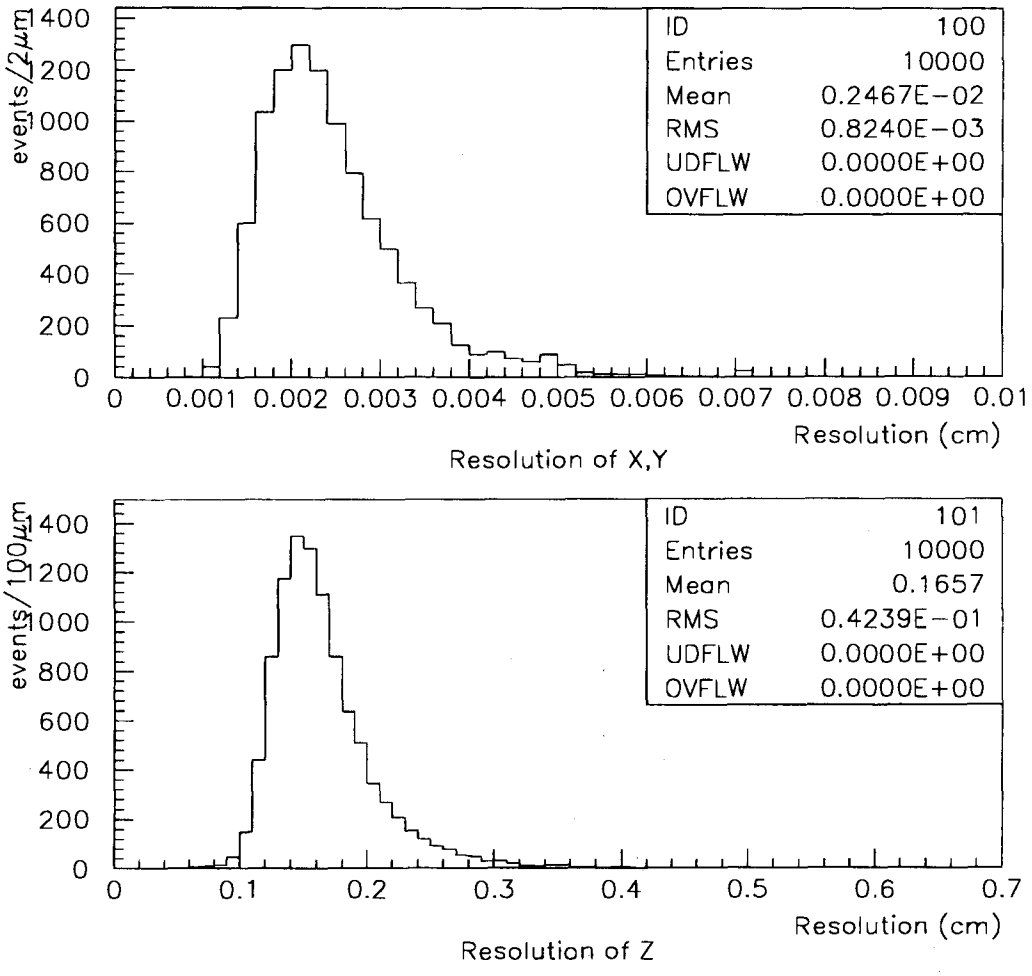

Figure 2.11: Resolution of measured primary vertex by VXPRIM for x-y plane and z direction.

as well as dead regions between detectors.

Track finding efficiency is studied by starting with well reconstructed CTC tracks which extrapolate into the SVX fiducial volume [25] and pass through at least 2 SVX layers. Using this denominator, we measure an efficiency of 98%. Of these found tracks, 70.5% have 4 associated hits, 23.0% have 3 associated hits and 4.5% have 2 associated hits.

The crucial track parameter for this thesis is the impact parameter. Figure 2.13 shows the measured impact parameter resolution as function of track Pt. As we will show in Chapter 6, the impact parameter of B decay products ranges between 0 and several hundred microns. To measure impact parameter with high precision, the resolution should be less than a few tens of microns. As seen Figure 2.13, the resolution is about 23 μm for 10 GeV/c tracks , which we will use for the analysis. The resolution of the impact parameter depends on detector resolution, multiple scattering and the primary vertex resolution. The intrinsic impact parameter resolution of the SVX is of order 10 μm, independent of track Pt and depends on geometry and the resolution of the silicon microstrips. The mean resolution of primary vertex finding is about 25 μm as seen in Figure 2.13. Figure 2.15 shows that at low Pt, the contribution from multiple scattering is dominant, but at high Pt its contribution vanishes and primary vertex finding error and intrinsic track error become dominant. The distribution can be parameterized as

$$\sigma_D = \sqrt{\sigma_0^2 + (\frac{\sigma_{MSC}}{Pt})^2}$$

where σ_0 is resolution due to intrinsic resolution plus primary vertex finding resolu-

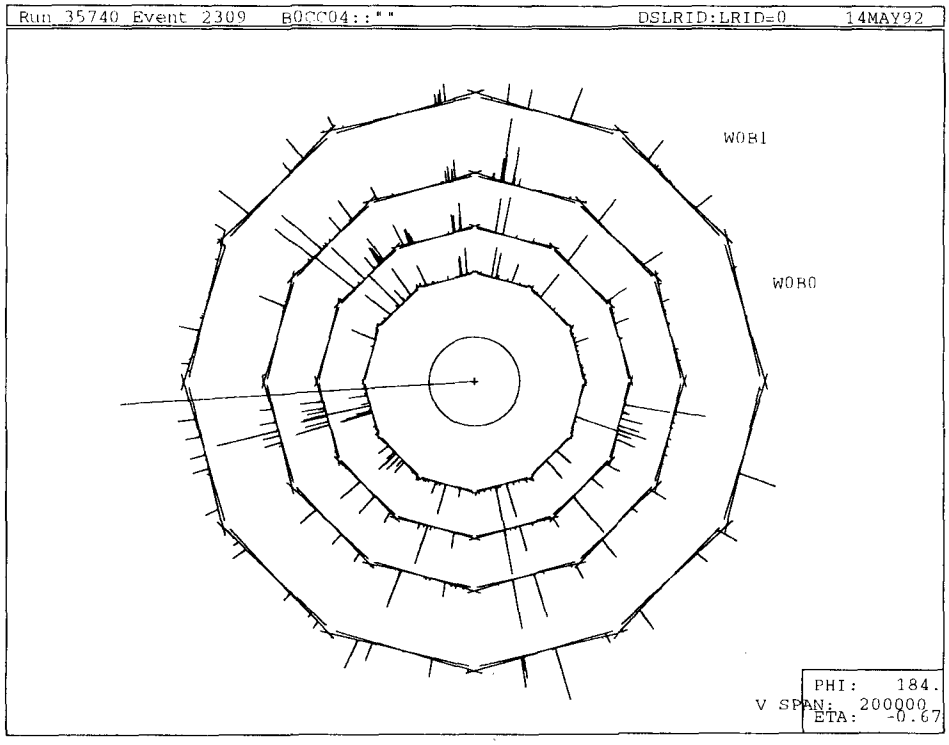

Figure 2.12: SVX event display for a typical event.

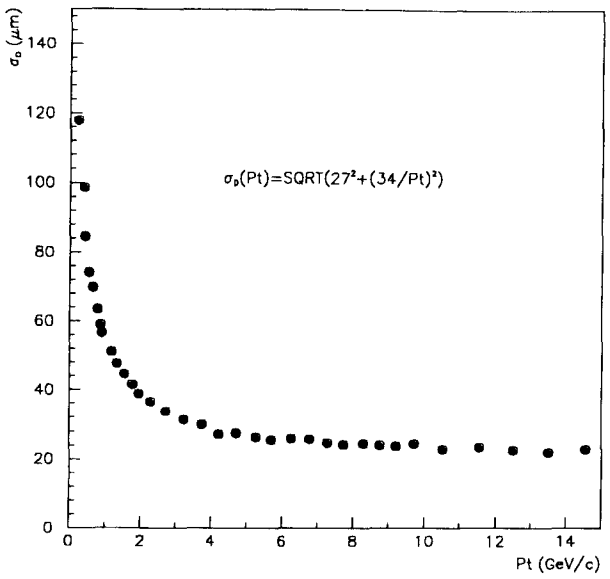

Figure 2.13: Measured impact parameter resolution.

tion, and σ_{MCS} normalizes the multiple scattering contribution, which increases at low Pt. Fitting gives σ_0=27 μm and σ_{MCS}=34 μm.

Radiation Damage

The performance of the SVX readout chips is degraded by exposure to ionizing radiation. A radiation monitoring system was set up in CDF to measure the radiation dose and abort the beam in case of large doses. Three PIN silicon diodes were placed around the beam pipe to measure instantaneous minimum ionizing particle rates. Two Beam Loss Monitors (BLM) were set up at opposite ends of CDF, near the beam pipe, to measure ionizing dose levels. The BLM is a sealed glass ion chamber with very low leakage currents. For cross calibration several thermo-luminescent dosimeters (TLD) were placed near the BLMs and extracted about once per month. Figure 2.14 shows estimated radiation dose at layer 0 [26], which is the closest one to the beam. The integral dose is about 16 kRad. The signal-to-noise ratio went down to 6.5 : 1 for the

innermost layer by the end of the run with some effects on the performance of the SVX. The measured hit efficiency went down to 89% (layer 0), 85% (layer 1), 91% (layer 2) and 89% (layer 3). For the data taken near the end of the run, we measure an overall efficiency of 97% compared to 98% at the beginning. The impact parameter resolution also decreases slightly due to the radiation damage. Figure 2.15 shows the change of the resolution for the 10 GeV/c tracks as a function of run numbers.

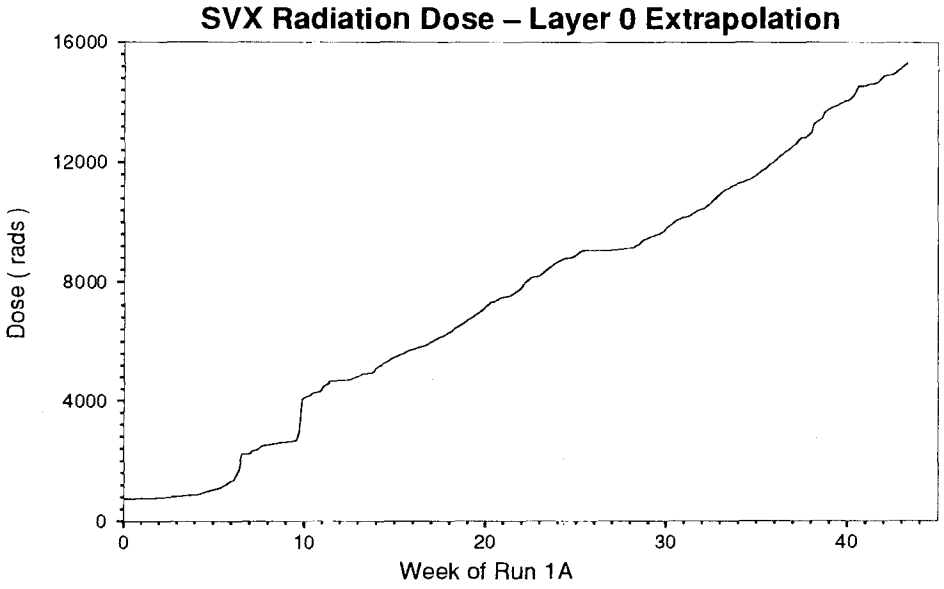

Figure 2.14: The SVX radiation dose.

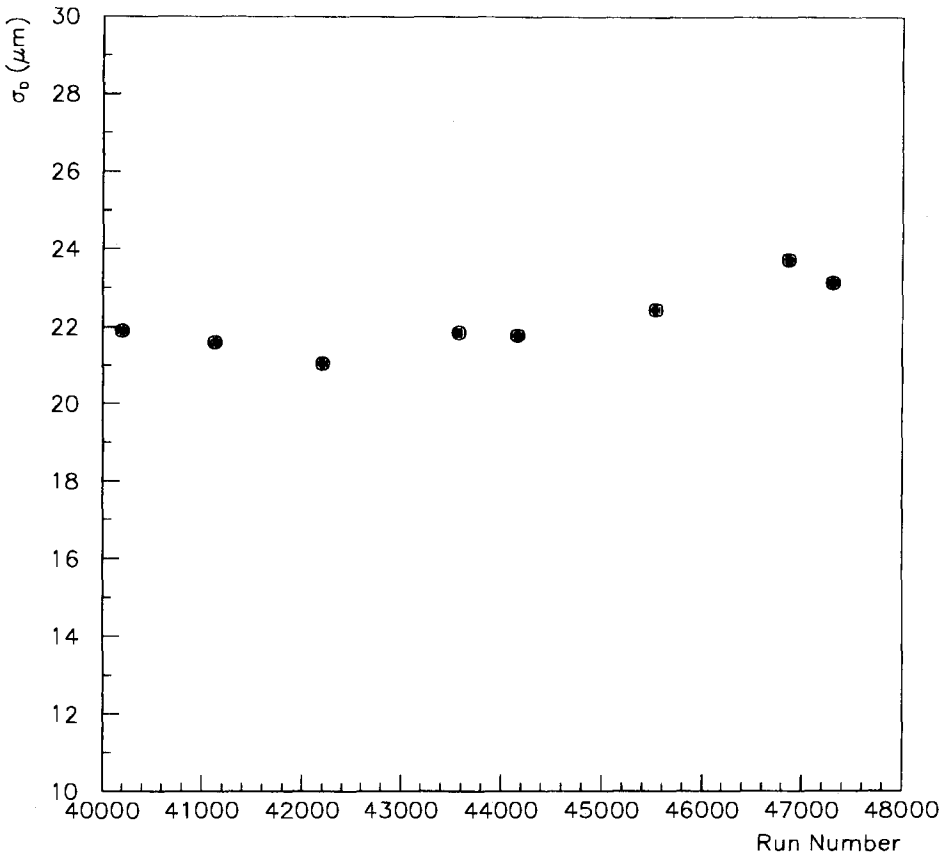

Figure 2.15: Change of impact parameter resolution due to radiation damage for high Pt tracks (Pt >10 GeV/c).

Number of layers:	4
Inner/Outer radii:	3.005 cm/7.866 cm
Strip Pitch:	60 μm layers 0-2, 55 μm layer 3
Active Length:	51 cm (2×25.5 cm with a 2.15 cm gap
Resolution:	asymptotic impact parameter=10μm
Technology:	single sided DC coupled silicon microstrips
Front end readout:	SVX Revision D IC with sparse scan
Signal to noise ratio:	9–10 for normal incidence, most probable MIP
Number of channels:	46080
Number of chips:	360
Power dissipation:	$\approx$ 200 mW/chip
Total power:	$\approx$ 100 watts (includes drivers, regulators)
Cooling:	chilled water (14°C)
Beam collision period:	3.5 μsec
Support materials:	rohacell, beryllium, alumina, aluminium nitride
Segmentation:	projective wedge (30° azimuth) = 1 readout unit.
DAQ system:	RABBIT + FASTBUS
Readout time:	1–2 milliseconds
Typical occupancy:	7%
Radiation exposure:	15–20 KRad over lifetime

Table 2.1: Basic parameters of the CDF Silicon Vertex Detector.

a: Barrel geometrical parameters

	Radius [cm]	Length [cm]
Layer #1	3.005	25.6
Layer #2	4.256	25.6
Layer #3	5.687	25.6
Layer #4	7.866	25.6

b: Silicon crystal geometrical dimensions

	Width [μm]	$\pm$	Length [μm]	$\pm$	Thickness [μm]	$\pm$
Layer #1	16040	50	85000	50	300	15
Layer #2	23720	50	85000	50	300	15
Layer #3	31400	50	85000	50	300	15
Layer #4	42930	50	85000	50	300	15

c: Characteristics of the active area of the detectors

	Width [μm]	Pitch [μm]	Readout strips	Number of chips	Length [μm]
Layer #1	15360	60	256	2	84500
Layer #2	23040	60	384	3	84500
Layer #3	30720	60	512	4	84500
Layer #4	42240	55	768	6	84500

d: Coverage in polar angle

	Theta $\pm$	Eta $\pm$
Layer #1	6.3	2.9
Layer #2	9.5	2.5
Layer #3	12.6	2.2
Layer #4	17.2	1.9

Table 2.2: The SVX geometrical specification.

Chapter 3

Data Set

The data set used in this analysis was recorded in the period from April, 1992 to April, 1993, and is called the CDF Run Ia. The total delivered luminosity during that period is about 27 pb^{-1}. Among these about 19 pb^{-1} of data was recorded by CDF. All 19 pb^{-1} has been processed for the reconstruction and classified into several subsets called "Streams", where a Stream is a set of data selected according to physical contents like muons, electrons, jets and so on. CMU1_3P is a Stream containing low momentum inclusive muons, which we use for this analysis. In this chapter we discuss the collection of the data, starting from colliding beams, and ending with a restricted sample for this study.

3.1 Data Taking

All of the CDF data is derived from $p\bar{p}$ collisions in the Tevatron. 6 protons and 6 anti-protons bunches are counter-rotated and collided every 3.5 μsec. The instantaneous luminosity is the flux-like quantity used to measure the rate at which protons and anti-protons are provided for collision. It is given by

$$\text{Instantaneous Luminosity} = \frac{N_p N_{\bar{p}} C}{4\pi\sigma^2}$$

where N_p and $N_{\bar{p}}$ are the number of protons and anti-protons per bunch, C is the bunch crossing rate, and σ is the RMS width of the beam spot. The CDF luminosity is measured using the beam-beam counters (BBC). They consist of two planes of scintillation counters covering the angular range of 0.32° to 4.47° in both the forward and backward directions. Hits in both counters that arrive coincident with the particle bunches crossing through the detector serve as the primary luminosity monitor. The rate of coincidences in these counters, divided by the effective cross section of the counters, gives the luminosity [27].

For the 1992 and 1993 run, the typical instantaneous luminosity was measured to be about $5\times\ 10^{30}\ cm^{-2}s^{-1}$. The total cross section measured by CDF at $\sqrt{s}$ =1.8 TeV is about 50 mb [28]. Therefore about 250,000 collisions happen every second, an impossible data rate for any data acquisition system. Since there is limit in the data acquisition, we need to adopt a system selecting events of interest before an event is recorded to magnetic tapes. That is called a trigger system and CDF has 3 stages of triggers. Each stage is called a Level and each event is tested sequentially through 3 Levels from the Level 1 to the Level 3.

The idea behind the multi-level trigger structure is to introduce as little bias as possible at the lower levels, with the goal of reducing the rate to a point where the next level can do a more sophisticated analysis without incurring significant deadtime. If an event is to be identified as one of interest, it is recorded to a magnetic tape. The CDF data acquisition system has an approximately 6 Hz limit for writing to

magnetic tapes. This means the trigger selects 1 event out of every 41,500 collisions.

3.2 The Central Muon Trigger

There are several kinds of triggers at each trigger Level in order to identify and select different kinds of final states. In many cases an event can pass several triggers at the same time at a certain Level. Since the triggering is not perfect, some events which should be kept are lost. For that reason, the measurement of cross sections requires knowledge of trigger efficiencies. To measure the trigger efficiency for the central muon trigger, we select events which have come through the trigger level in question via an independent trigger. The trigger efficiency is the fraction of those selected events which contain an identified muon and actually pass the central muon trigger. For our multilevel trigger we require events to pass previous levels, so the total trigger efficiency is multiplicative.

The inclusive muon sample for this analysis passes the Level 1 trigger called CMU_CMP_6PT0. The CMU_CMP_6PT0 requires hits both in the CMU and the CMP and that the track Pt measured by the CMU should be greater than 6 GeV/c. If a track is reconstructed in the CMU, the CMP hit information is compared to the expected CMP hits of the extrapolated CMU track, based on information derived from the simulation studies. If at least 2 hits are found in the expected CMP drift cell, the event satisfies the CMU/CMP matching requirement. As mentioned in Section 2.4, Pt in the CMU is measured by the time difference between wires. Wire hit information is sent to the hardware trigger and if satisfying $\mathrm{MIN}(|t_4 - t_2|, |t_3 - t_1|) < t_{max} = 40\ ns$ (see Figure 2.10), the track has $Pt > 6$ GeV/c and the event passes the Level 1 muon trigger. Figure 3.1 is the Level 1 CMU_CMP_6PT0 trigger efficiency as

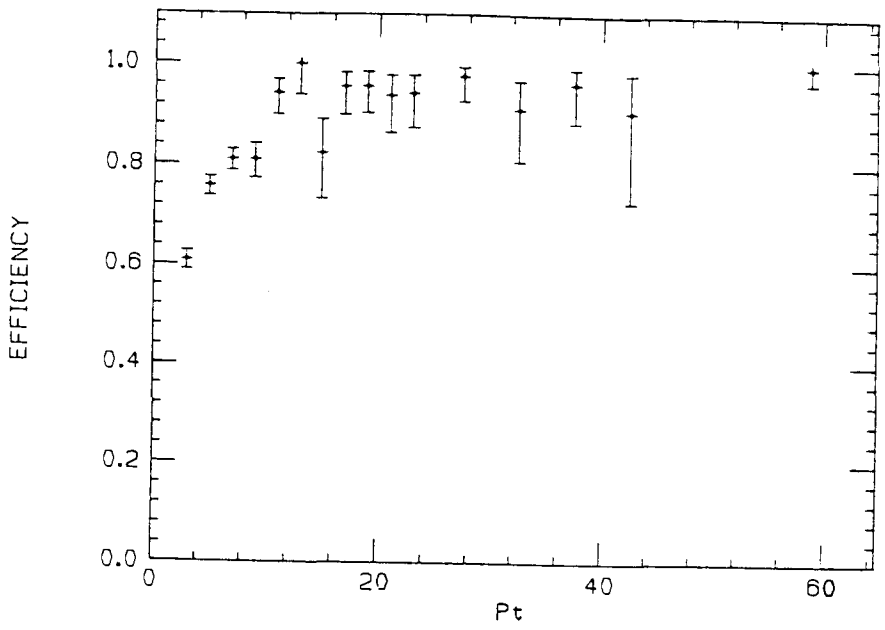

Figure 3.1: The Level 1 trigger efficiency for the inclusive muon sample.

a function of muon Pt [29].

The Level 2 trigger for the data sample for this analysis is called CMUP_CFT_9_2_5DEG. It requires a Level 1 trigger. Then it uses track information provided by the Central Fast Tracker (CFT), which is a hardware track processor using fast time information from the CTC. The momentum resolution of the CFT is $\delta Pt/Pt = 0.035 \times Pt$ (Pt in GeV/c), which is significantly worse than the offline reconstruction, but better than the Level 1 muon trigger and adequate at our Level 2 trigger. The CFT efficiency is 93.5% for tracks with Pt above 10 GeV/c [30]. If there is any CTC track which differs in ϕ by less than 5° from the track reconstructed in the CMU and exceeds Pt = 9.2 GeV/c measured by the CFT, the event passes the Level 2. Figure 3.2 is the Level 2 CMUP_CFT_9_2_5DEG trigger efficiency [31].

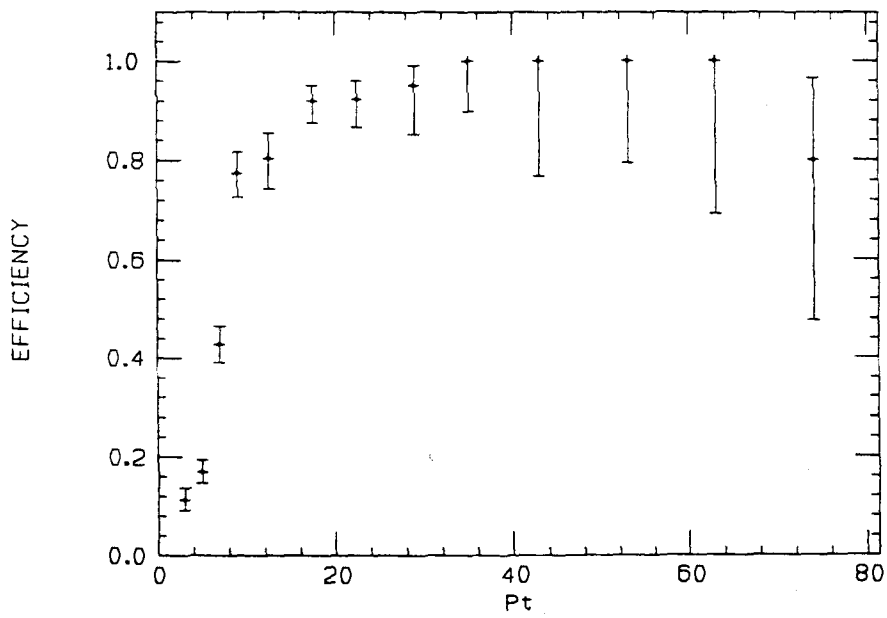

Figure 3.2: The Level 2 trigger efficiency for the inclusive muon sample.

The Level 3 trigger is a FORTRAN program running online during data taking and MUO1_CMU_CMP_7PT5 is the Level 3 trigger for the muon sample. The Level 3 trigger first verifies the Level 2 result by checking the there is a track from the CFT with Pt above the Level 2 threshold. Then a more complicated 2-dimensional reconstruction algorithm calculates track Pt again and only tracks with Pt greater than 7.5 GeV/c pass the Level 3 trigger. Another requirement is that the difference of the x intercept (muon coordinate system) between the extrapolated CTC track and muon stub should be less than 10 cm. The Level 3 MUO1_CMU_CMP_7PT5 trigger efficiency is 0.992 [32] and flat for muons with $Pt > 10$ GeV/c.

3.3 Data Production

Events passing a Level 3 trigger are selected for readout. The data written to tape is relatively low level information such as channel identification and signal magnitudes in electrical units for many detector channels. The conversion of this huge amount of raw data into physical quantities like track parameters and jet energy is called the "data production". During this step, for instance, the full 3-dimensional CTC reconstruction is done and a more carefully reconstructed muon stub is matched to the CTC track. After that, a χ^2 showing "goodness" of match is calculated. The definition of matching χ^2 will be described in detail in Section 4.2. The SVX tracking reconstruction is also done at this stage.

The reconstructed data is separated into a variety of "Streams" according to its physical contents. The Stream including the muon triggers described in Section 3.2 is CMU1_3P, and will form the basis of our bottom cross section analysis.

3.4 Other Data Sets

In this section we briefly discuss other data sets which play a supporting role in our analysis.

Jet Data

The study of systematic issues like backgrounds, tracking quality, and so on require huge control samples that we derived from inclusive jet data. We use a Stream called JET_20, which is made by requiring at least one jet with Et >20 GeV in an event. Most of the tracks in these jets are prompt pions or kaons coming from the fragmentation of light quarks and gluons. The fraction of heavy flavor in this sample has been studied in Ref. [33]. The charm and bottom fractions are obtained by fitting the $c\tau$ distribution of the jets and is found to be 3.36±0.80% and 1.35±0.10% for charm and bottom respectively.

Monte Carlo

It is also very useful to study simulated data, which we generate using ISAJET 6.43 [34]. The simulation is performed using the standard CDF detector simulation package called CDFSIM [35]. For jets the generation is done by using 2 parton→2 parton processes, allowing all final state partons in order to model the inclusive jet data as described.

Bottom and charm Monte Carlo samples are also generated using ISAJET 6.43. In the case of bottom production, version 6.0 of the CLEO Monte Carlo is integrated into the generator and used to re-decay the bottoms using the best world knowledge. We restrict generation to the inclusive 2 parton→2 parton process. A special version of the ISAJET routine called REJJET selects only those events that contain a bottom

or charm quark and then the CDFSIM is used for the simulation. Our bottom and charm Monte Carlo samples are obtained by using an average B lifetime [36] of $c\tau = 420\ \mu m$, a D^0 lifetime [37] $c\tau = 126\ \mu m$, and a $D^{\pm}$ lifetime [38] $c\tau = 321\ \mu m$.

Chapter 4

Event Selection

In this chapter we describe the characteristics of the CMU1_3P data set and further preparation of this data set for the cross section measurement. We apply an offline selection ("cuts") to remove backgrounds and improve the quality of muon identification and tracking reconstruction. The efficiencies of our offline selections will be discussed in Chapter 5.

4.1 Sources of Muons

The output of the data production process includes reconstructed muon candidates called central muon objects, CMUO. Each CMUO is a CTC track matched to information in a central muon detector.

The muon candidates selected as the CMUO objects have their origins in 6 main sources.

- beauty decay

Figure 4.1(a) shows the semileptonic decay of b quarks. The semileptonic decay

$b \rightarrow \mu\nu_\mu X$ occurs in 11% [39] of all bottom decays. The sequential process $b \rightarrow c \rightarrow \mu\nu_\mu X$ occurs in 9% [40] of all bottom decays. The branching ratio of direct decay is almost same as the sequential one, but the ratio of direct to sequential muons in the inclusive muon sample with applied minimum Pt cut is about 9 : 1 since the muon Pt distribution has higher average value for the case of the direct decay.

- charm decay

  Figure 4.1(b) is the diagram of the semileptonic decay of charm quarks. The semileptonic process $c \rightarrow \mu\nu_\mu X$ occurs in 9% [41] of all charm decay. The expected ratio of muons from bottom and charm in the CDF data sets has been previously studied using ISAJET Monte Carlo in conjunction with the theoretical b/c production ratio and bottom and charm fragmentation properties [42]. The conclusion of that study is that the harder bottom fragmentation leads to about five times more muons from bottom than from charm, and that this ratio is almost independent of muon Pt.

- light flavor decay

  Pions and kaons decay to muons with the branching ratio of 99.9% and 63.5% [43] respectively, and there is a significant rate of hits in the muon systems from pions and kaons which decay "in flight". Since pions constitute the overwhelming majority of particles produced in $p\overline{p}$ collisions, these decay-in-flight (DIF) muons are a significant source of muon background. The production ratio of K to π is known to be 0.28 at the Tevatron collider [44].

- Electroweak processes

  As in Figure 4.1(c), muons are also generated in the electroweak processes such as $p\bar{p} \rightarrow W \rightarrow \mu\nu_{\mu}$, $p\bar{p} \rightarrow Z \rightarrow \mu^{+}\mu^{-}$ and $p\bar{p} \rightarrow \gamma \rightarrow \mu^{+}\mu^{-}$ (Drell-Yan) [45]. Muons generated in this way are isolated and W and Z decay muons have large Pt due to the large mass of W and Z. The Drell-Yan process gives two isolated muons. In case of Z events, the invariant mass of the two muons can be reconstructed with two muons and the distribution has a peak at 91 GeV/c^2, which is the Z mass. In W events, the transverse component of the neutrino momentum can be reconstructed from the transverse energy unbalance, but the longitudinal neutrino momentum is lost, and we cannot form a true invariant mass. Instead, we use the transverse mass for the identification of W, which is defined as $M_t = \sqrt{2P_t^{mu} Et(1 - cos(\phi_{\mu} - \phi_{\nu}))}$.

- cosmic rays

  Cosmic ray muons are collected as muon trigger data when they accidentally overlap real minimum bias interactions. Cosmic rays are detected as back-to-back tracks, and since they do not come from the $p\bar{p}$ collision, their track z distribution is flat, unlike the Gaussian z distribution for real collisions. The impact parameter is generally larger than for tracks from the collision and the distribution is also flat. Finally, one leg of cosmic rays usually is poorly measured in the CTC. Since it appears to be going "backwards in time", it will have fewer recognized hits, larger residuals, a poor χ^2 and frequently a failure of 3-dimensional reconstruction in the CTC.

- fake muons

  Truly fake muon signals are produced by hadrons which pass through the calorimeter and reach the muon chamber, or by secondary hadrons produced in showering the calorimeter. The former is called non-interacting punch-through and the later is called interacting punch-through.

A significant fraction of the background can be removed by careful examination of signals from, and matching between, the CTC and muon chambers. In addition, good quality control here is necessary to ensure robust results when it comes time to fit the bottom fraction in the real muons. We now describe muon selection.

4.2 Offline Cuts

We apply to the inclusive muon sample a selection designed to remove backgrounds and improve quality while maintaining efficiency. Table 4.1 is the list of the offline cuts we applied.

We select 3 sets of muons with minimum Pt = 10, 15 and 20 GeV/c. The reason for this minimum Pt selection is motivated by the ultimate physics goals which will be discussed in Chapter 5.

To remove fake muons we use only tracks found in both the CMU and the CMP. As mentioned in Section 2.4, the additional absorber in this case reduces punch-through backgrounds by a factor of 20.

Since tracks found in the muon chamber are associated with the CTC tracks, we can construct a "matching χ^2" which measures the "goodness" of the association. The matching χ^2 is defined in the muon coordinate system, which is described in

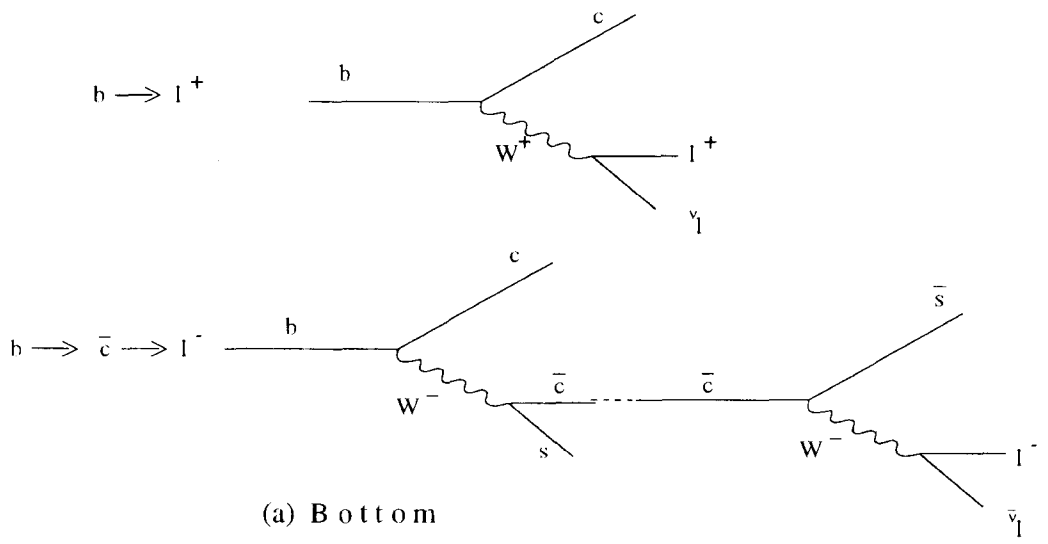

(a) Bottom

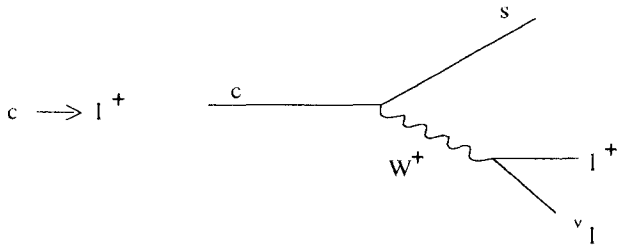

(b) Charm

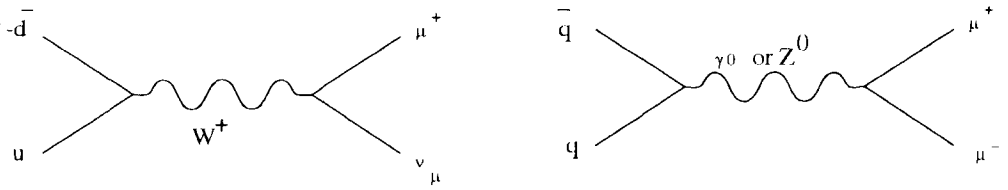

(c) Electroweak

Figure 4.1: The Feynman diagrams describing decay mechanisms of muon production.

3 sets of muons with minimum Pt=10,15 and 20 GeV/c
CMU-CMP muon
matching χ^2_x(CMU) $\leq$ 9, χ^2_x(CMP)$\leq$ 9, χ^2_z(CMU)$\leq$ 12
$\lvert z_{mu} \rvert \leq$ 30.0 cm
primary vertex finding error $\leq$ 60 μm
SVX muon
track quality cut on the CTC and the SVX tracking
$\lvert$impact parameter$\rvert \leq$ 0.06 cm
W and Z removal

Table 4.1: Offline cuts.

Figure 2.8. In the case of the CMU, the χ^2 is calculated for x-y and y-z planes, but for the CMP only the x-y χ^2 is calculated. For each plane the difference in the slope (ΔS) and the intercept (ΔI) between the corresponding muon stub and the extrapolated CTC track are combined into a χ^2 according to

$$\chi^2=(\Delta I\ \Delta S)\begin{pmatrix} \sigma_I^2 & \gamma \\ \gamma & \sigma_S^2 \end{pmatrix}^{-1}\begin{pmatrix} \Delta I \\ \Delta S \end{pmatrix}$$

where σ is the resolution including multiple scattering and track resolution and $\gamma=\rho\sigma_I\sigma_S$ is the correlation term with the correlation factor ρ. For each plane and each chamber σ and ρ are obtained as function of Pt and polar angle θ with respect to the event vertex origin [46]. For example, σ and ρ of the CMU for the x-y plane is

$$\sigma^2_{l_x}(CMU)=(13.8\text{cm}/Pt)^2\frac{0.59+0.41/sin\theta}{1-0.71/Pt}+(0.3\text{cm})^2$$

$$\sigma^2_{S_x}(CMU)=(0.131/Pt)^2\frac{0.27+0.73/sin\theta}{1-1.43/Pt}+(0.0062)^2$$

$$\rho_x(CMU)=0.87$$

Figure 4.2 is the matching χ^2 distribution for 10 GeV/c CMU-CMP muons. We use the standard CDF χ^2_x requirement of $\chi^2_x(CMU)$ <9.0, $\chi^2_z(CMU)$ <12.0 and $\chi^2_x(CMP)$ <9.0, which remove gross backgrounds from DIF and punch through, but keep real muons which have only modestly good matches due to large multiple scattering.

Cosmic ray muons are removed by requiring that the muon track be close to the $p\overline{p}$ interaction point, $|z_{mu}| < 30$ cm. Since we will use muon impact parameter to measure the bottom fraction, we require that the muon track pass through the SVX. Since the SVX covers -25.0 cm$< z < 25.0$ cm, the z_{mu} cut has already done some of this selection, but we also explicitly require that the muon is a SVX track. We will explain in Section 6.2 how the SVX requirement serves to remove DIF muons.

We need to know the position of primary vertex for each event in order to correctly measure track parameters and their covariance matrix. As mentioned in Section 2.5, the routine VXPRIM gives both the primary vertex position and its error, and we require primary vertex error < 60.0 μm.

Tracking quality cuts on both the CTC and SVX reconstruction are generally used in the CDF analysis but are especially important for this analysis because of the impact parameter fit used to measure the bottom fraction. In Section 2.5 we mentioned that the performance of the SVX is degraded due to the radiation damage.

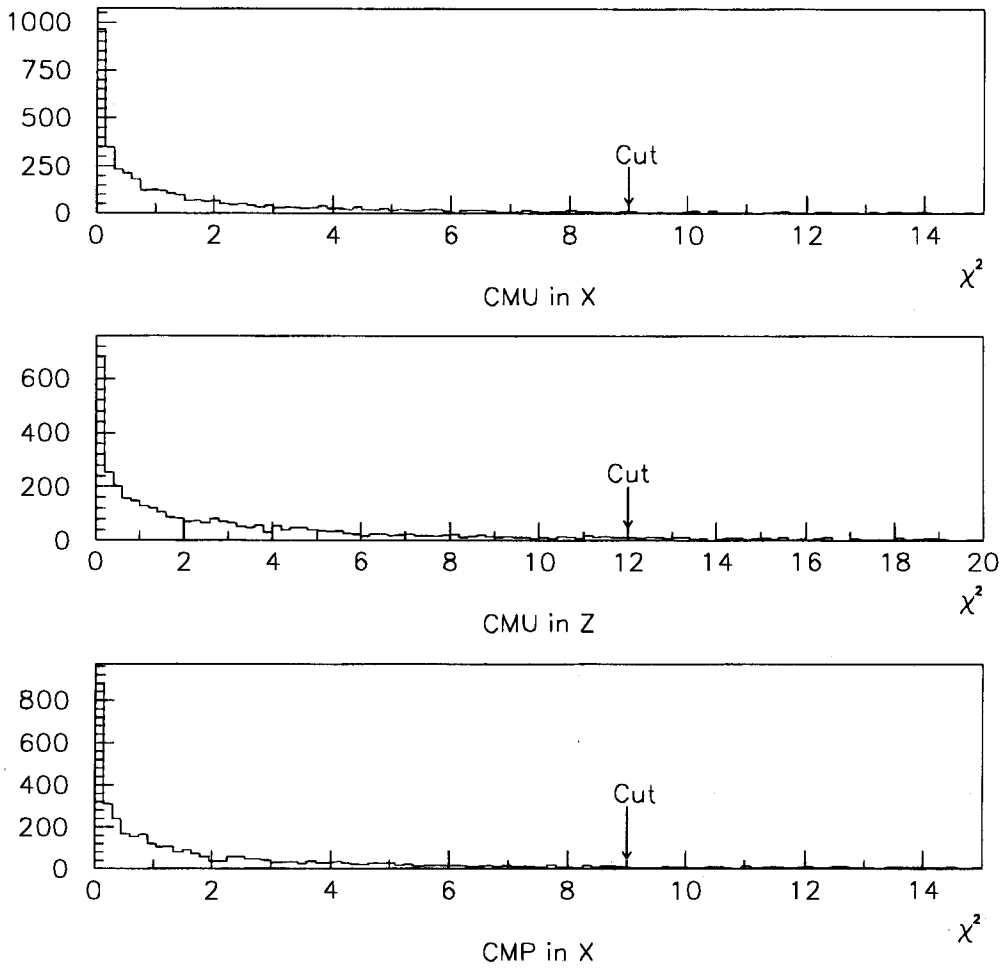

Figure 4.2: The matching χ^2 distribution between muon stub and the extrapolated CTC track for 10 GeV/c CMU-CMP muons.

The number of bad tracks increases as the run number increases due to increased radiation dose. These bad tracks affect the impact parameter distribution and bias the measurement of the bottom fraction. Track quality is therefore very important. We use only 3-dimensional tracks. For the CTC tracking, we require at least 2 axial superlayers with at least 4 hits and at least 2 stereo superlayers with at least 2 hits. For the SVX tracking we require at least 2 "good" hits associated with the SVX track and that the χ^2 per degree of freedom of the SVX tracking be less than 6.0. A good hit is defined as a hit which is not shared with another track, which has no dead channel included, and for which the charge is shared over 4 or less channels. We next require that the difference between z_{mu} and the event z is less than 5.0 cm, which rejects muons produced in events with multiple interactions. We can remove both DIF muons and cosmic rays by applying $|D_0| < 0.06$ cm. Figure 4.3 is the distribution of absolute value of the impact parameter for 10 GeV/c bottom muons with the other offline cuts applied as modeled by our Monte Carlo. It shows that only about 3% of bottom muons are removed by $|D_0| < 0.06$ cm cut.

Finally we identify W and Z bosons by requiring missing $Et \geq$20 GeV and transverse mass$\geq$20 GeV/c^2 in events with muons with $Pt >$18 GeV/c passing an isolation cut of $Et/Pt <$0.1. The missing Et is corrected for the muon Pt. For the Z removal, we reconstruct the invariant mass from two muons satisfying the same muon requirements used for W muons. An event is identified to be a Z event if the invariant mass is between 65 and 115 GeV/c^2. This cut is also effective for muons from Drell-Yan process which lie under the Z peak. Figure 4.4 shows the distributions of muon Pt before and after W and Z removal. For the two high momentum bins the difference

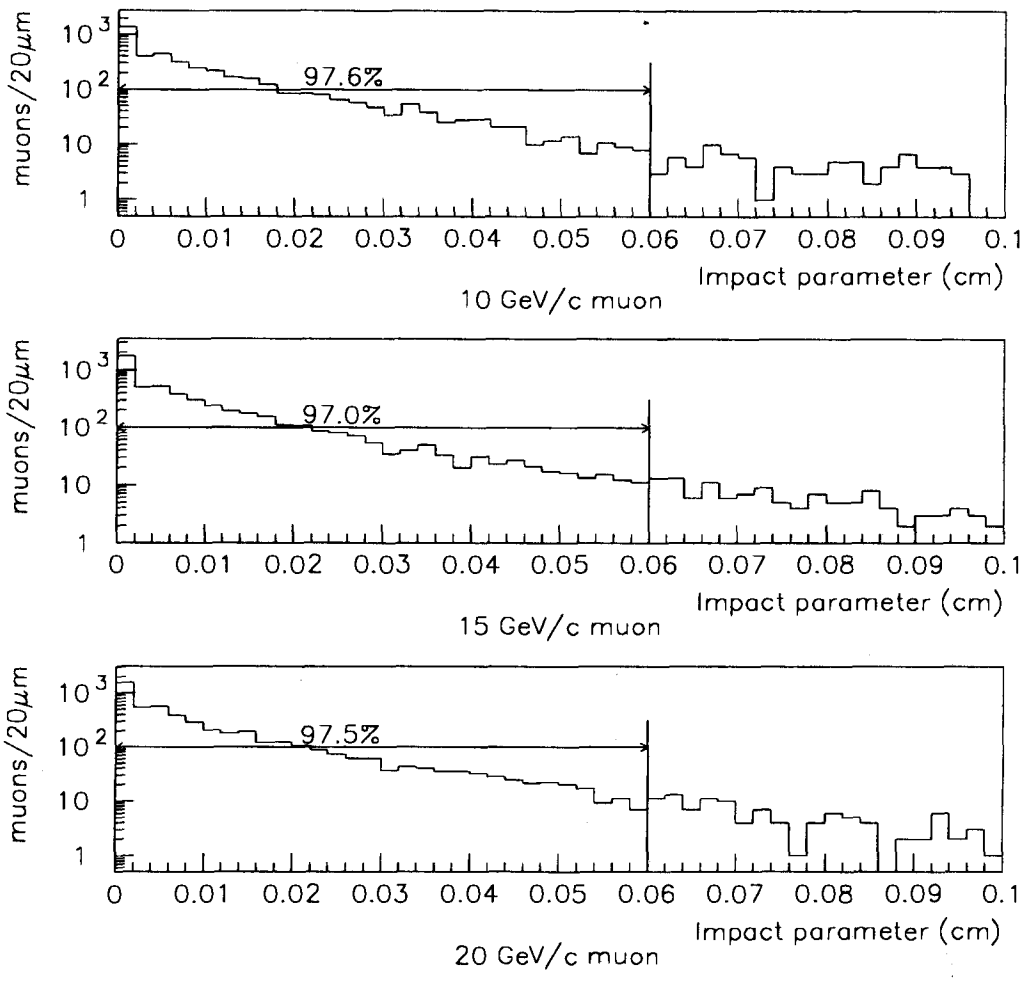

Figure 4.3: The impact parameter distribution of bottom muons with $Pt \geq$ 10,15 and 20 GeV/c.

is noticeable.

The initial number of 10 GeV/c CMU-CMP muons in the whole sample is about 320,000. This is reduced to 124,974 muons after matching χ^2 and $|z_{mu}|$ cuts are applied with reduction rates of 0.52 and 0.75 for χ^2 and $|z_{mu}|$ cuts respectively. After going through the other 5 offline cuts, there remains 84430, 15071 and 4015 muons with the Pt threshold of 10,15 and 20 GeV/c. Table 4.2 shows effects of the other 5 cuts on data size for 10 GeV/c muons.

cut	number of muons (%)
10 GeV/c CMU-CMP muon passing χ^2 and $\|z_{mu}\|$ cut	124974 (100.0)
primary vertex finding error $\leq$ 60 μm	124597 (99.7)
SVX muon	110677 (88.6)
Track quality cut on the CTC and the SVX tracking	88976 (71.2)
$\|$impact parameter$\|$ $\leq$ 0.06 cm	86842 (69.5)
W and Z removal	84330 (67.5)

Table 4.2: Effects of cuts on data size.

4.3 Estimation of Fractions of Minor Sources

In Section 4.1 we listed the sources of muons. The fraction of each source in the muon sample changes after the offline cuts are applied. When we measure the bottom fraction in the muon sample later, we will claim that the main sources of muons in the muon data after the offline cuts applied are bottom, charm, and DIF and that the other sources are negligible. To justify that claim we estimate here the fraction

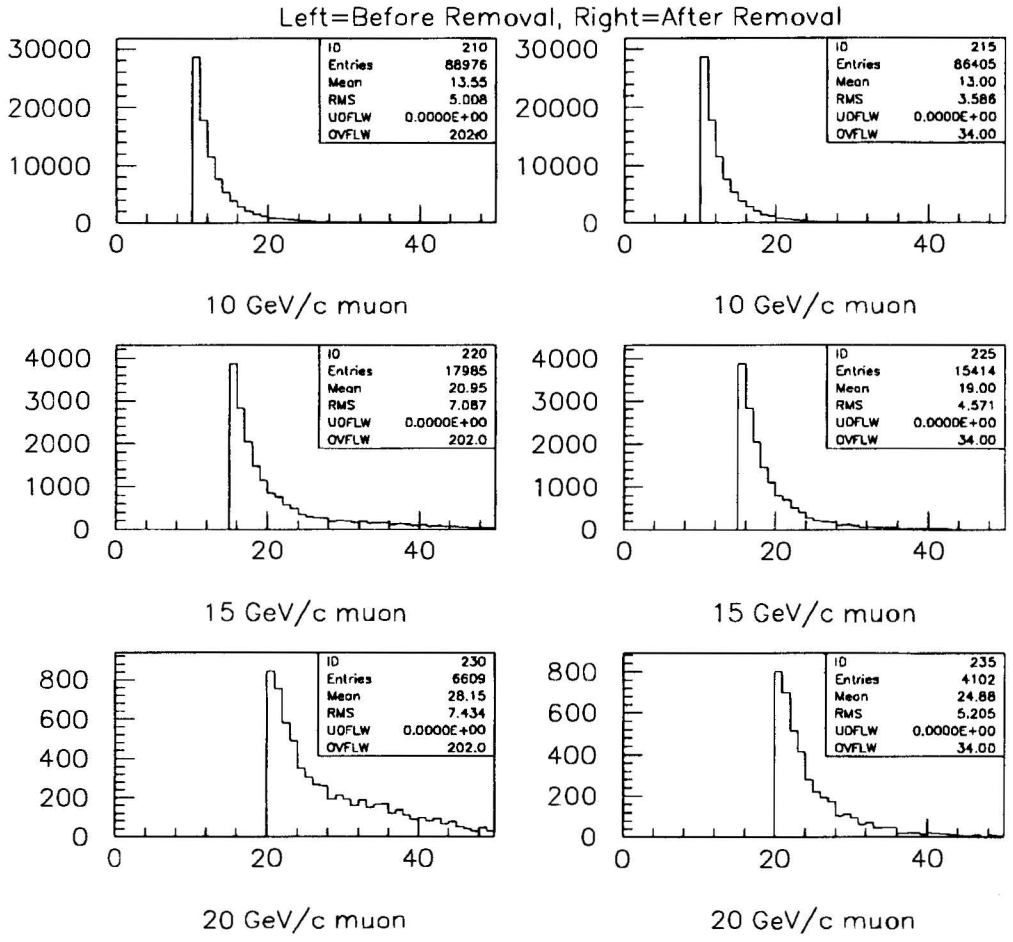

Figure 4.4: Distribution of muon Pt before and after W and Z removal with the other offline cuts applied.

of sources other than bottom, charm and DIF.

- electroweak process

  The efficiency of the W and Z removal procedure has been studied by using Monte Carlo samples [47]. When the same W and Z removal is applied to the inclusive muon sample [48] obtained from 1988-1989, it removes about 1420 W and Z from muons with Pt >12 GeV/c while leaving 146, 43 and 11 events from these sources for Pt bins 12-27, 17-27 and 22-27 GeV/c which are quite close to our Pt bins of $>$ 10, $>$ 15 and $>$ 20 GeV/c. These numbers give the final contribution to be about 10.3, 3.0 and 0.8 % of the amount removed. In the present data set we remove 2571 W and Z from our sample after all the offline cuts applied, about 3.0% of the whole sample. Scaling from the 1988-1989 removal inefficiency, we expect to have 0.3, 0.5 and 0.5 % of the 10, 15 and 20 GeV/c muons respectively in the final samples due to electroweak processes.

- cosmic rays

  Since cosmic rays are not produced by the $p\bar{p}$ collision, the cosmic ray event rate is independent of the instantaneous luminosity. Therefore the fraction of cosmic ray events in a certain sample passing a certain muon trigger is inversely proportional to the instantaneous luminosity during the collisions from which the muon sample is obtained. We know that the relative fraction of cosmic rays to electroweak events in the inclusive muon sample of the 1988-1989 CDF run [49], after a slightly different set of quality cuts, is 0.336/1, 0.093/1 and 0/1 for 12-27, 17-27 and 22-27 GeV/c Pt bins [50]. We can use those numbers

for our Pt ranges, greater than 10, 15 and 20 GeV/c. Considering the fact that the average instantaneous luminosity increased by a factor of 5 in the 1992-1993 run relative to the 1988-1989 run, the relative cosmic ray fractions to the electroweak sources in 1992-1993 data become 1/5 of those of 1988-1989 data, namely 0.067/1, 0.067/1, 0.019/1 and 0.0/1. However, we used a tighter selection on the impact parameter and the event z, which is more efficient in removing cosmic rays than the selection used in the 1988-1989 cuts. Therefore the relative fraction of cosmics to electroweak muons above is a very conservative upper limit. Combining these numbers with the fractions of electroweak sources left in our sample, we estimate the cosmic ray muon fraction to be $\leq$ 0.02, 0.01 and 0.00% for 10, 15 and 20 GeV/c muon samples.

- punch-through

  In case of punch-through an analysis using 1988-1989 data shows that punch-through takes about 46% of the CMU muons with Pt between 12 and 17 GeV/c when similar offline cuts are applied [51]. Considering the fact that requiring the CMP removes 95% of punch-through passing through the CMU, we expect the fraction of punch-through in our sample to be about 5%.

Chapter 5

Calculation of Bottom Cross Section and Efficiencies

We now turn to the discussion of the method for deriving the b quark cross section. We begin, in this chapter with the measurement of experimental efficiencies and acceptances.

5.1 Overview of The Cross Section Calculation

We measure the total cross section for the production of b quarks in the central rapidity region $|y_b| < 1.0$, above a minimum transverse momentum ($=Pt_b^{min}$), that is,

$$\sigma_b = \sigma(p\bar{p} \rightarrow b + X; Pt_b > Pt_b^{min}; |y_b| < 1.0)$$

We measure this cross section at three different Pt_b^{min} of 15, 25 and 35 GeV/c. Since we use a muon to indicate the presence of a bottom quark, we need a prescription to relate the bottom Pt threshold to a muon Pt threshold. The corresponding muon Pt cuts ($=Pt_{mu}^{cut}$) are chosen so that approximately 90% of bottom muons with $Pt >$

Pt^{cut}_{mu} come from b quarks with $Pt > Pt^{min}_{b}$. This leads to Pt^{cut}_{mu} selections of 10, 15 and 20 GeV/c for 15, 25 and 35 GeV/c b quarks, which we have derived using our b quark Monte Carlo sample. In Figure 5.1 we show the Monte Carlo result for the Pt distributions of b quarks which produce 10, 15 and 20 GeV/c muons. In each case the Monte Carlo derived correction factor will allow us to scale from the muon cross section back to the bottom cross section.

Finally, in order to convert a bottom muon rate to a b quark cross section, we need to know acceptances and efficiencies which correct for losses due to geometrical coverage of the detector, kinematical cuts, offline cuts and so on.

The b quark cross section, σ_b, is given by

$$\begin{aligned} &\mathbf{N}_{mu\ passing\ cuts} \cdot \mathbf{f}_b \cdot \mathbf{f}_{(Pt_b > Pt^{min}_b)} \cdot \mathbf{f}_{|y_b|<1} \\ &= \mathbf{2} \cdot L \cdot \sigma_b \cdot \mathbf{B}(b \rightarrow \mu) \cdot \mathbf{A} \cdot \varepsilon \end{aligned} \tag{5.1}$$

where A and ε are global acceptance and efficiency respectively. In equation (5.1), the factor 2 accounts for the fact that we measure an inclusive rate for b quarks, but actually count muons which may come from both b and anti-b quarks.

A represents the experimental acceptance, which has a kinematical and geometrical part

$$\mathbf{A} = \mathbf{A}_{kin} \cdot \mathbf{A}_{geo} \tag{5.2}$$

and ε represents the combined efficiency of all other selections.

$$\begin{aligned} \varepsilon = \varepsilon_{trigger} \cdot \varepsilon_{CMU-CMP} \cdot \varepsilon_{CTC} \cdot \varepsilon_{matching\ \chi^2} \cdot \varepsilon_{|z_{mu}|} \cdot \varepsilon_{PVF} \cdot \\ \varepsilon_{SVX} \cdot \varepsilon_{track\ quality} \cdot \varepsilon_{|D_0|} \cdot \varepsilon_{WZ\ removal} \end{aligned} \tag{5.3}$$

The detailed definitions of all symbols used in equations (5.1),(5.2) and (5.3) are

- $N_{mu\ passing\ cuts}$=the number of muons in the data passing all cuts
- $f_{(Pt_b>Pt_b^{min})}$= fraction of $N_{mu\ passing\ cuts}$ coming from b quark with $Pt_b > Pt_b^{min}$
- f_b= bottom muon fraction in the muon sample after the offline cuts are applied
- $f_{|y_b|<1}$=fraction of b quark ($Pt_b \geq Pt_b^{min}$) with $|y_b| < 1.0$
- L=luminosity
- B($b \rightarrow \mu$)=branching ratio
- A_{kin}=kinematical acceptance for bottom muons with $Pt \geq Pt_{mu}^{cut}$
- A_{geo}=geometrical acceptance for the CMU-CMP muons from bottom decay with $Pt \geq Pt_{mu}^{cut}$
- $\varepsilon_{trigger}$=trigger efficiency
- $\varepsilon_{CMU-CMP}$=muon reconstruction efficiency in the CMU and CMP
- ε_{CTC}= CTC reconstruction efficiency
- $\varepsilon_{matching\ \chi^2}$=efficiency for matching χ^2 cut
- $\varepsilon_{|z_{mu}|}$= efficiency for $|z_{mu}| \leq 30.0$ cm
- ε_{PVF}=efficiency for primary vertex error $\leq 60.0\ \mu m$
- ε_{SVX}=the SVX reconstruction efficiency

- $\varepsilon_{track\ quality}$=track quality cut efficiency

- $\varepsilon_{|D_0|}$=efficiency for |impact parameter| $\leq$ 0.06 cm

- $\varepsilon_{WZ\ removal}$= W and Z removal cut efficiency

Our method for deriving f_b is the heart of this analysis and is therefore discussed separately in Chapter 6. In the remainder of this chapter we derive all other required factors.

5.2 Efficiencies and Acceptances

In this section we consider separately each efficiency and acceptance . A summary of all numbers is given in Table 5.2, along with statistical and systematical uncertainties. Some efficiencies and acceptances are dependent on each other. In that case, a factor coming first is a precondition for a factor coming later.

$\mathbf{f}_{|y_b|<1}$

Figure 5.2 shows the rapidity distributions of b quarks with $Pt > Pt_b^{min}$=15,25 and 35 GeV/c, as modeled by our ISAJET Monte Carlo. The fractions of b quarks with $|y_b| <1.0$ are 0.474$\pm$0.003(stat), 0.542$\pm$0.004(stat) and 0.597$\pm$0.004(stat) for the 3 cases respectively. The efficiency increases with b quark Pt since b quarks with higher Pt are more transverse to the beam line.

$\mathbf{f}_{(Pt_b>Pt_b^{min})}$

As mentioned at the beginning of Section 5.1, we use a convention where roughly 90% of muons with $Pt > Pt_{mu}^{cut}$ come from b quarks with Pt above the corresponding

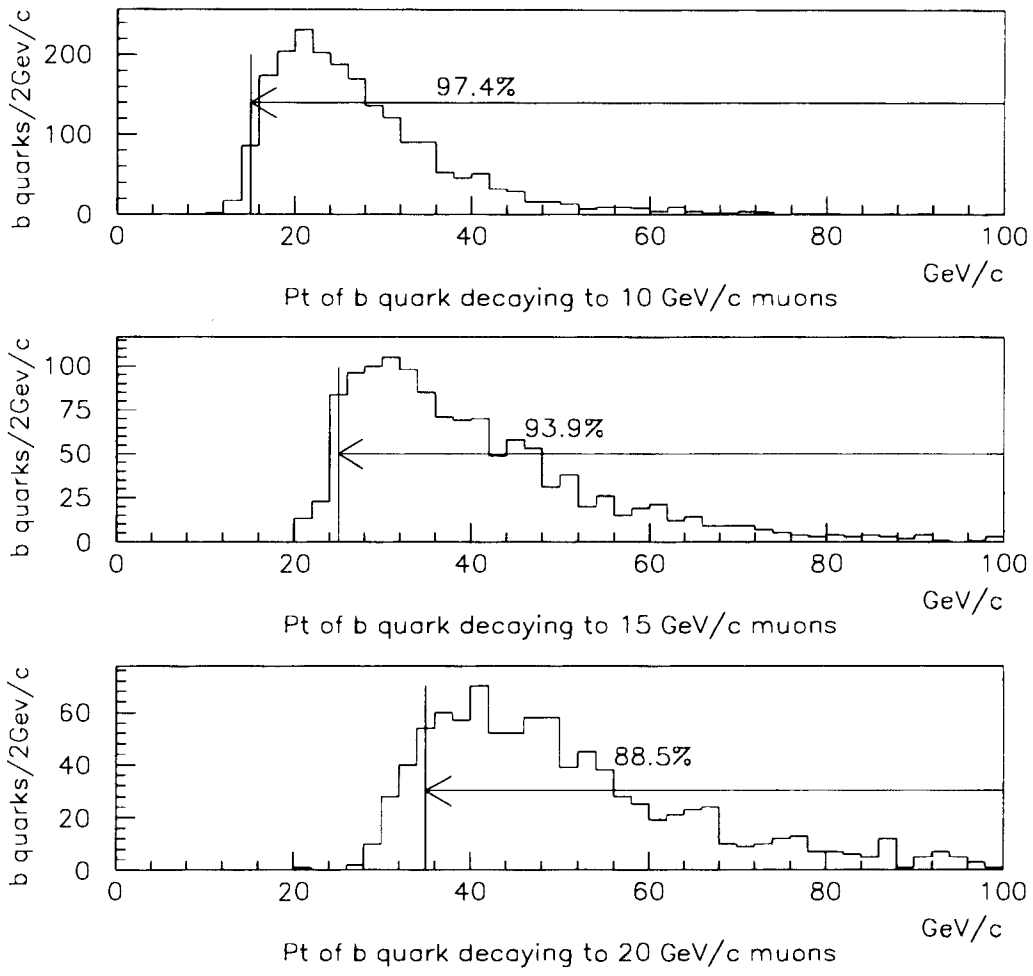

Figure 5.1: The Pt distribution of b quarks producing muons with $Pt \geq$10, 15 and 20 GeV/c. The corresponding minimum b quark Pt's for our measurement are indicated by vertical lines and the fraction of b quarks above this Pt is indicated.

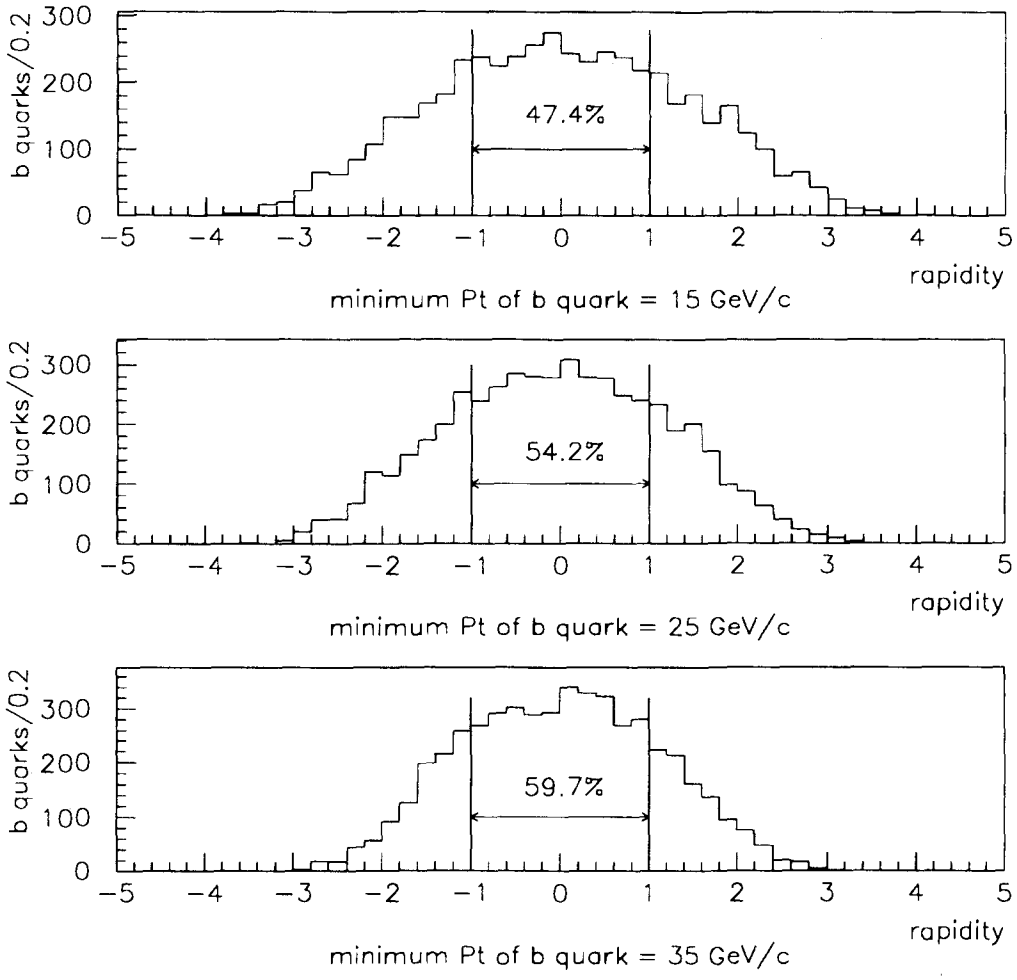

Figure 5.2: The rapidity distribution of b quarks with Pt_b^{min}= 15, 25 and 35 GeV/c.

Pt_b^{min}. The conversion between integral muon rate and integral b quark rate is derived from the ISAJET Monte Carlo. Figure 5.1 shows that the $f_{(Pt_b>Pt_b^{min})}$'s are 0.974, 0.939 and 0.885 with 0.5, 0.7 and 1.0% statistical errors for 10 , 15 and 20 GeV/c muons.

We expect that the main systematic uncertainty in these numbers is contained in the parameterization of the b quark fragmentation function, which describes the fraction of b quark momentum transferred to B mesons during the hadronization process. We use the Peterson parameterization [52], with mean momentum fraction $< z >$=0.83$\pm$0.03, as measured in the e^+e^- experiments [53], to derive our central values for $f_{(Pt_b>Pt_b^{min})}$. Variation of $< z >$ by one standard deviation (0.03) produces changes in $f_{(Pt_b>Pt_b^{min})}$ of order several percent, which we take as systematic uncertainty in $f_{(Pt_b>Pt_b^{min})}$, and which are summarized in Table 5.2.

$\mathbf{B}(b \rightarrow \mu)$

We use the semileptonic decay branching ratio of B hadrons which has been measured at CLEO [54]. Both direct and sequential branching ratios are measured and the values are 0.108$\pm$0.006 for direct lepton decay and 0.0935$\pm$0.0106 for sequential decay.

$\mathbf{A}_{kin}$

A_{kin} is the fraction of bottom muons above the muon Pt cut. Figure 5.3 and 5.4 show the Pt distributions of the direct and sequential bottom muons for three Pt_b^{min} sets as given by the ISAJET Monte Carlo. As seen in the plots, the acceptance of the

Pt cut is very low and the sequential muon acceptance is lower than the direct muon acceptance by a factor of 9, as explained in Section 4.1. The kinematical acceptances for both direct and sequential muons are given in Table 5.2.

It is known that A_{kin} is also sensitive to the model of b quark fragmentation, as discussed above. In this case a 3% variation in $< z >$ in the Monte Carlo shows that the kinematical acceptance changes by about 10% due to the uncertainty of $< z >$.

The experimental efficiency resulting from combining the branching ratio and A_{kin} for both direct and sequential decay is (A_{kin} of direct muon)$\times$(direct muon decay branching ratio) + (A_{kin} of sequential muon)$\times$(sequential muon decay branching ratio), and the values are : $(0.0080-0.0010+0.0009)$, $(0.0090-0.0009+0.0011)$ and $(0.0098-0.0011+0.0011)$ for 10, 15 and 20 GeV/c muons respectively, where the error is the combination of all component errors in quadrature.

$\mathbf{A}_{geo}$

A_{geo} is the fraction of muons passing through the fiducial volume of the CMU and CMP. To study the geometrical acceptance for the CMU-CMP muons, we use a routine called CMUSWM. The CMUSWM is a program simulating trajectory of muons through the CDF detector including multiple scattering. The inputs of CMUSWM are the position and velocity of muons and CMUSWM returns as output the flag of a hit for each muon detector. This program accounts for the beam size, and uses ISAJET to model muon trajectories. We find the geometrical acceptance to be 0.199, 0.252 and 0.262 with 0.6% statistical error for 10, 15 and 20 GeV/c muons. Since the geometrical acceptance depends on the muon Pt spectrum, there is again uncer-

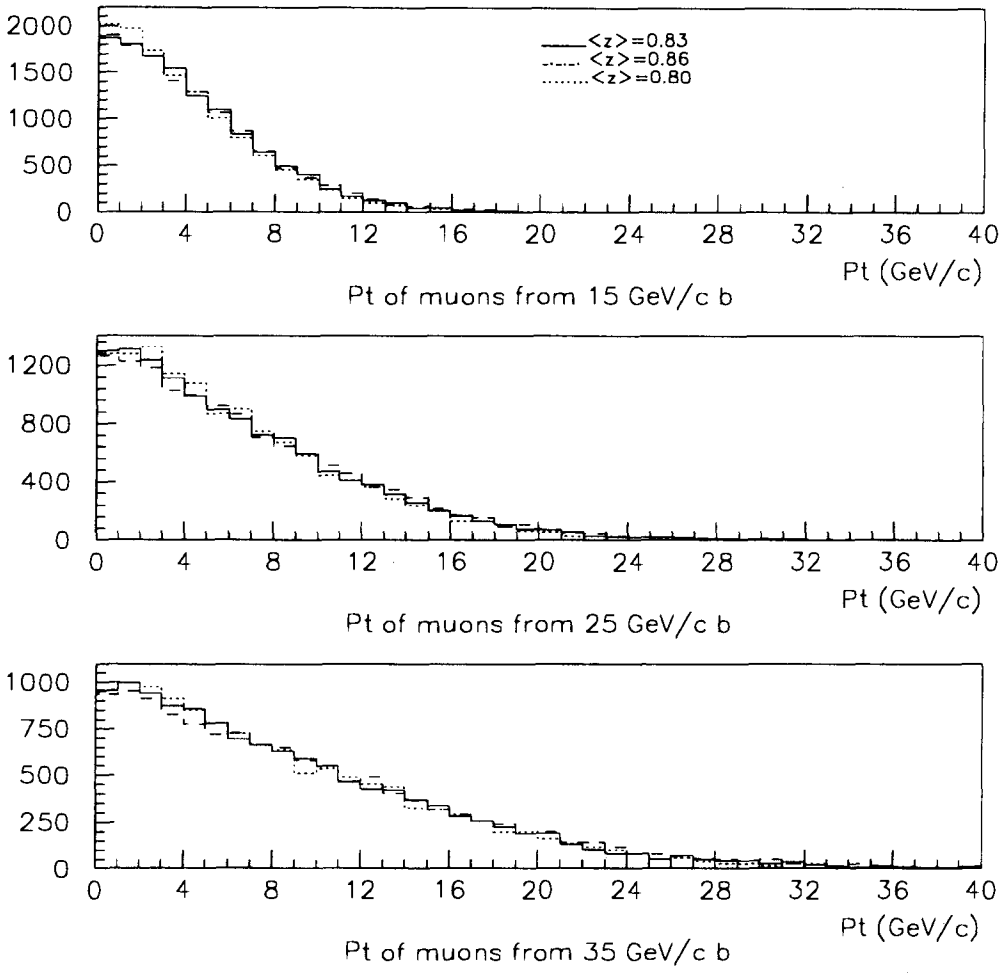

Figure 5.3: The Pt distribution of direct muons from b quark.

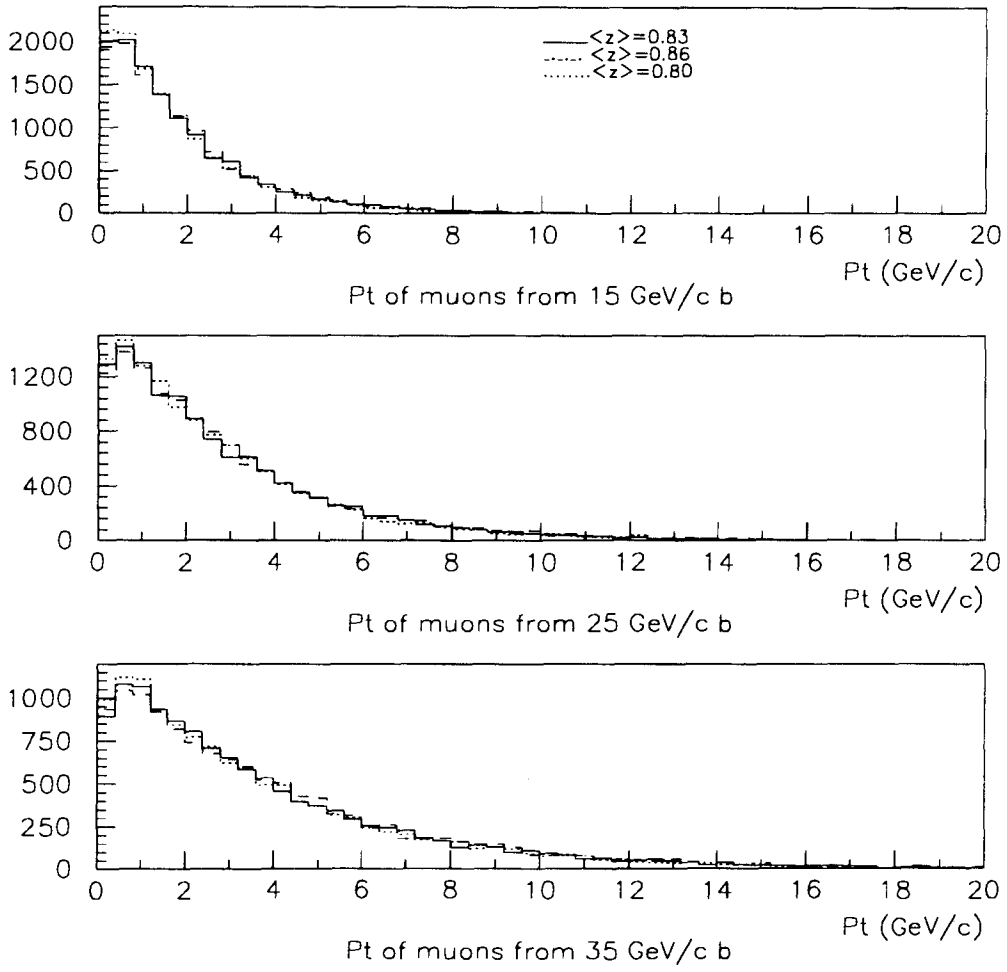

Figure 5.4: The Pt distribution of sequential muons from b quark.

tainty of the acceptance due to the bottom fragmentation. This has been studied by measuring the acceptance again using muon trajectory information in ISAJET after changing the b quark fragmentation parameter by 3%. We do not see any change in the acceptance when using $< z >$=0.86, but when we use $< z >$=0.83, the acceptance decreases by 6.5% and 2.7% for 10 and 20 GEV/c muons and does not change at all for 15 GeV/c muons.

$\varepsilon_{trigger}$

The measurement of trigger efficiency was mentioned in Section 3.2. The trigger efficiencies are functions of track Pt, as seen in Figure 3.1 and 3.2. The total trigger efficiency is the product of Level 1, Level 2 and Level 3 efficiencies and is found at the 10,15 and 20 GeV/c points to be 0.86, 0.89 and 0.89 with an uncertainty of 3.0% [55].

$\varepsilon_{CMU-CMP}$

To measure the CMU-CMP chamber efficiency [56], we use Z samples, where the first muon is required to be reconstructed in the muon chamber and no requirement is made on the second muon except the minimum ionizing cut. We then restrict the 2nd muon to fall into the fiducial volume of the CMU-CMP and count the number of those second muons which actually form a CMU-CMP track. The efficiency is 0.955 ± 0.025.

ε_{CTC}

We use the measured CTC tracking efficiency [57] of kaons and pions from the decays $B \rightarrow J/\psi K$ as our estimate of the CTC tracking efficiency for muons in the B decay environment. The result is 0.989±0.011

$\varepsilon_{matching\ \chi^2}$

To study the matching cut efficiency of b quark muons, $J/\psi \rightarrow \mu^+\mu^-$ samples are used [58]. Since the mass of J/ψ is known to be 3.1 MeV/c^2, we can identify J/ψ muons by reconstructing the invariant mass of two muons. J/ψ muons are selected if the mass of J/ψ is between 3.0 and 3.2 MeV/c^2. Figure 5.5 shows matching χ^2 of those muons. The efficiency of χ^2 cut used in this analysis is 0.987±0.002(stat).

$\varepsilon_{|z_{mu}|}$

The z_{mu} distribution is well fit by a Gaussian distribution, but the variation in beam conditions produces small shifts in the mean and sigma of the distribution from run to run. This run-to-run dependence has been studied for other analyses [59]. Since the muon track z distribution should not be different from the event z distribution, we can use the result of the event z distribution for the muon z distribution. The whole Run Ia data can be separated into 5 groups with each group having a slightly different mean and sigma. Table 5.1 shows 5 partitions with different means and sigmas [60]. Using this table, we can calculate the $|z|$ <30 cm cut efficiencies shown in Table 5.1. The overall efficiency of 0.736±0.003 is found by weighting the efficiency of each group by the fraction of muon data in that interval. The uncertainty results from combining

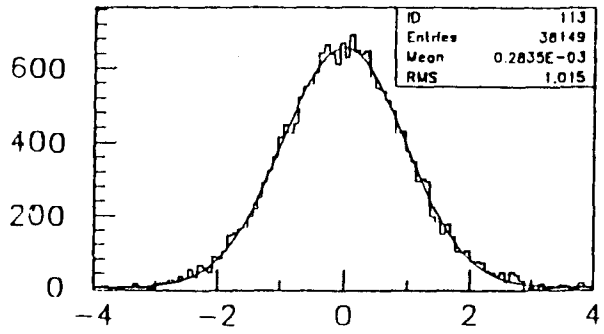

sqrt of X Matching χ^2 CMU, background subtracted

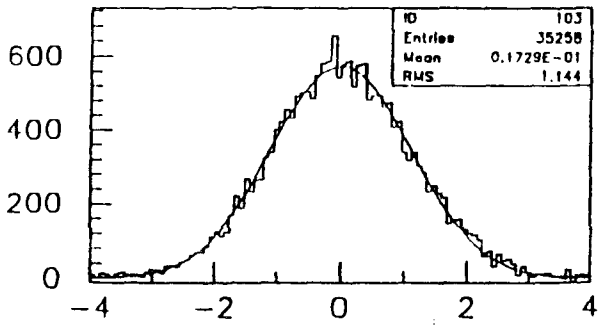

sqrt of Z Matching χ^2 CMU, background subtracted

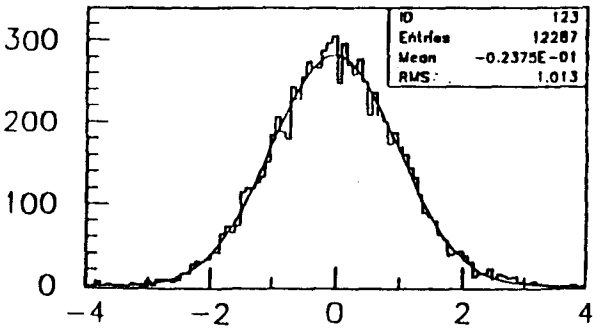

sqrt of X Matching χ^2 CMP, background subtracted

Figure 5.5: The CTC matching χ^2 distribution of J/ψ muons.

the systematics the uncertainty of the mean and sigma of each distribution.

run number	fraction of data (%)	mean (cm)	sigma (cm)	efficiency
40000 - 42000	12.8	-0.67 ± 0.15	27.1 ± 0.18	0.728 ± 0.003
42000 - 44000	32.1	-2.13 ± 0.18	27.2 ± 0.13	0.725 ± 0.003
44000 - 46000	21.7	-0.89 ± 0.12	26.6 ± 0.23	0.736 ± 0.004
46000 - 47200	22.8	-1.89 ± 0.19	27.0 ± 0.51	0.728 ± 0.009
47200 - 48000	10.6	-0.76 ± 0.17	23.5 ± 0.23	0.795 ± 0.005

Table 5.1: Run dependent efficiency for the cut of $\mid z$ event vertex $\mid \leq 30.0$ cm. The uncertainty in the efficiency is the systematics due to the uncertainty of mean and sigma of Gaussian distributions.

ε_{PVF}

Figure 5.6 is the distribution of primary vertex errors in the 10 GeV/c muon sample passing matching χ^2 and z_{mu} cut. Our cut was 60 μm ; therefore almost all muons pass this cut and the efficiency is 0.997 ± 0.000(stat).

ε_{SVX}

ε_{SVX} is the SVX reconstruction efficiency of muons passing the previous cuts. We mentioned the SVX tracking efficiency in Section 2.5 and it is 98% before radiation damage and 97% after the damage. In addition to reconstruction efficiency, this number includes the residual geometrical acceptance due to the fact that the SVX covers $|z|$ <25 cm and we have used $|z_{mu}|$ <30 cm.

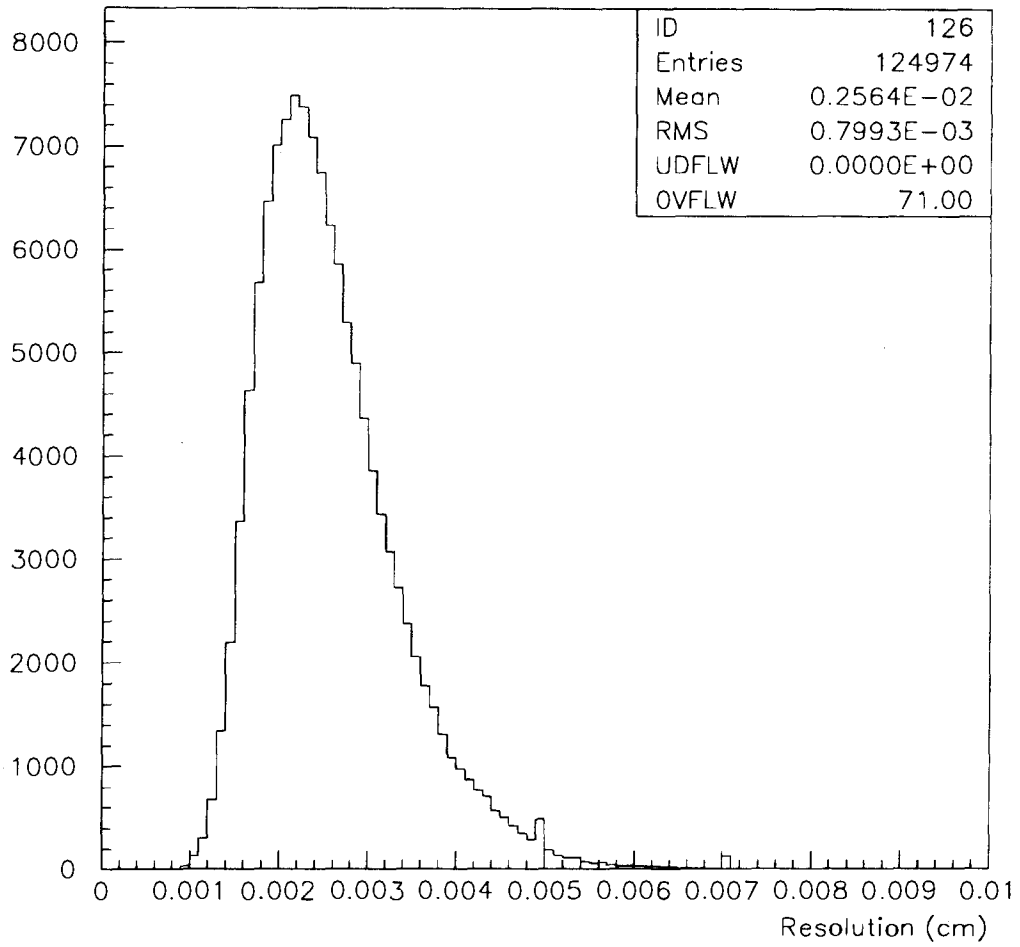

Figure 5.6: Primary vertex finding error of 10 GeV/c muons.

To measure ε_{SVX} we use J/ψ samples in the same way used to measure matching χ^2 cut efficiency. We count the number of muons reconstructed in the SVX among the 5 GeV/c CMU-CMP muons coming from J/ψ and passing matching χ^2 and z_{mu} cuts. We find the efficiency of 0.913±0.006(stat).

$\varepsilon_{track\ quality}$

We measure efficiency of the track quality cut by using the bottom Monte Carlo sample, but we should consider the fact that generally the track quality is worse in data than Monte Carlo. In addition, the track quality gets worse in the later data due to the radiation damage to the SVX. This can be seen in Figure 5.7, where the the track quality cut efficiency for 10 GeV/c muons in our sample is plotted as the function of run number. To get the correction factor between Monte Carlo and data we use jet data and its Monte Carlo. Since the track quality cut efficiency changes as function of the run number, we group the whole Run Ia into 5 partitions, as done in the z_{mu} cut efficiency study and measure the average track quality cut efficiency in each partition using 10 GeV/c tracks. The average efficiency for the whole run is 0.725±0.003(stat). We also measure the efficiency from jet Monte Carlo and we have the efficiency of 0.805±0.005(stat) for 10 GeV/c tracks and conclude that the Monte carlo to data correction factor is 0.725/0.805 = 0.901±0.006(stat). For b decays the Monte Carlo gives track quality cut efficiency of 0.906, 0.891 and 0.872 for 10, 15 and 20 GeV/c bottom muons, with statistical error of 0.4%. The track quality cut efficiency decreases with increasing jet Et because the jets grow denser so that more tracks share the same SVX hits. We multiply the track quality cut efficiency from

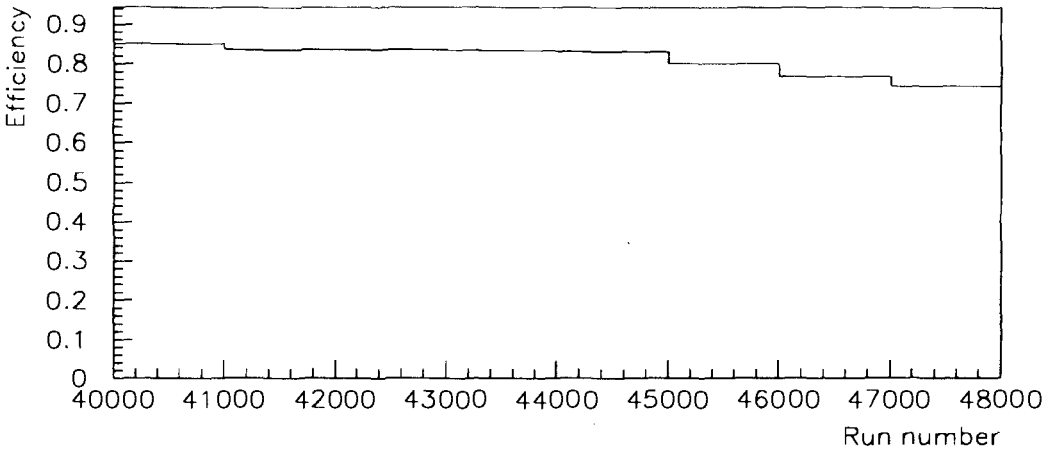

Figure 5.7: The change of track quality cut efficiency obtained by using 10 GeV/c muons.

bottom Monte Calro by the conversion factor above and we find 0.816, 0.803 and 0.786 for 10, 15 and 20 GeV/c muons with 0.8% statistical uncertainty.

$\varepsilon_{|D_0|}$

We again use the bottom Monte Carlo sample to measure this cut efficiency. Figure 4.3 is the absolute impact parameter distribution of 10, 15 and 20 GeV/c bottom muons and the cut efficiency is 0.976, 0.970 and 0.975 with the statistical uncertainty of 0.2%. Since the impact parameter distribution is, to first order, insensitive to the Pt of decay product, we expect the efficiencies to be similar for muon samples with different Pt thresholds, as seen.

$\varepsilon_{WZ\ removal}$

Bottom Monte Carlo sample is used to measure the fraction of bottom muons which are not removed by this cut. The fractions are 1.000, 0.999 and 0.996 for 10, 15 and 20 GeV/c bottom muons and statistical uncertainty is 0.1%

L

Several unavoidable factors lead to a reduction in the size of the useable data set for this analysis. Due to the malfunctioning of muon system during data taking, about 1 pb^{-1} out of all the available 19 pb^{-1} data turned out to be bad runs for all analyses using the CMU-CMP muons. We use 15.2 pb^{-1} out of 18 pb^{-1} due to other data processing problem such as bad condition of magnetic tapes where the data are stored. The uncertainty of the luminosity measurement for the 1992-1993 run is 3.6% [61].

$\mathbf{N}_{mu\ passing\ cuts}$

Total number of muons passing all offline cuts are 84430, 15071 and 4015 for 10,15 and 20 GeV/c muons respectively from Table 4.2.

5.3 Summary of Acceptances and Efficiencies

Table 5.3 is the summary of the study for acceptances and efficiencies needed for the b quark cross section calculation.

By putting all numbers in the Table 5.2 into Equations (5.1), (5.2) and (5.3), we have the following :

$$\sigma_b = \sigma(p\bar{p} \rightarrow b + X; Pt_b > 15GeV/c; |y_b| < 1.0) = \mathbf{1883.9} \times f_b\ nb$$

$$\sigma_b = \sigma(p\bar{p} \rightarrow b + X; Pt_b > 25GeV/c; |y_b| < 1.0) = \mathbf{257.3} \times f_b \; nb \tag{5.4}$$

$$\sigma_b = \sigma(p\bar{p} \rightarrow b + X; Pt_b > 35GeV/c; |y_b| < 1.0) = \mathbf{64.9} \times f_b \; nb$$

Therefore, what remains is to determine the fraction of bottom muons in the inclusive muons passing the offline cuts. A technique for determining this number is the main study of this thesis, and we discuss it in the next chapter.

	$(Pt_b^{min}, Pt_{mu}^{cut})$			stat. error(%)			sys. error(%)		
	(15,10)	(25,15)	(35,20)	(15,10)	(25,15)	(35,20)	(15,10)	(25,15)	(35,20)
$f_{\|y_b\|<1}$	0.474	0.542	0.597	0.7					
$f_{(Pt_b>Pt_b^{min})}$	0.974	0.939	0.885	0.5	0.7	1.0	−0.3+0.4	−0.6+0.9	−2.8+1.5
$B(b \to \mu)$	0.108						5.5		
$B(b \to c \to \mu)$	0.0935						11.3		
$A_{kin}(b \to \mu)$	0.0697	0.0777	0.0846	0.1			−11.8+9.5	−8.2+10.9	−9.2+9.8
$A_{kin}(b \to c \to \mu)$	0.0054	0.0065	0.0065	0.0			−6.5+23.5	−16.3+3.9	−19.3+12.7
A_{geo}	0.199	0.252	0.262	0.6			−6.5+0.0	0.0	−2.7+0.0
$\epsilon_{trigger}$	0.86	0.89	0.89				3.0		
$\epsilon_{CMU-CMP}$	0.955						2.6		
ϵ_{CTC}	0.989						1.1		
$\epsilon_{matching\ \chi^2}$	0.987			0.2					
$\epsilon_{\|z_{mu}\|}$	0.736						0.4		
ϵ_{PVF}	0.997			0.0					
ϵ_{SVX}	0.913			0.7					
$\epsilon_{track\ quality}$	0.816	0.803	0.786	0.8					
$\epsilon_{\|D_0\|}$	0.976	0.970	0.975	0.2					
$\epsilon_{WZ\ removal}$	1.000	0.999	0.996	0.1					
$L(nb^{-1})$	15192						3.5		
$N_{mu\ passing\ cuts}$	84430	15071	4015	0.3	0.8	1.6			

Table 5.2: A summary of efficiencies and acceptances.

Chapter 6

Measurement of Bottom Fraction

We measure the bottom muon fraction in the muon data passing the offline cuts by analysing the shape of muon impact parameter distributions, and measuring the contribution from the $b \rightarrow \mu X$ component. In this chapter we discuss the method, the models employed, and checks on the technique. Then we present the results with their statistical and systematical errors.

6.1 Impact Parameter Distribution of Muons

We discussed the definition of impact parameter in Section 1.6 and based on Equation (1.2), we can formulate the impact parameter distribution of a decay product. It is written as [62]

$$\frac{dN}{d\Delta} = \frac{1}{2}\int \sin(2\tan^{-1}\frac{y}{z})\frac{2}{1+(\frac{y}{z})^2}\frac{1}{cz\tau}e^{-z}dz \qquad (6.1)$$

where Δ is the impact parameter, $z=t/\tau$ and $y=\Delta/c\tau$. The decay time in the lab frame is denoted by t and τ is the mean lifetime. Equation 6.1 cannot be expressed as the form of an explicit function. We can use a numerical method to get a distribution,

but the measured impact parameter distribution includes other effects such as multiple scattering, detector resolution and primary vertex finding error, which require us to rely on a Monte Carlo simulation instead. The impact parameter is measured by the SVX, and since the resolution of the SVX is small compared to $c\tau_B$, the SVX is well suited to the technique of measuring the bottom fraction by muon track impact parameter. We first discuss characteristics of the impact parameter distributions for muons from the different sources that we expect in our sample.

Bottom and Charm Muons

The expected distribution of impact parameters for bottom and charm muons will be derived from Monte Carlo simulation. Figure 6.1 is the impact parameter distribution of bottom and charm muons with Pt >10 GeV/c. As we expect from the fact that the average lifetime of bottom mesons is larger than that of charm mesons, the impact parameter distribution of bottom muons is much broader than for charm muons.

In case of the bottom muon distribution, Figure 6.1 also shows the distribution before adding resolution smearing in the detector simulation. After resolution smearing is added, the width of the distribution as estimated from the RMS increases by 10 μm.

In general the resolution simulated in the Monte Carlo is underestimated compared to the data. Figure 6.2 shows the impact parameter distribution of 10 GeV/c tracks in jet data and jet Monte Carlo. As mentioned in Section 3.4, the jet sample consists of mostly no-lifetime tracks, and the width of the track impact parameter distribution in jets is a measure of a resolution broadening effect. The distribution of jet data

is a little broader than jet Monte Carlo as predicted. We expect the same in the impact parameter distributions of bottom and charm Monte Carlo, but we will show later that this difference does not affect the fitting result for the measurement of the bottom muon fraction.

Decay-In-Flight Muons

As discussed in Section 4.1, a significant component of the muon signal after all selections is from decay-in-flight (DIF) of pions and kaons. The probability that a relativistic particle of lifetime τ will decay before a time t in the lab frame is $P(t)$=1-$e^{\frac{-t}{\gamma\tau}}$. It can be put in a different form of

$$P(p_t)=1\text{-}\exp(-\frac{RM}{Pt\tau}) \tag{6.2}$$

where Pt and M are transverse momentum and mass of the decaying particle, and R is arc-length projected in the x-y plane [63]. Using the CMU radius R=3.7 m in Equation (6.2) and the Pt distribution of pions and kaons in ISAJET, we can calculate the fraction of pions and kaons decaying before reaching the CMU, and find this fraction for pions and kaons with Pt >10 GeV/c is 0.0046 and 0.0331. Since the lifetimes are very long, a significant fraction of pions and kaons will decay inside the SVX, CTC and calorimeter, unlike the bottom and charm mesons, which, because of their relatively short lifetimes, decay well before reaching even the beam pipe.

When pions and kaons decay inside the detector component, the trajectory has a measurable kink, and therefore many DIF muons cannot be reconstructed as "good" muon tracks, and as a result, a significant fraction of DIF muons fails to pass the matching χ^2 and track quality cuts.

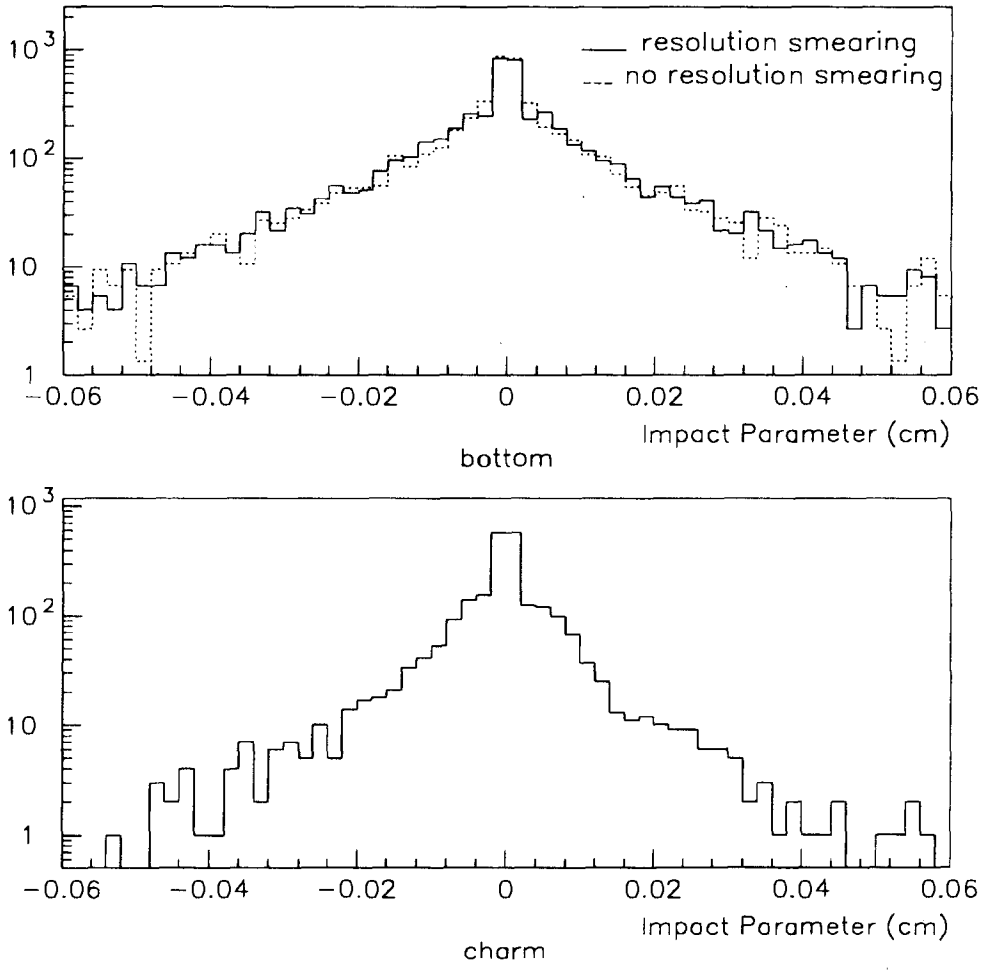

Figure 6.1: Impact parameter distribution of 10 GeV/c bottom and charm muons. Dotted line in the bottom plot is the distribution before resolution effect is introduced.

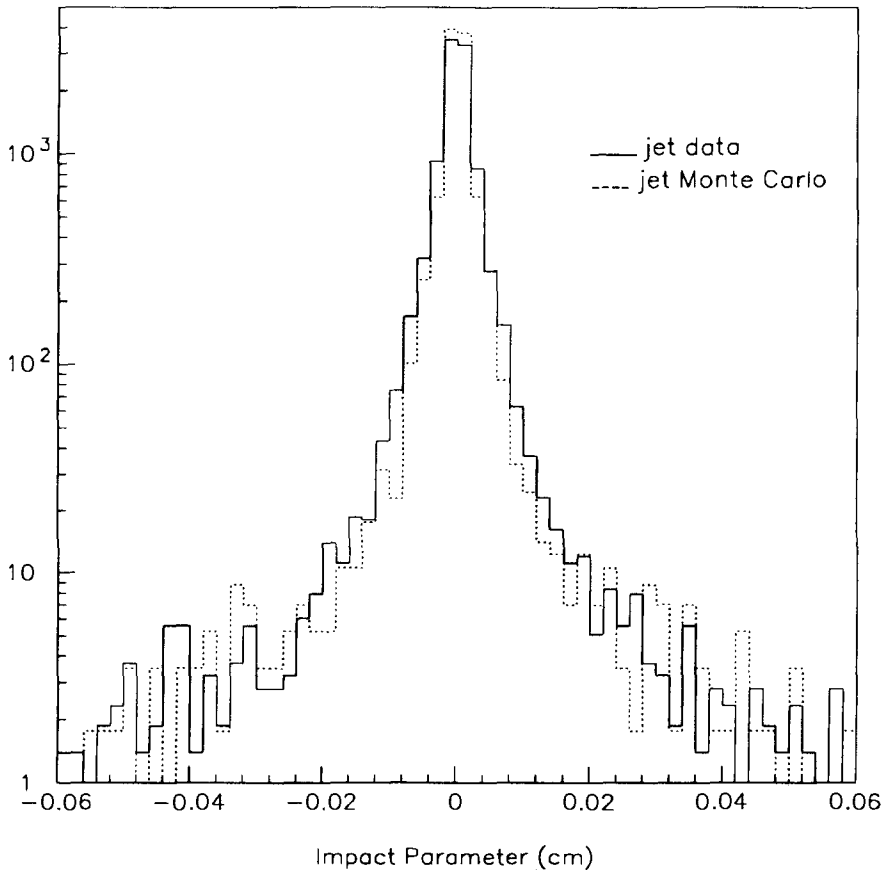

Figure 6.2: Comparison of impact parameter distributions of 10 GeV/c tracks in jet data and jet Monte Carlo.

Since later we will use the ratio of pions to kaons in our sample for a systematic study of bottom fraction, we calculate acceptances and efficiencies needed to estimate the ratio. To study the acceptance of DIF muons, we used Monte Carlo tools. We generate a pion and kaon by ISAJET at a given Pt and then force the pion (kaon) to decay into a muon by a routine called GET_PATH_LENGTH [64]. This routine takes into account dE/dx of the meson in the calorimeter prior to decay and produces the probability of decay and decay path-length. After that, the same standard CDF detector simulation is performed.

We used 1,000 10 GeV/c pions and 700 10 GeV/c kaons, each decaying to muons before reaching the CMU and found 154 and 91 10 GeV/c CMU-CMP muons reconstructed with $|z_{mu}| < 30$ cm for pions and kaons respectively, which gives the acceptances of 0.154 ± 0.011(stat) and 0.130 ± 0.013(stat).

We calculate the ratio of offline cut efficiency for kaon and pion muons from the Monte Carlo. There are 4 cuts which affect pion and kaon differently, which are matching χ^2, D_0 , track quality cuts and SVX reconstruction. Since kaon decays have larger kinks, the quality of track reconstruction is worse than for pions and the impact parameter is larger. The efficiency of those 4 cuts is 0.597 ± 0.007(stat) and 0.319 ± 0.009(stat) for 10 GeV/c CMU-CMP pion and kaon muons. Table 6.1 is the summary of the information needed to estimate the K/π ratio. The K/π ratio of the DIF muons in our muon sample is estimated to be 0.58 ± 0.10.

To estimate the fraction of DIF muons decaying before reaching the third SVX layer from the interaction point we plotted the distribution of decay radii of pions and kaons producing 10 GeV/c CMU-CMP muons passing the matching χ^2 cut, and

production rate	0.28±0.03
fraction decaying before reaching the CMU	0.0331/0.0046=7.20
branching ratio	0.635/0.999=0.64
acceptance of CMU-CMP muons with Pt>10 GeV/c	0.130/0.154=0.84±0.11(stat)
offline cuts efficiency	0.319/0.597=0.53±0.02(stat)
final ratio in the sample	0.58±0.10

Table 6.1: The ratio of K/π of DIF muons for muons with Pt >10 GeV/c.

as shown in Figure 6.3, only about 3% of pions and kaons decay before reaching the third SVX layer which is at r=6 cm. Therefore only 3% of 10 GeV/c DIF muons can be reconstructed in the SVX and have their impact parameters measured, because the SVX reconstruction requires a track to have at least 2 hits. For the other 97% 10 GeV/c DIF muons, the reconstructed tracks in the SVX are tracks of the decaying not the decay product. Therefore the DIF background will have the impact parameter distribution of no-lifetime tracks, but broadened from the expected resolution by the presence of kinks.

Figure 6.4 is the impact parameter distribution of 10 GeV/c muons from kaon and pion Monte Carlo. Since DIF muons behave like no-lifetime tracks, we can use tracks in a sample of generic jets to model the impact parameter distribution of DIF muons. The distributions are compared to 10 GeV/c tracks in jet data and the impact parameter distribution of pion muons agrees well with the distribution of jet data, but the distribution of muons from kaons is slightly broader than from pions and jets

since the kink angle in kaon decay is larger. We will show later that the difference in broadness does not affect f_b. We will therefore use as our model for DIF the impact parameter distribution for a sample of tracks with $Pt > Pt^{cut}_{mu}$ from JET_20 data.

Other Sources

The other sources are muons from electroweak processes, that is, W,Z and Drell-Yan, cosmic rays and punch-through's. We estimated fractions of the above sources in Section 4.3 and find that they make a very small contribution. And even in this small contribution, muons from electroweak process are no-lifetime tracks and non-interacting punch-through's are long-lifetime hadrons produced at primary vertex, all of which are reconstructed to have zero-lifetime. In case of interacting punch-through, hadrons interact at the calorimeter, which means fake muons are matched to tracks reconstructed as zero-lifetime tracks in the CTC and SVX. Therefore the impact parameter distribution of other sources can also be modeled as no-lifetime tracks.

6.2 Impact Parameter Fitting Method

As we mentioned in the previous section, we can classify muon sources after our selection into three categories, which are bottom muons, charm muons and "background". The "background" is mainly DIF muons and can be handled as a single no-lifetime component as far as the impact parameter distribution is concerned.

Our goal is to measure the bottom muon fraction in the muon data by fitting the three distinctive impact parameter distributions of these components to that of muon data. We use a binned maximum likelihood method [65] for fitting. We let bottom and charm fractions be unknown variables; then the expected population in each bin

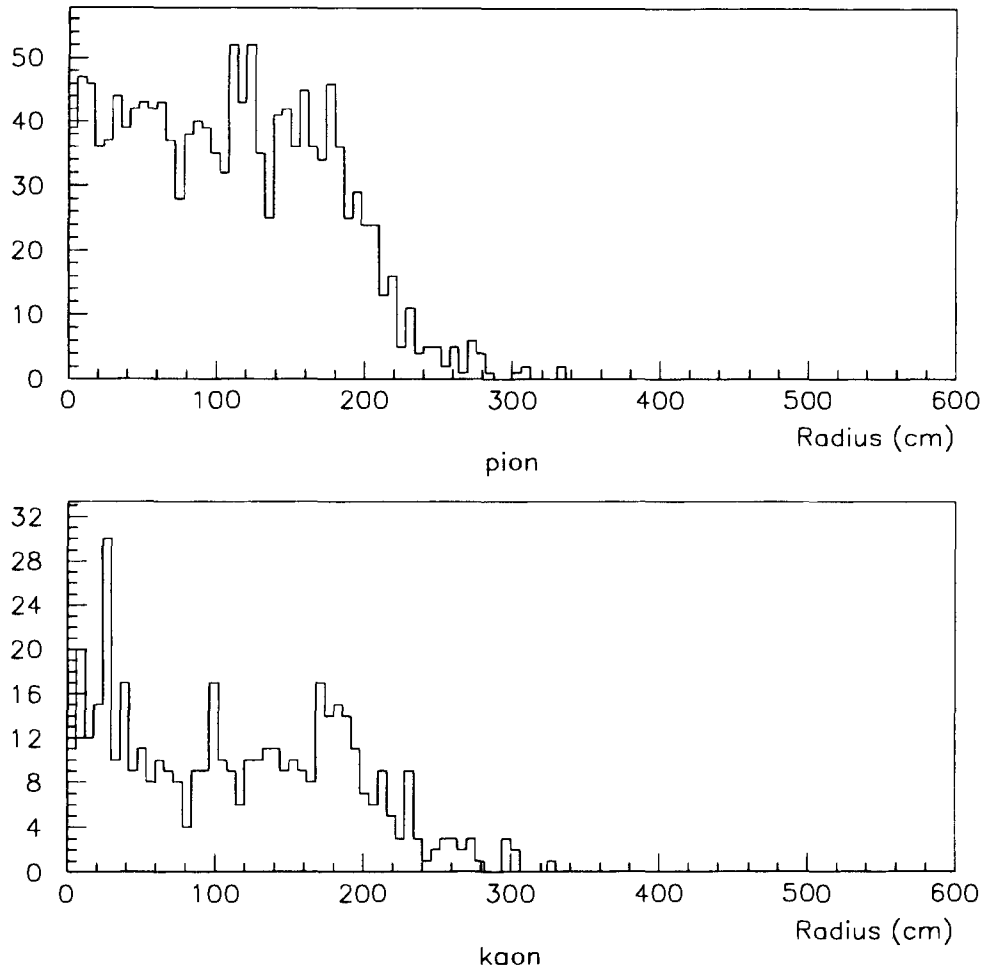

Figure 6.3: Decay length in x-y plane of 10 GeV/c pions and kaons which decay to 10 GeV/c CMU-CMP muons passing matching χ^2 cuts.

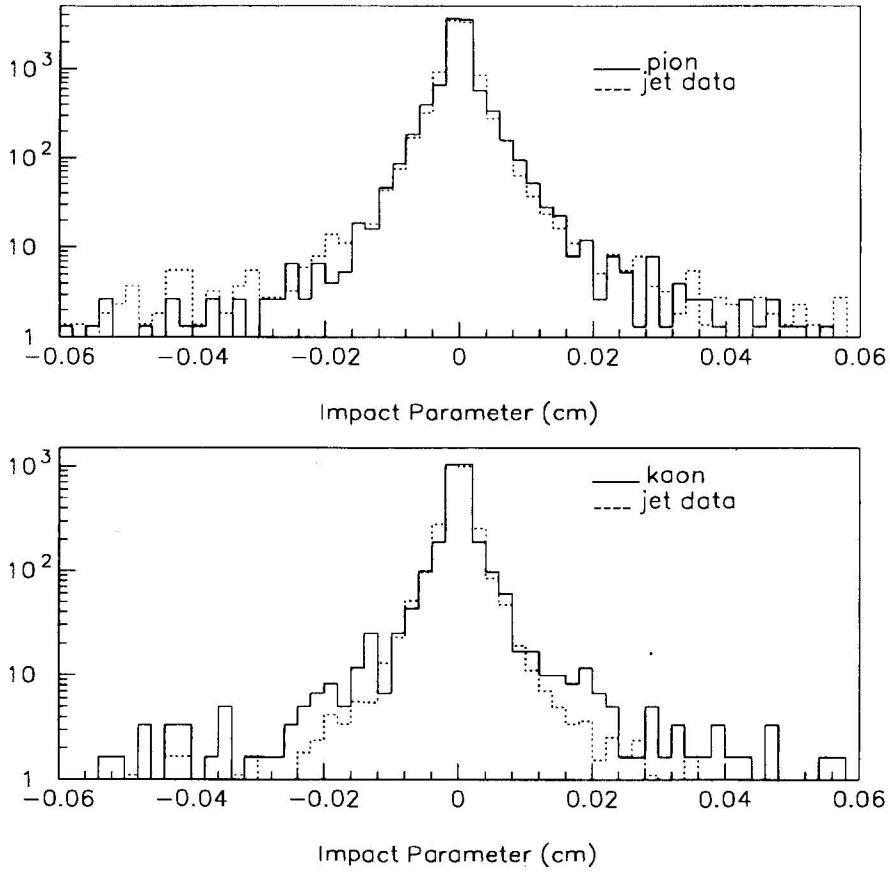

Figure 6.4: Impact parameter distribution of 10 GeV/c DIF muons and comparison of impact parameter distributions between DIF muons and 10 GeV/c tracks in jet data.

of the impact parameter histogram is

$$f_b A_i + f_c B_i + (1 - f_b - f_c) C_i \equiv l$$

where i represents the i^{th} bin, f_b and f_c are bottom and charm fractions respectively, and A, B and C are normalized bottom, charm and DIF muon impact parameter distributions derived from our models. For each muon event, l is given as a function of f_b and f_c and we define the likelihood ($=L$) as the product of all l's for all muon data, which is

$$L = \prod_{j=1}^{N} l_j(f_b, f_c)$$

where N is the total number of muons in the data. The variable f_b and f_c are found by maximizing L, which is performed by the program called MINUIT [66].

We model the impact parameter distribution of muons coming from b quarks and c quarks by using Monte Carlo samples. We model the impact parameter distribution of the "background" using tracks in the generic jet data samples, which is JET_20 data. We apply the same offline cuts to the tracks in the jet data, except for muon specific cuts like matching χ^2 cut.

6.3 Test of Fitting Technique

Before we measure the bottom muon fraction in the muon data, we test the reliability of the proposed procedure in full simulation. For that purpose, we take the simulated bottom, charm muons and the JET_20 background sample, and mix them with known rates to make a test sample. We use 10 GeV/c muons for bottom and charm and 10 GeV/c tracks from JET_20 jets for background, where all those

tracks pass the offline cuts. Table 6.2 shows the result of fitting 3 mixed samples with different fractions of each component. The fitting result of f_b agrees well with the real f_b in the mixed sample for all 3 mixed samples. We repeat the same thing for 15 and 20 GeV/c tracks. Table 6.3 and 6.4 show that the fitting program also gives the expected bottom fractions for the cases of higher Pt's.

number of total events in the mixed sample	number of b muons in the mixed sample	number of c muons in the mixed sample	number of background tracks in the mixed sample	fitted b fraction
3000	1000(0.333)	1000	1000	0.333±0.039
2000	1000(0.500)	500	500	0.500±0.046
2500	500(0.200)	1000	1000	0.200±0.031

Table 6.2: Test of fitter for 10 GeV/c tracks. The values in the parenthesis are real b fractions.

6.4 Bottom Fraction

We now measure the bottom fraction in our samples of 10,15 and 20 GeV/c muons. The impact parameter distribution of the 10 GeV/c muon data is shown in Figure 6.5(a). Figure 6.5(b), 6.5(c) and 6.5(d) are impact parameter distributions for 10 GeV/c bottom muons, charm muons and background tracks respectively. We notice that the slope in muon data is between that of bottom muons and charm muons.

We now fit the data distribution of Figure 6.5(a) to the bottom muons distributions plus charm muons plus backgrounds, that is, 6.5(b) plus 6.5(c) plus 6.5(d)

number of total events in the mixed sample	number of b muons in the mixed sample	number of c muons in the mixed sample	number of background tracks in the mixed sample	fitted b fraction
2000	500(0.250)	1000	500	0.250±0.044
4000	1500(0.375)	2000	500	0.375±0.036
2500	1000(0.400)	500	1000	0.400±0.041

Table 6.3: Test of fitter for 15 GeV/c tracks. The values in the parenthesis are real b fractions.

The result is

$$f_b(10\text{GeV}) = 0.310\pm0.008$$

The result of this fit is shown graphically in Figures 6.6 and 6.7. Figure 6.6 shows that the bottom fraction is driven by the tail region of the distribution and the sum of 3 components agrees well with the data except in the tail region.

We can measure bottom fractions of 15 and 20 GeV muons in the same way. The result is

$$f_b(15\text{GeV}) = 0.383\pm0.020$$

$$f_b(20\text{GeV}) = 0.270\pm0.035$$

Figure 6.7 and 6.8 are plots for 15 GeV muons and Figure 6.9 and 6.10 are for 20 GeV muons. In cases of both 15 and 20 GeV/c, it is seen more clearly that bottom muons are the strong contribution to the tail region of the data distribution. For the

number of total events in the mixed sample	number of b muons in the mixed sample	number of c muons in the mixed sample	number of background tracks in the mixed sample	fitted b fraction
2500	500(0.200)	1500	500	0.200±0.034
3500	1000(0.286)	1500	1000	0.286±0.034
3000	2000(0.667)	500	500	0.667±0.045

Table 6.4: Test of fitter for 20 GeV/c tracks. The values in the parenthesis are real b fractions.

15 and 20 GeV/c cases, we see that the fit is very good, even out to extreme tail, and this convinces us that the poor fit on the tail in the 10 GeV/c case is the result of statistical fluctuations in our model distributions, which are poorly populated for impact parameter greater than 0.04 cm. The uncertainty associated with our model statistics is discussed in Section 6.6.

6.5 Additional Test of Fitting Without W and Z Removal

After we measure the bottom fractions, we can test the fitting in another way. The bottom fractions we have are for the muon data after offline cuts including W and Z removal. Since we know how many W's and Z's are removed, we can predict f_b in the muon data before removing W and Z and refit the data without removing W and Z to see if the prediction agrees with the fitting. Table 6.5 shows that the measurement of f_b agrees well with the prediction except for the Pt=20 GeV/c case, where the W/Z fraction is large, and the statistical uncertainty on the heavy flavor

component is large compared to the Pt=10 and 15 GeV/c cases. Nevertheless the agreement is still within 2σ. This cross-check also shows that our assumption that all "backgrounds" can be represented by no-lifetime tracks is reasonable.

muon Pt(GeV/c)	measured f_b after removal	predicted f_b before removal	measured f_b before removal
10	0.310±0.008	0.301±0.008	0.293±0.008
15	0.383±0.020	0.328±0.017	0.293±0.017
20	0.270±0.035	0.168±0.022	0.096±0.029

Table 6.5: Test of the fitting with and without W and Z removal.

6.6 Treatment of Statistical Uncertainty

The fitting program returns fitting uncertainties, which are 2.6%, 5.2% and 13.0% for 10,15 and 20 GeV/c bottom muon fractions. Since the fitting program regards the impact parameter distributions of 3 components of models as perfect models, these fitting uncertainties include statistical uncertainty of only the muon data. To study the uncertainty due to statistics of the 3 component models, we run many trials where we fluctuate the contents of each bin in the impact parameter distribution for each component according to a Poisson distribution with mean equal to the bin contents, and then refit.

As the first step, we study how f_b changes due to statistical fluctuation in the impact parameter distribution of bottom muons only. We study 10 GeV/c muons first and repeat same thing for 15 and 20 GeV/c muons. We used 3 components of

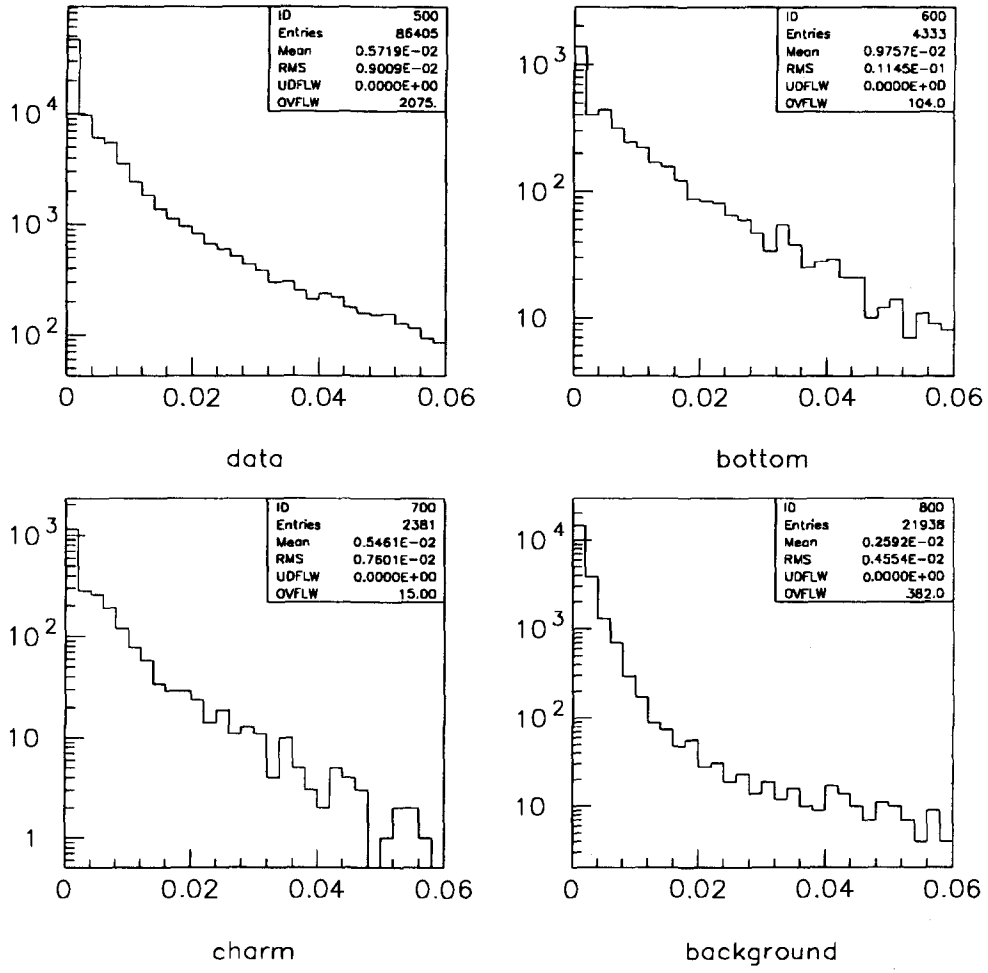

Figure 6.5: Impact parameter distribution of 10 GeV/c data muons along with 3 components of models.

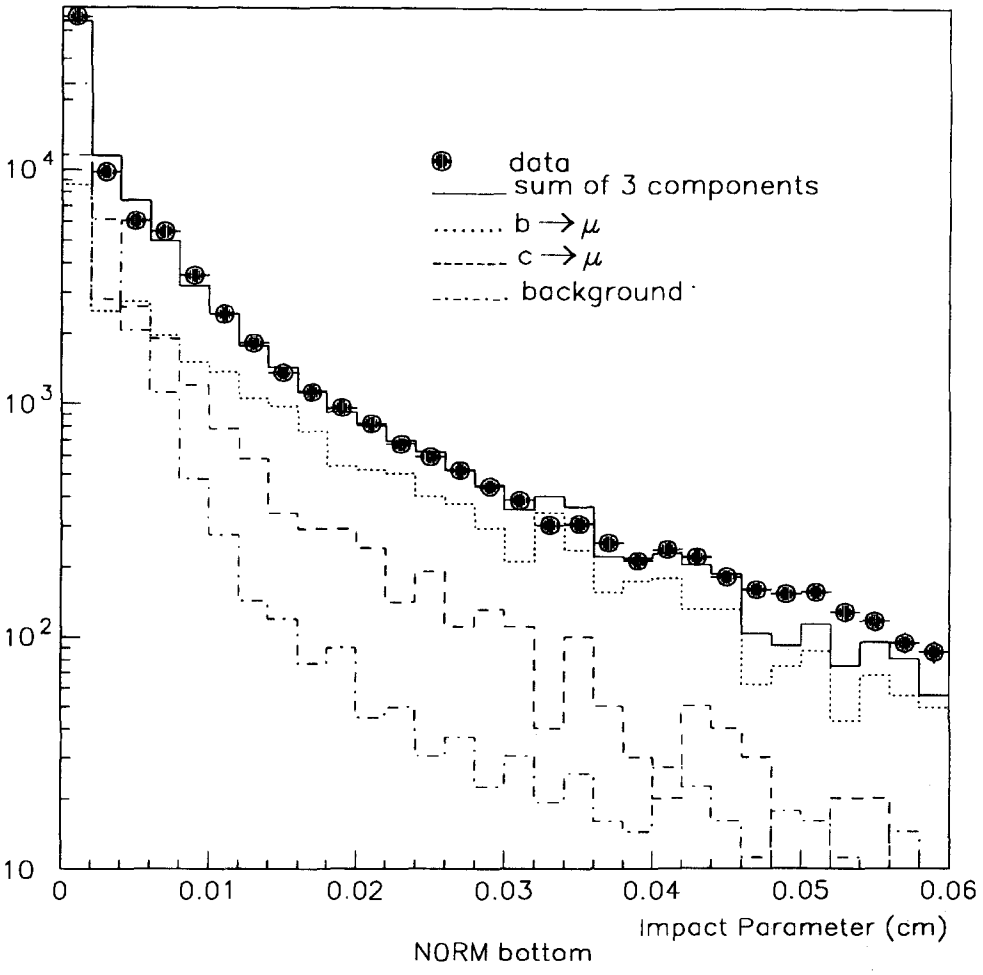

Figure 6.6: 10 GeV/c muon impact parameter with 3 components of models normalized to their fractions in muon data and sum of the 3 components.

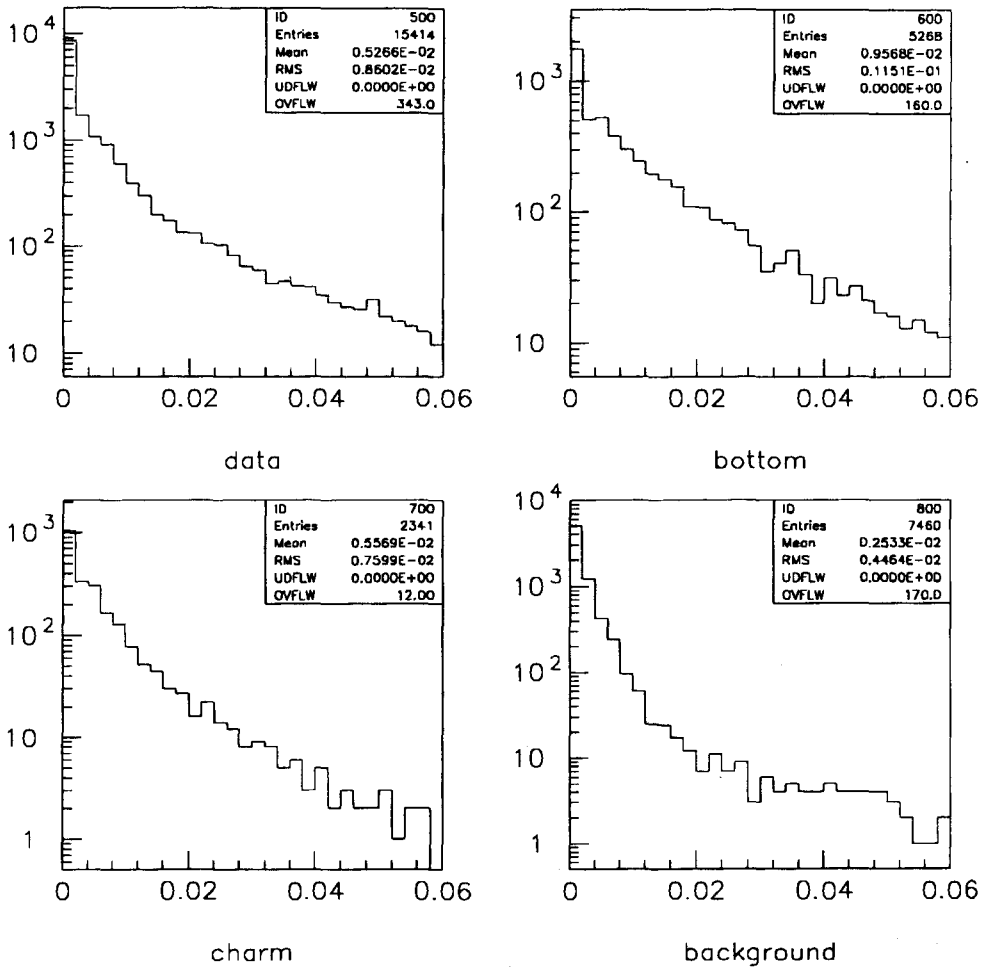

Figure 6.7: Impact parameter distribution of 15 GeV/c data muons along with 3 components of models.

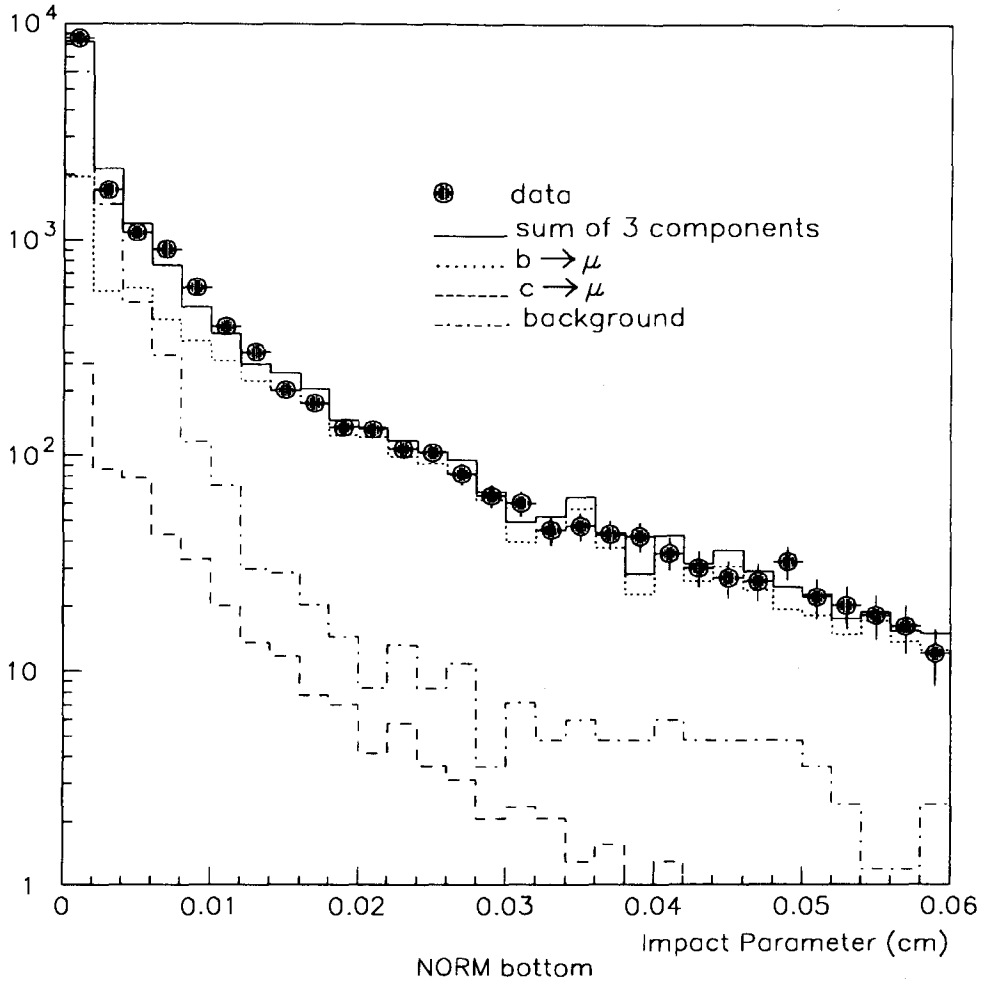

Figure 6.8: 15 GeV/c muon impact parameter with 3 components of models normalized to their fractions in muon data and sum of the 3 components.

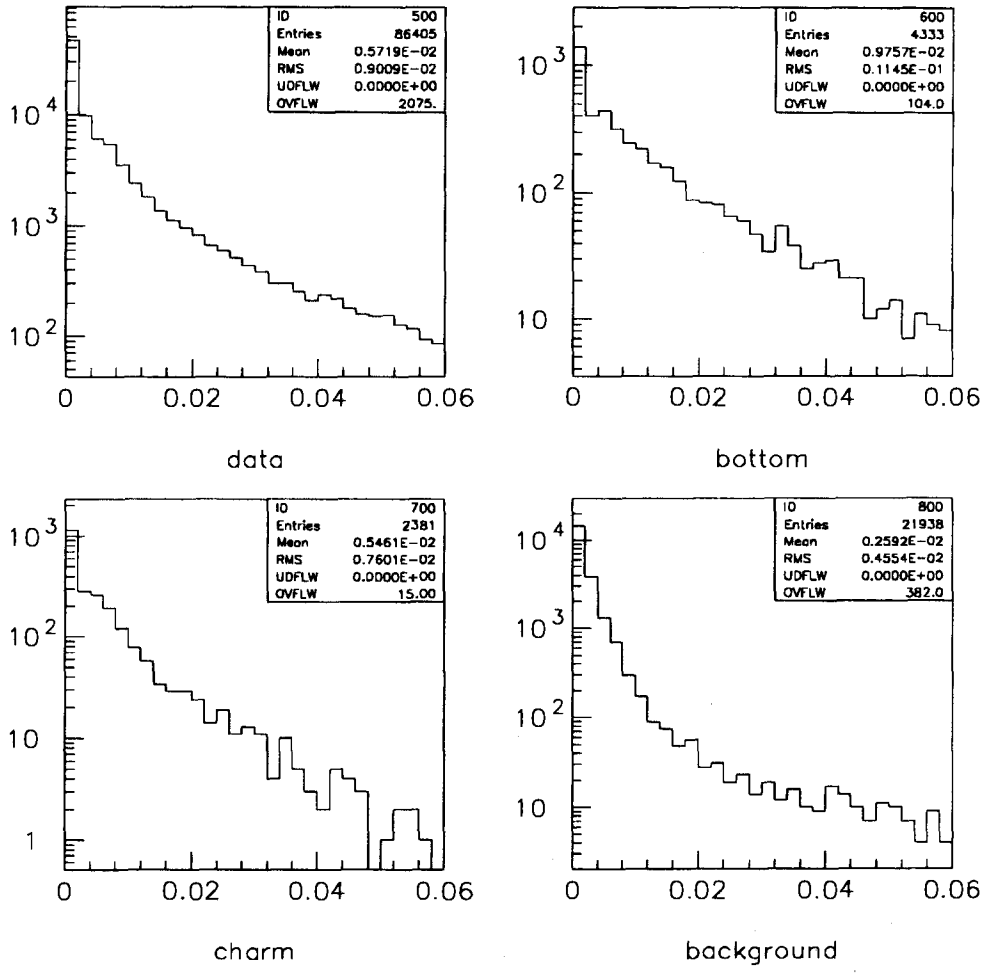

Figure 6.9: Impact parameter distribution of 20 GeV/c data muons along with 3 components of models.

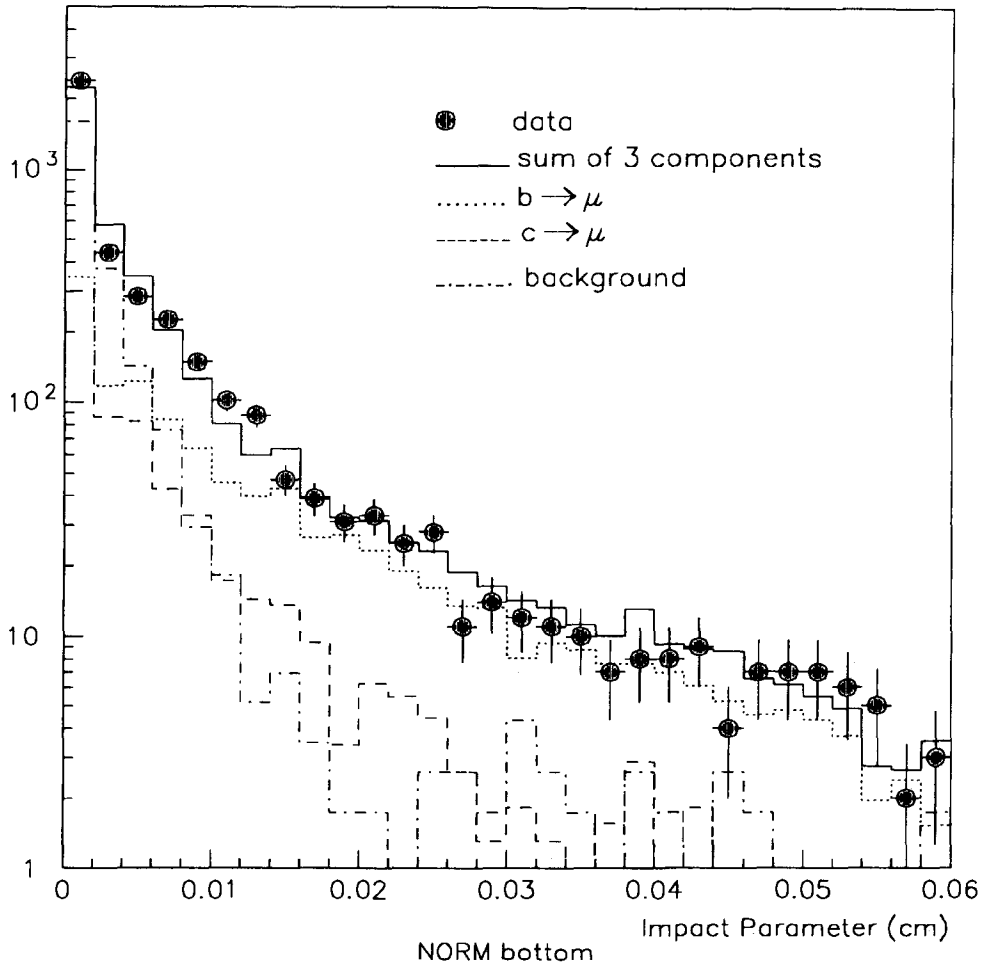

Figure 6.10: 20 GeV/c muon impact parameter with 3 components of models normalized to their fractions in muon data and sum of the 3 components.

models shown by Figure 6.5(b), (c) and (d) to measure f_b of 10 GeV muons. We then fluctuate the contents of each bin of Figure 6.5(b), which is bottom muons. We make 500 impact parameter distributions from Figure 6.5(b) in that way and measure f_b's 500 times without changing Figure 6.5(a), (c) and (d). Figure 6.11 is the distribution of such 500 f_b's fitted with a Gaussian, and the sigma of the Gaussian is 0.016.

To find the statistical uncertainty due to all 3 components together, we fluctuate 3 components together and measure f_b. Figure 6.12(a) is the f_b distribution from the statistical fluctuation of all 3 components for 10 GeV/c muons and the sigma is 0.024. We can do the same thing for 15 and 20 GeV/c muons and we find sigmas of 0.026 and 0.031 respectively. Figure 6.12(b) and (c) are distribution of f_b for 15 and 20 GeV/c muons. Table 6.6 is a summary of statistical uncertainties for f_b's.

muon Pt(GeV/c)	data	bottom	charm	background	3 components	total
10	2.6	5.2	5.5	1.6	7.7	7.8
15	5.2	5.2	4.2	2.3	6.5	7.0
20	13.0	6.3	9.3	5.2	12.9	14.5

Table 6.6: Statistical error of bottom fraction.

6.7 Systematics of Bottom Fraction

We anticipate possible systematic uncertainties in f_b due to uncertainties in particle lifetimes, our model for the background, resolution differences between Monte Carlo and data (including the effect of radiation damage).

1. Our Monte Carlo simulation uses the B lifetime measured by LEP, which

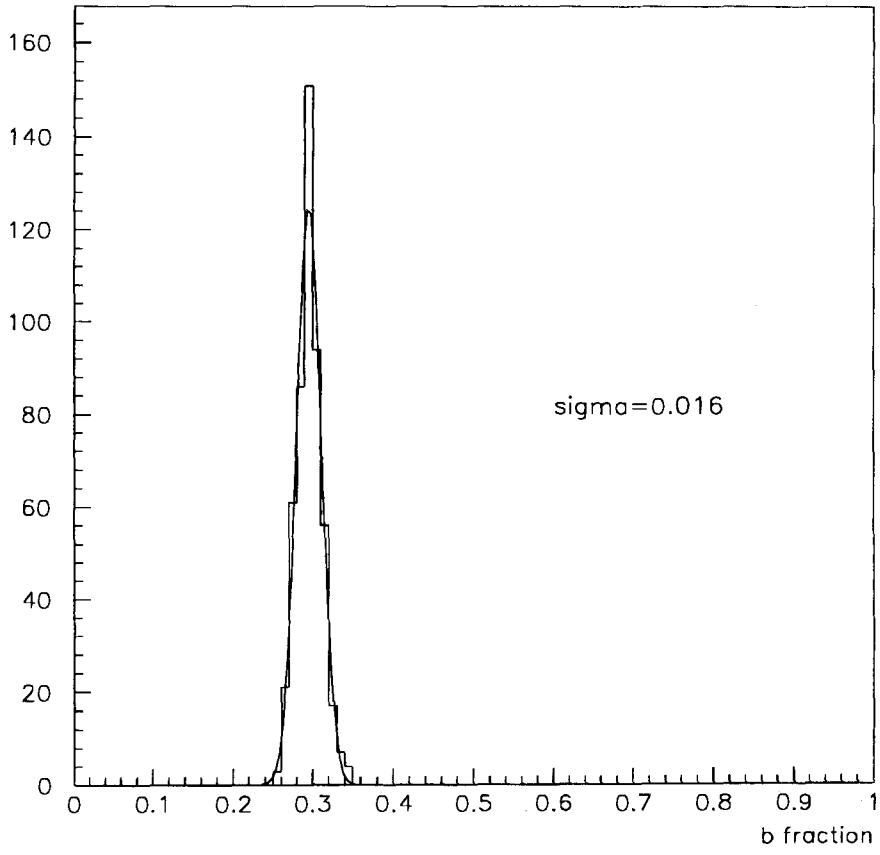

Figure 6.11: Bottom fraction change due to statistical fluctuation of bottom muons for 10 GeV/c muons.

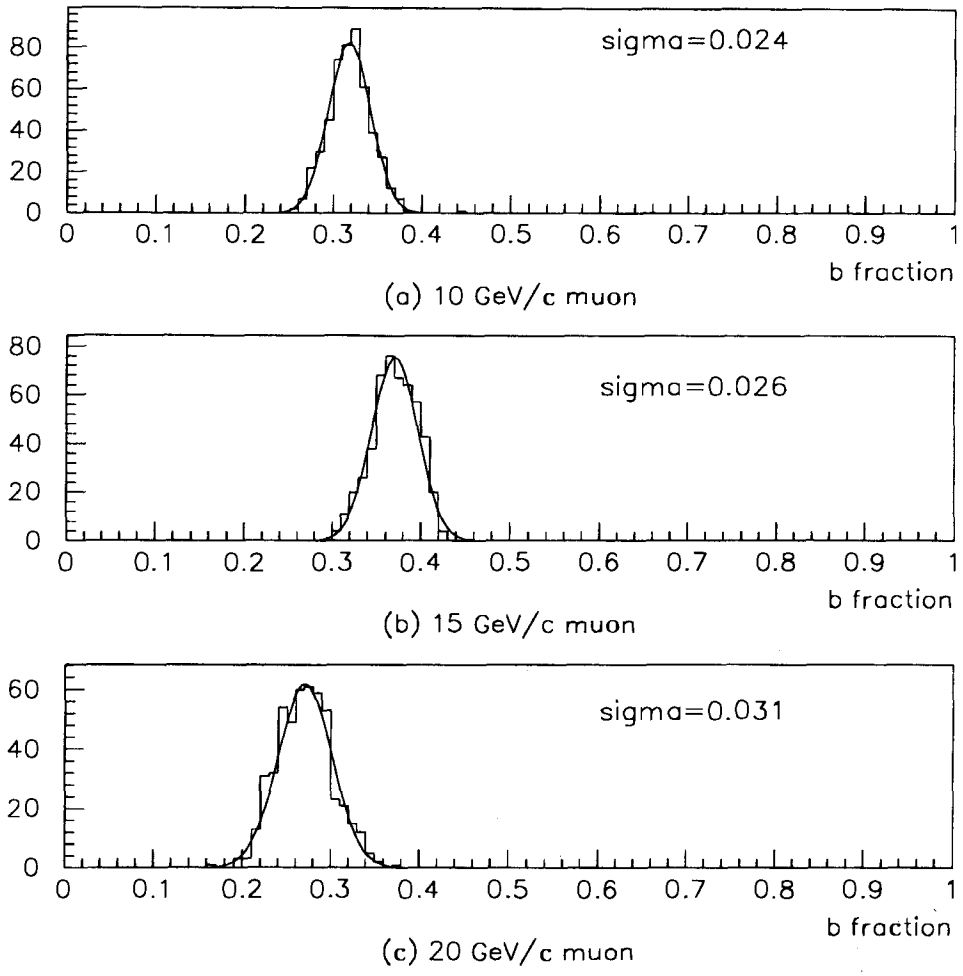

Figure 6.12: Bottom fraction change due to statistical fluctuation of all 3 components for 10,15 and 20 GeV/c muons.

has 10% uncertainty [67]. Since the impact parameter distribution of bottom muons changes as the B lifetime changes, the bottom fraction is affected by B lifetime. As can be seen in Equation (1.2), we can simulate the average effect of a B lifetime change of 10% by just broadening or shrinking the impact parameter distribution of bottom muons by 10%. We measure f_b after this manipulation of the bottom impact parameter distribution, and Table 6.7 shows the fractional changes of f_b for each Pt set of muon sample.

muon Pt(GeV/c)	original f_b	f_b change by shrinking	f_b change by broadening
10	0.310	0.352(+13.5%)	0.299(−3.5%)
15	0.383	0.421(+9.9%)	0.346(−9.7%)
20	0.270	0.296(+9.6%)	0.263(−2.6%)

Table 6.7: Change in f_b due to the B lifetime uncertainty.

2. We use generic tracks in a generic jet samples to model all non-heavy flavor background. To check the validity of this assumption, we measure f_b with DIF Monte Carlo samples instead of jet tracks for background model. We use a mixture of pion and kaon based on the ratio of two sources estimated in Section 6.2. We check only on 10 GeV/c muon samples. The bottom fraction measured with the DIF Monte Carlo sample is 0.323 ± 0.012, which agrees well with f_b measured with jet data within the statistical uncertainty. The bottom fraction is obviously dominated by the fit in the tail region, and small changes in the background function have a large effect just on the relative fraction of charm and background.

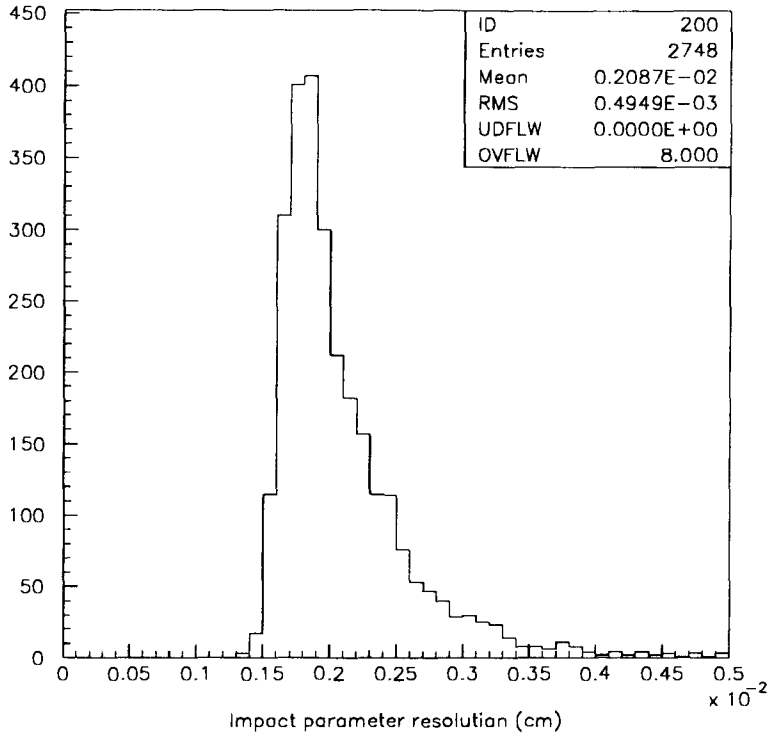

Figure 6.13: Impact parameter resolution of 10 GeV/c muons.

3. The bottom and charm impact parameter models use the Monte Carlo model for SVX resolution, which is not quite correct. However the resolution difference inferred by comparing RMS values of jet data and jet Monte Carlo distribution as in Figure 6.2 is only 3 μm. In addition to that, the resolution itself averages about $20\mu m$ in average for 10 GeV/c muon as seen in Figure 2.13. Both of these values are small compared to the width of the impact parameter distribution, which drives the fit for f_b. Therefore we expect the resolution difference in bottom and charm Monte Carlo samples will not affect f_b. To check this we redo the f_b analysis using 10 GeV/c tracks in the jet Monte Carlo sample instead of jet data and we find 0.301 ± 0.010, which agrees well with $f_b = 0.310 \pm 0.009$ as measured by jet data.

4. We have already noted that the SVX performance was affected by radiation damage. Most of the effect of radiation damage on the impact parameter distribution should be minimized by our track quality cuts, but there may still be an effect on f_b. To check this, we measure f_b in 2 partitions of data, early data and late data. Early data are from run number 40000 to 43000 and late data are from 47000 to 48000. Since Monte Carlo does not suffer from radiation damage, we group only muon data and jet data. Table 6.8 lists the measured f_b's for 10 GeV/c muons with 4 different combinations of muon data and jet data. For reference we also measure f_b both before and after the track quality cut is applied. Before the track quality cut is applied, there is a big difference. Late data is broader than early data and f_b is affected. But after applying the track quality cut, we can see that the run dependence of f_b disappears and f_b's agree within the statistical error. Therefore we claim that radiation damage does not affect f_b once we apply quality cuts.

muon data	jet data	f_b before quality cut	f_b after quality cut
early	early	0.358±0.014	0.326±0.015
early	late	0.273±0.012	0.290±0.014
late	early	0.475±0.020	0.298±0.022
late	late	0.415±0.019	0.286±0.022

Table 6.8: Effect of radiation damage on f_b of 10 GeV/c muons.

We believe this check of systematic effects shows that the lifetime uncertainty of B mesons is the main source of systematic uncertainty. Table 6.9 summarizes

the statistical and systematical uncertainty of the bottom fraction for each muon momentum selection.

muon Pt cut (GeV/c)	f_b	stat. error(%)	syst. error(%)
10	0.310	7.8	$-3.5+13.5$
15	0.383	7.0	$-9.7+9.9$
20	0.270	14.5	$-2.6+9.6$

Table 6.9: Bottom fraction and error.

Chapter 7

Results and Conclusion

We found the bottom fractions in Chapter 6 and can now calculate b cross sections by inserting these bottom fractions into Equation (5.4).

The cross sections are

$$\sigma(p\bar{p} \rightarrow b + X; Pt_b > 15GeV; |y| < 1.0) = 584.0 - 119.1 + 117.4\ nb$$

$$\sigma(p\bar{p} \rightarrow b + X; Pt_b > 25GeV; |y| < 1.0) = 98.5 - 16.6 + 17.6\ nb$$

$$\sigma(p\bar{p} \rightarrow b + X; Pt_b > 35GeV; |y| < 1.0) = 17.5 - 4.0 + 4.1\ nb$$

where the errors are the sum in quadrature of statistical and systematical uncertainties.

Figure 7.1 shows our measurements along with the theoretical prediction and other CDF measurements. The upper bound theory curve is obtained by using MRSA

structure function with b quark mass (m_b) = 4.5 GeV, energy scale (μ) = $\mu_0/2$ = $\sqrt{m_b^2 + P_t^2}/2$ and Λ_5 = 300 MeV and the lower bound curve for m_b = 5.0 GeV, $\mu = 2\mu_0$ and Λ_5 = 151 MeV . Other CDF measurements sit above the theoretical prediction, but near the upper boundary of the theoretical prediction. Our measurement agrees with other CDF measurements within uncertainties, but has central values somewhat lower, especially at large Pt.

We note that our measurement provides the first cross section measurement at CDF for $Pt^b_{min} > 35$ GeV/c. In this case, the power of our technique has allowed us to measure the bottom cross section with good precision in a new kinematic regime. In all regimes, we can now use the bottom cross section to measure correlated b quark cross sections, where one b is detected from the muon decayed from b quark and the second b quark is detected with secondary vertex techniques [68].

Bottom cross sections measured by other hadron collider experiments, UA1 and D0, were discussed in Chapter 1. We can compare all 3 measurements to see if they are consistent with theory. Figure 7.2 is the ratio between data points and the upper theoretical prediction on a linear scale [69]. This figure shows that UA1 and D0 results agree well with the prediction while CDF points are slightly high, but consistent with prediction within uncertainties. Our measurement shows the same trend. The difference between CDF and D0 should be understood, but we conclude that our measurement along with other CDF measurements are consistent with the theory of bottom production in high energy hadron collisions.

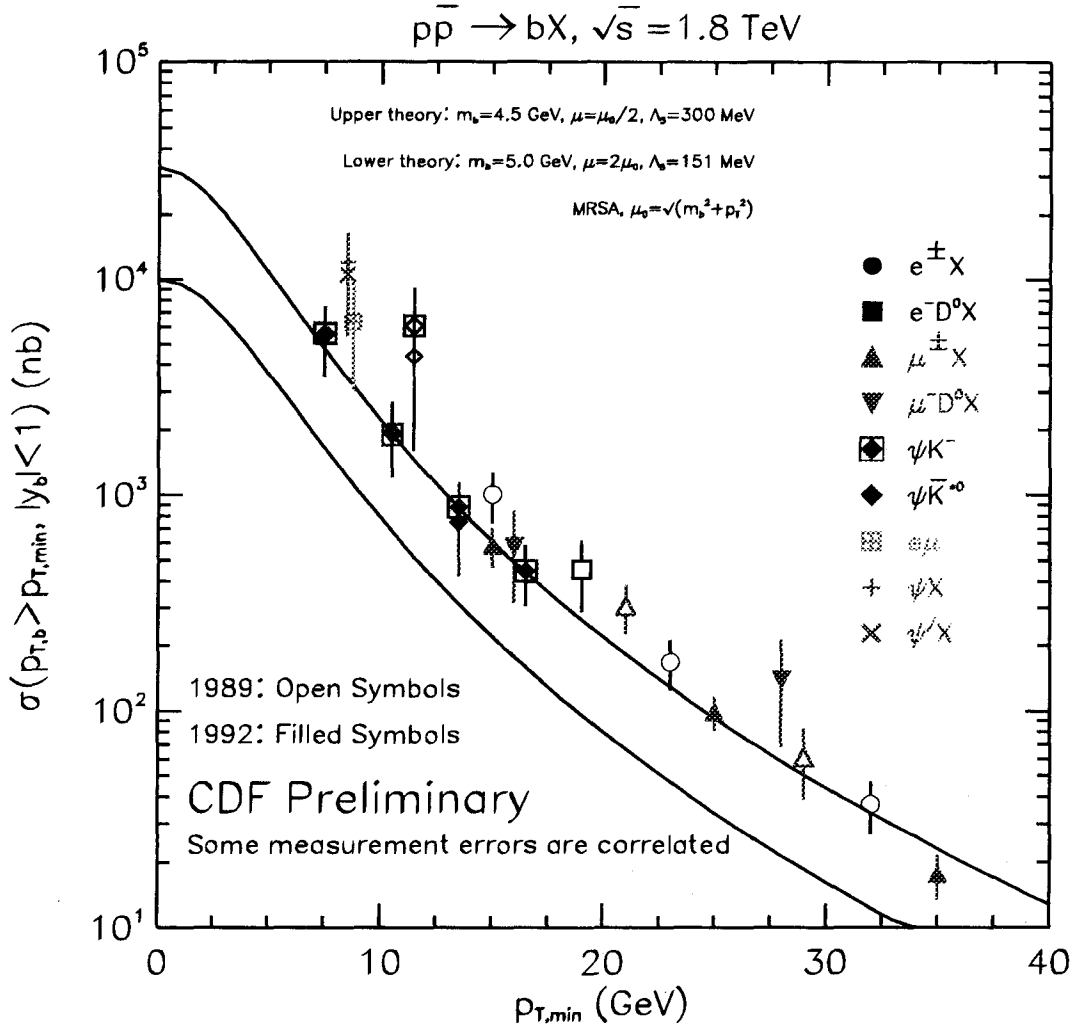

Figure 7.1: The b quark cross section along with theoretical prediction and other CDF measurements.

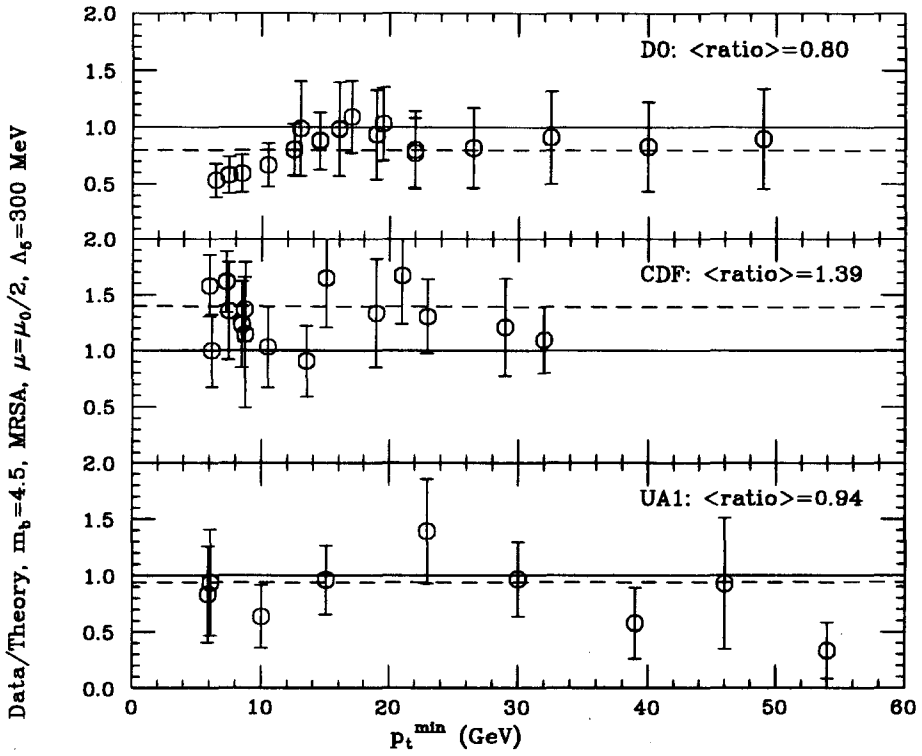

Figure 7.2: Ratio of data and theory for b cross sections at CDF, D0 and UA1.

Bibliography

[1] F. Halzen and A. Martin, "Quarks & Leptons : An Introductory Course in Modern Particle Physics", John Wiley and Sons, New York, 1984.

[2] K. Huang, "Quarks, Leptons & Guage Fields", World Scientific, 1982.

[3] F. Abe *et al.*, Phys. Rev. Lett 73(1994) 225.

[4] G. Arnison *et al.*, Phys. Lett. B 122(1983) 103.

G. Arnison *et al.*, Phys. Lett. B 126(1983) 398.

[5] J.C. Collins and D.E. Soper, Annu. Rev. Nucl. Part. Sci. 37(1987) 383.

[6] L. DiLella, Annu. Rev. Nucl. Part. Sci. 35(1985) 107.

[7] I. Hinchliffe, LBL Preprint, LBL-25820(1988).

[8] R.K.Ellis, Fermilab Preprint, FERMILAB-Conf-89/168-T(1989).

[9] C. Albajar *et al.*, CERN Preprint, CERN-PPE/90-155 Rev(1990).

C. Albajar *et al.*, Phys. Lett. B186(1987) 237.

C. Albajar *et al.*, Phys. Lett. B213(1988) 405.

N. Ellis and A. Kernan, Phys. Rep. 195(1990) 23.

[10] S. Frixione *et al.*, CERN Preprint, CERN-TH.7292/94(1994).

[11] C. Albajar *et al.*, Phys. Lett. B 186(1987) 237.

[12] K.M. Ankoviak, 8th Topical Workshop on Proton-Antiproton Collider Physics (1989) 537.

[13] F. Bedeschi *et al.*, Nuclear Instruments and Methods in Physics Research A268(1988) 50.

[14] G. Ascoli *et al.*, Nuclear Instruments and Methods in Physics Research A268(1988) 33.

[15] *ibid.*

[16] *ibid.*

[17] A. Gauthier *et al.*, CDF internal note 1500(1991).

[18] D. Amidei *et al.*, Fermilab Preprint, Fermilab-Pub-94/024-E(1994).

[19] S.A. Kleinfelder, IEEE Trans. Nucl. Sci. 35(1988) 171.
C. Haber *et al.*, IEEE Trans. Nucl. Sci. 37(1990) 1120.

[20] P. Billoir *et al.*, Nuclear Instruments and Methods in Physics Research A241(1985) 115.

[21] P.F. Derwent, CDF internal note 2188(1994).

[22] H. Wenzel, CDF internal note 1924(1993).

[23] F. Bedeschi *et al.*, CDF internal note 2055(1993).

[24] D. Amidei *et al.*, Fermilab Preprint, Fermilab-Pub-94/024-E(1994).

[25] *ibid.*

[26] D. Amidei *et al.*, CDF internal note 2061(1993).

[27] S. Belforte *et al.*, CDF internal note 2361(1994).

S. Belforte *et al.*, CDF internal note 2535(1994).

[28] *ibid.*

[29] T. LeCompte *et al.*, CDF internal note 2367(1994).

[30] G.W. Foster *et al.*, Nuclear Instruments and Methods in Physics Research A269(1988) 93.

[31] T. LeCompte *et al.*, CDF internal note 2367(1994).

[32] *ibid.*

[33] P. Koehn *et al.*, CDF internal note 2894(1994).

[34] T. Kamon *et al.*, CDF internal note 2458(1993).

[35] G.S. Sganos, private note, "Tutorial on CDFSIM"(1992).

[36] R. van Kooten, Proceedings of 7th Rencontres de physique de la Vallee d'Aoste, La Thuile, Aosta Valley, Italy, 1993.

[37] Particle Data Group, "Review of Particle Properties", Phys. Rev. D 50(1994) 1582.

[38] Particle Data Group, "Review of Particle Properties", Phys. Rev. D 50(1994) 1572.

[39] S. Henderson *et al.*, Phys. Rev. D45(1992) 2212.

[40] *ibid.*

[41] *ibid.*

[42] B.T. Huffman, Ph.D. Thesis, Purdue University, Dec. 1992.

[43] Particle Data Group, "Review of Particle Properties", Phys. Rev. D 50(1994) 1524.

Particle Data Group, "Review of Particle Properties", Phys. Rev. D 50(1994) 1446.

[44] P.B. Straub *et al.*, Phys. Rev. D 45(1992) 3030.

[45] V.D. Barger and R.J.N. Phillips, "Collider Physics", Addison-Wesley Publishing Company, 1988.

[46] D. Frei, CDF internal note 1430(1991).

[47] B.T. Huffman, Ph.D. Thesis, Purdue University, Dec. 1992.

[48] *ibid.*

[49] *ibid.*

[50] *ibid.*

[51] *ibid.*

[52] V.D. Barger and R.J.N. Phillips, "Collider Physics", Addison-Wesley Publishing Company, 1988.

[53] J. Chrin, Z. Phys. C36(1987) 165.

D. Decamp *et al.*, Phys. Lett. B244(1990) 551.

[54] S. Henderson *et al.*, Phys. Rev. D45(1992) 2212.

[55] T. LeCompte *et al.*, CDF internal note 2367(1994).

[56] W. Badgett, CDF internal note 2217(1993).

[57] M.W. Bailey *et al.*, CDF internal note 2815(1994).

[58] C.E. Anway-Wiese, CDF internal note 1986(1993).

[59] W. Badgett, CDF internal note 2527(1994).

[60] *ibid.*

[61] S. Belforte *et al.*, CDF internal note 2361(1994).

S. Belforte *et al.*, CDF internal note 2535(1994).

[62] R. Hollebeek, MKII note, "Distance of Closest Approach Distributions for Vertex Studies"(1982).

[63] B.T. Huffman, Ph.D. Thesis, Purdue University, Dec. 1992.

[64] C. Campagnari, private communication.

[65] L. Lyons, "Statistics for Nuclear and Particle Physicists", Cambridge University Press, Cambridge, 1986.

[66] F. James and M. Ross, CERN Preprint, CERN-D506 MINUIT(1989).

[67] Particle Data Group, "Review of Particle Properties", Phys. Rev. D 50(1994) 1610.

[68] P. Derwent *et al.*, CDF internal note 2581(1994).

[69] M.L. Mangano, private note, "Recent Progress in the Theory of Heavy Quark and Quarkonium Production in Hadronic Collisions"(1994).